A Study of Radiative Muon Pair Production at the Z^0 Resonance

Fraser Niles Hatfield

Department of Physics

The University of Sheffield

May 1993

Thesis Submitted in Partial Fulfilment
of the Requirements for the
Degree of Doctor of Philosophy
in the subject of Physics.

Abstract

A study has been made of radiative muon pair production in the region of the Z^0 resonance using the data collected over the period 1990 to 1991 by the ALEPH detector at the CERN Large Electron-Positron (LEP) Collider. From this work several measurements were performed. The first of these was the measurement of the total cross-sections for the processes $e^+e^- \rightarrow \mu^+\mu^-\gamma$, and $e^+e^- \rightarrow \mu^+\mu^- N\gamma$, for a minimum photon energy of 2 GeV. These measurements were made at seven centre of mass energies in the region of the Z^0 resonance between 88.222 GeV and 94.201 GeV. It was found that the cross-sections measured for the 1990 data set were generally lower than the predictions. But this was thought to be due to a statistical fluctuation. With the inclusion of the 1991 results the cross-section measurements were found to be in acceptable agreement with the predictions.

The second measurement was of the forward-backward charge asymmetry. This was done for the combined data below the peak, at the peak, and above it. For the measurements either side of the Z^0 resonance, agreement was found between the real data and the predictions, although the statistical and systematic errors were very large. The asymmetry at the Z^0 peak was measured separately for data collected in 1990 and 1991 using two different methods. The magnitudes of the asymmetries obtained using these methods were found to be approximately 2 sigma larger than the prediction for both data sets. But the significance of these deviations was not so high as to rule out simple statistical fluctuations as the explanation.

As well these measurements, a set of kinematic distributions for the process $e^+e^- \rightarrow \mu^+\mu^-\gamma$ were obtained, and these were all found to agree well with the electroweak predictions.

Finally a search was conducted for $\mu^\star$ creation in Z^0 decays, in both the single and pair production channels. In both cases the observations were found to be consistent with the predictions of QED.

Preface

This thesis describes a study of radiative muon pair production in electron-positron annihilation events. This work was conducted using data collected by the ALEPH detector, which is positioned on the LEP collider at CERN, Geneva. From the data, which were obtained at centre of mass energies in the region of the Z^0 resonance, total cross-section and asymmetry measurements were performed, and these were compared with the predictions of the Electroweak model. Using the same data set, a search was made for the appearance of the excited state of the muon, which is predicted by models of compositeness.

In addition to this analysis, I was involved with the ECAL group, whose tasks were to run and maintain the ALEPH electromagnetic calorimeter, which is one of the main subdetectors of ALEPH. My role in this group was to assist in the manning of shifts during the physics running period. Also, during my stay at CERN, I was responsible for the transfer of ALEPH data cartridges back to the Rutherford Appleton Laboratory.

The results presented here were obtained from my own physics analysis, and are not official ALEPH results.

None of the work referred to here has been submitted in support of an application for another degree or qualification in this or any other university or institution of learning.

Acknowledgements

During my postgraduate years at Sheffield University and CERN in Geneva, I have made many friends and acquaintances of different nationalities and backgrounds who have contributed in some way to my PhD thesis. First of all I wish to express my gratitude to my supervisor Professor Fred Combley for giving me the chance to continue with my studies in physics and for proof reading my thesis. I would also like to thank him and his wife Margaret for the hospitality and support they have shown me over the years. May I also convey my appreciation for all the help and advice Drs Chris Booth and Susan Cartwright have given me during my course. I would especially like to express my gratitude to Susan who spent a great deal of time proof reading my thesis. My special thanks goes out to all of the other members of the Sheffield HEPP group both past and present who have given me a lot of help, whether through friendship or advice given; thanks to Lee, Craig, John, Jolyon, Darren, Mark, Richard, Philip, Chris, Ayda, Hou and Steve and not forgetting the members of the HEPP 'Muffin Club': Wayne, Mike, Andy and Ian. To Mahmut I express my personal thanks for being a good friend throughout. From my time at CERN I would like to thank: Andy Halley, Ingrid Tenhave, Dave Salmon, Mark Nuttall, Anil Patel and Edmund Whelan.

During my course I have received a great deal of help from people based at CERN and Sheffield. In particular I wish to express my gratitude to Gerard Bonneaud for many useful discussions concerning my analysis, and E. Lancon and F. Ranjard for all of the help given to me concerning Monte Carlo production. Z. Was, B.F.L Ward, and S. Jadach are three people who deserve special thanks for all of the help that they have given me concerning the predictions and technical points of their event generator which was used in my analysis. Finally, thank you to S. Sazhin who translated for me a theoretical paper from Ukrainian to English.

I am especially grateful for all of the financial support given to me during my course which came in the form of the Robert Styring Scholarship from Sheffield University and from the SERC while I was at CERN.

Finally, I thank my family for all the love and support they have given to me over the years, and it is to them that this thesis is dedicated.

April 30, 1993

A long time ago in a galaxy far,

far away....

Contents

List of Figures

List of Tables

Chapter 1

The Theories of High Energy Particle Physics

1.1 Introduction

Since the dawn of civilization, mankind has gazed in wonderment at its physical surroundings. Its curiosity for the countless hundreds of bright twinkling stars in the night sky, and for the wide variety of shapes and colours of material objects in these surroundings, and their associated phenomena, has led to many questions being asked. Questions like, 'Where does it all come from ?', 'What is it all made of ?' and 'What are the rules, if any, which govern the behaviour of physical objects in our universe ?'. Today, we have a set of theories, which between them are helping us to find solutions to some of these questions. These theories, collectively known as the Standard Model, have been built up from hundreds of experimental observations and theoretical advances which have been made over the centuries of scientific investigation and are capable of very precise predictions about the behaviour of matter under certain conditions.

We now know that the basic building blocks of materials on Earth are atoms, of which there are over a hundred different types, and these cluster together in different

combinations to form the chemical compounds. An atom is constructed from a tiny central nucleus which carries a positive electric charge, and surrounding this is a swarming cloud of particles called electrons which each carry a negative electric charge. The nucleus is itself built from a number of smaller particles called protons and neutrons. The neutrons are electrically neutral and it is the protons which give the nucleus its positive charge. Also it is the number of protons which are present within a nucleus which determines the type of chemical element formed.

Until recently, it was believed that there were four fundamental forces in nature which acted upon and between the atoms and their constituents. The first force, which is the most important one at the atomic level, is the electromagnetic force. This is responsible for the interactions between all electrically charged particles, and is repulsive for like signed charges and attractive for unlike signed charges. It is this force which keeps the electrons in orbit around the nucleus, and also gives rise to all of the reactions between the chemical elements. The second force is known as the weak force and this is responsible for the radioactive processes such as the nuclear β-decay of the neutron. The third force is called the strong force. This is stronger than both the electromagnetic and the weak forces. It is this force which is responsible for holding together the constituents of the atomic nucleus which would otherwise fly apart under the influence of the repulsive electromagnetic force between the protons. The fourth and most familiar of the fundamental forces is the gravitational force. This acts upon all particles and over all distances. It is responsible for the motions of the stars and planets, and for the large scale structure of the universe. But on the subatomic scale it is the weakest force of all. The Standard Model concerns itself only with the first three forces. This is because gravity is explained classically by general relativity [1], which is very different from the theories used to describe the other forces. Also to study the effect of gravity at the subatomic level, very high energy densities are required and very short distance scales need to be probed, and these cannot be achieved by the current

generation of particle colliders used to test the Standard Model.

We now know that the constituents of the atom are not the only particles found in nature and that there are a great deal more which can be created in high energy collisions. These particles fall into two classes, the 'Leptons' and the 'Hadrons'. The leptons are a family of six particles and these can be grouped into doublets to form a three generation family. Three species of lepton possess mass, and have the same electric charge as the electron, – e. The electron is a member of this group, and the other two charged members are the muon and tau particles. The other three types of lepton are all electrically neutral and are called neutrinos. At the present time these particles are thought to be massless, although this has not been proved. The charged members of this group take part in both the electromagnetic and weak interactions, while the neutral members only participate in the weak interactions.

The hadrons are a group consisting of over a hundred members which all possess mass. The proton and neutron are members of this group. These particles are different from the leptons in that they feel the strong force as well as the electromagnetic and weak forces.

For each of the leptons and hadrons there is an antiparticle. These possess the same masses as the particles do, but have the opposite sign in their electric charges, magnetic moments, and in their associated quantum numbers, which are explained in the following sections.

Another difference between the leptons and hadrons is that the leptons are apparently fundamental, while the hadrons are constructed from smaller particles called 'Quarks'. The quarks were originally introduced as mathematical entities in order to explain, in terms of symmetry principles, the structure of the large hadron family. Evidence for their existence was discovered by deep inelastic electron-proton scattering experiments at SLAC [2]. The quarks come in six types or 'flavours', as do the leptons, and these can also be grouped into doublets to form a three generation family. The

quarks differ from the leptons in that they are all massive and all carry a fraction of the electric charge carried by the electron. No free quark has ever been observed, but they are found to cluster together in either of two ways to form the hadrons. Bound states of three quarks can be produced, and these are called 'Baryons', the proton and neutron are the most familiar of these. Also bound states of a quark and an antiquark can be formed and these are called 'Mesons'. Well known examples of these are the pion and the kaon.

The forces between the particles are transmitted via the exchange of packets of energy or 'quanta'. In the case of the electromagnetic force the interactions between charged particles are mediated via the massless photon, and the strength of this interaction is attributable to the electromagnetic charge carried by the particles. The model which best describes this kind of interaction is the very successful quantum electrodynamics theory (QED). The weak force is mediated by a set of three massive particles, the W^+, W^-, and the Z^0. The strong force between the quarks is mediated by a set of eight massless particles called 'gluons'. The strength of this type of interaction is due to the strong charge carried by the quarks, and also by the gluons themselves, called 'colour'. This is why the hadrons feel the strong force. The theory which best describes the interactions between quarks and gluons is called quantum chromodynamics (QCD).

The fundamental particles and force mediators all possess an intrinsic angular momentum called 'spin', which is quantized into multiples of the Planck constant $\hbar \left(= \frac{h}{2\pi}\right)$. The particles with spins which are half-integer multiples of $\hbar$ are known as 'Fermions', while the particles with spins which are integer multiples of $\hbar$ are known as 'Bosons'.

The quarks[1], leptons[2] and force mediators are listed in tables 1.1, 1.2 and 1.3 along with their spins and electric charges. Also contained within these tables are the particles

[1]The top quark still remains to be discovered.

[2]Evidence for the tau-neutrino's existence as a distinct particle is still not conclusive.

Quark Flavour		Spin $\hbar$	Charge e	Lepton Number	Baryon Number
up	(u)	$\frac{1}{2}$	$+\frac{2}{3}$	0	$\frac{1}{3}$
down	(d)	$\frac{1}{2}$	$-\frac{1}{3}$	0	$\frac{1}{3}$
charm	(c)	$\frac{1}{2}$	$+\frac{2}{3}$	0	$\frac{1}{3}$
strange	(s)	$\frac{1}{2}$	$-\frac{1}{3}$	0	$\frac{1}{3}$
top	(t)	$\frac{1}{2}$	$+\frac{2}{3}$	0	$\frac{1}{3}$
bottom	(b)	$\frac{1}{2}$	$-\frac{1}{3}$	0	$\frac{1}{3}$

Table 1.1: *The Quarks.*

Lepton Flavour		Spin $\hbar$	Charge e	Lepton Number	Baryon Number
electron	(e)	$\frac{1}{2}$	-1	+1	0
electron-neutrino	(ν_e)	$\frac{1}{2}$	0	+1	0
muon	(μ)	$\frac{1}{2}$	-1	+1	0
muon-neutrino	(ν_μ)	$\frac{1}{2}$	0	+1	0
tau	(τ)	$\frac{1}{2}$	-1	+1	0
tau-neutrino	(ν_τ)	$\frac{1}{2}$	0	+1	0

Table 1.2: *The Leptons.*

Force Mediator		Spin $\hbar$	Charge e	Lepton Number	Baryon Number
photon	γ	1	0	0	0
weak bosons	$W^{\pm}$, Z^0	1	$\pm$1,0	0	0
gluons	g_i (i = 1,...,8)	1	0	0	0

Table 1.3: *The Force Mediators.*

lepton and baryon numbers. These numbers are assigned to all particles, and are found to be conserved in all interactions.

In the late 1960's and early 1970's it was theoretically predicted that the weak and electromagnetic forces were but two different manifestations of a single force, known as the electroweak force. Experimental verification of this has come from the discovery of weak neutral currents in 1973 [3] and also from the discovery of the Z^0, and the $W^{\pm}$ particles [4,5,6]. This unification was a great triumph and has led many theorists to try to incorporate this interaction along with the strong interaction and gravity into one whole encompassing scheme. This is the road towards the so called Grand Unified Theories (GUTS) of all fundamental interactions [7].

By studying the process of radiative muon pair production, which is a direct result of electron-positron annihilation, it is possible to test the leptonic sector of the electroweak model, at the level of higher order corrections. With this in mind, the following sections will give the main points of the QED and weak interaction theories. The electroweak theory is then described, building on the results presented in the preceding sections. Following this, the application of the electroweak theory to the subject of radiative muon pair production is explained. Finally, the subject of compositeness is discussed as a possible solution to some of the problems of the electroweak theory, and its relevance to the study of radiative muon pair production is explained.

1.2 Quantum Electrodynamics

Quantum electrodynamics (QED) is the theory which describes the interactions between charged particles and photons. It is a theory which has been able to predict, to extremely high precision, experimentally determined quantities such as the anomalous magnetic moment of the muon [8] and the Lamb shift in the hydrogen spectrum [9]. Its origins lay in the foundation of the wave theory of electromagnetism, which was developed by James Clerk Maxwell in 1867, as a unification of the phenomena of electricity and magnetism[10]. In 1931 Paul A M Dirac combined the ideas of this theory with quantum mechanics and special relativity, and from this the ideas of quantum field theory were born[11].

In quantum field theory there is an intimate connection between the conservation laws and symmetry operations. For example, the principle of the conservation of momentum can be demonstrated by the effect of an infinitesimal translation in space applied to the wavefunction or field describing a particle in an isolated system[12]. In QED, which was the prototype quantum field theory, the application of symmetry operations, known as gauge transformations, to a particle field, show the existence of conserved electromagnetic currents.

QED is a locally gauge or phase invariant theory describing electromagnetic interactions by local gauge symmetries. It is the aim of this section to explain the meaning of this statement.

QED is constructed using the Lagrangian formulation of field theory which is based on the 'Principle of Least Action' [3]. The action is defined by equation 1.1.

$$S = \int \mathcal{L}\left(\phi, \partial_\mu \phi\right) d^4x, \tag{1.1}$$

where ϕ is the scalar field of a free particle and $\partial_\mu = \frac{\partial}{\partial x_\mu}$. $\mathcal{L}$ is the Lagrangian density

[3]The following equations are written in a standard notation, which is fully explained in references [13,14].

and $L = \int \mathcal{L} d^3x$ the Lagrangian, although $\mathcal{L}$ is also frequently referred to simply as the Lagrangian. This principle states that the motion of a particle described by ϕ is the one which minimizes S. Under a variation in ϕ the action is a minimum when

$$\partial_\mu \left(\frac{\partial \mathcal{L}}{\partial(\partial_\mu \phi)} \right) - \frac{\partial \mathcal{L}}{\partial \phi} = 0. \tag{1.2}$$

This is known as the Euler-Lagrange field equation and is the equation of motion for the particle described by ϕ.

For a freely moving spin $\frac{1}{2}$ particle of mass m, represented by a four component spinor field ψ, the Lagrangian is given by equation 1.3.

$$\mathcal{L} = i\bar{\psi}\gamma^\mu \partial_\mu \psi - m\bar{\psi}\psi \tag{1.3}$$

where γ^μ are the Dirac gamma matrices [12] and $\bar{\psi} = \gamma^\circ \psi^\dagger$. On substituting this expression for $\mathcal{L}$ into 1.2, the Dirac relativistic wave equation 1.4 is obtained.

$$(i\gamma^\mu \partial_\mu - m)\psi = 0. \tag{1.4}$$

The Lagrangian defined by equation 1.3 can be shown to be invariant under the gauge transformation:

$$\psi(x) \rightarrow \psi\,'(x) = e^{i\alpha}\psi(x). \tag{1.5}$$

This transformation is parameterized by the real number α, which for so-called global transformations is fixed at all points in space-time. Transformations of this kind belong to a family known as the U(1) unitary gauge group. This group is Abelian, that is, it contains operators which are commutative. The invariance of the Lagrangian over this transformation implies the existence of a conserved vector current, with an equation of continuity given by

$$\partial_\mu j^\mu = 0, \tag{1.6}$$

where the conserved current j^μ is given by

$$j^\mu = -\bar{\psi}\gamma^\mu \psi. \tag{1.7}$$

This is known as Noether's Theorem. If we define $\alpha = e\theta$, where e is the magnitude of the electron's electric charge, then we obtain

$$j^{\mu}_{em} = -e\bar{\psi}\gamma^{\mu}\psi. \tag{1.8}$$

This is the electromagnetic charge current density for an electron. It follows from 1.6 that the charge Q of a particle is a conserved quantity, and this can be shown using equation 1.9

$$Q = \int d^3x \; j^0. \tag{1.9}$$

The idea that the phase should be fixed simultaneously at all points in space-time is inconsistent with the principles of relativity theory. Yang and Mills [15] therefore proposed the substitution of a variable phase $\alpha = \alpha(x)$. Now by making the transformation as before, we get:

$$\psi(x) \rightarrow \psi\,'(x) = e^{i\alpha(x)}\psi(x) \tag{1.10}$$

and the conjugate of this is

$$\bar{\psi}(x) \rightarrow \bar{\psi}\,'(x) = e^{-i\alpha(x)}\bar{\psi}(x). \tag{1.11}$$

These are called local gauge transformations. The only problem here is that the Lagrangian is no longer invariant. The derivative $\partial_\mu\psi$ transforms as:

$$\partial_\mu\psi \rightarrow e^{i\alpha(x)}\partial_\mu\psi + ie^{i\alpha(x)}\psi\partial_\mu\alpha \tag{1.12}$$

and so does not transform in the same way as $\psi(x)$. Instead another term appears which must be cancelled in order to get back to the previous state of affairs. For the Lagrangian to be invariant under this local gauge transformation a 'covariant derivative' D_μ must be introduced which transforms like $\psi(x)$ i.e.

$$D_\mu\psi(x) \rightarrow e^{i\alpha(x)}D_\mu\psi(x). \tag{1.13}$$

For the extra term to be cancelled, the derivative must have the form:

$$D_\mu \equiv \partial_\mu - ieA_\mu, \tag{1.14}$$

where A_μ is a 4-vector field which must transform as:

$$A_\mu \rightarrow A_\mu + \frac{1}{e}\partial_\mu \alpha(x). \tag{1.15}$$

By replacing ∂_μ by D_μ equation 1.4 becomes

$$\mathcal{L} = i\bar{\psi}\gamma^\mu D_\mu \psi - m\bar{\psi}\psi, \tag{1.16}$$

or

$$\mathcal{L} = \bar{\psi}(i\gamma^\mu \partial_\mu - m)\psi + e\bar{\psi}\gamma^\mu A_\mu \psi. \tag{1.17}$$

So by requiring local phase invariance the vector field A_μ has to be introduced. This is known as a gauge field and can be identified with the photon field which couples to the Dirac particles and governs their electromagnetic interactions. By using the current given in equation 1.8 the new interaction term which appears in equation 1.17 can be rewritten as $-j^\mu_{em} A_\mu$, in terms of the electromagnetic current density and the photon field. For this gauge field to represent the electromagnetic field another term must be added to the Lagrangian to take into account the kinetic energy of this field. This new term must be invariant under the transformation stated by equation 1.15. So the gauge invariant field tensor $F_{\mu\nu}$ is used, and this is defined in equation 1.18,

$$F_{\mu\nu} = \partial_\mu A_\nu - \partial_\nu A_\mu, \tag{1.18}$$

and a term of the form $-\frac{1}{4}F_{\mu\nu}F^{\mu\nu}$ is added to the Lagrangian. Now the full Lagrangian of QED can be obtained.

$$\mathcal{L}_{QED} = \bar{\psi}(i\gamma^\mu \partial_\mu - m)\psi + e\bar{\psi}\gamma^\mu A_\mu \psi - \frac{1}{4}F_{\mu\nu}F^{\mu\nu}. \tag{1.19}$$

Here it must be noted that a term for the photon mass of the form $\frac{1}{2}m^2 A_\mu A^\mu$ cannot be added because this would break the gauge invariance once more. This shows that the photon must be massless, and by the Heisenberg uncertainty principle, the photon field must have an infinite range. So by requiring the Lagrangian of a free particle to be invariant under local gauge transformations the interacting field theory for QED has

been obtained, and the statement that QED is a locally gauge or phase invariant theory describing electromagnetic interactions by local gauge symmetries has been explained.

1.3 Weak Interactions

The development of the weak interaction theory has its origins in the discovery of radioactivity which was first observed by Becquerel in 1896. In 1914 Chadwick discovered that the electrons emitted in nuclear β-decay had a continuous energy spectrum [16]. This implied the break-down of the laws of conservation of energy and momentum, since it was assumed that this process was a two-body decay. In order to explain this electron energy spectrum, Wolfgang Pauli postulated the existence of the neutrino, which was responsible for carrying away part of the available energy. A theory which was in close analogy to QED was developed by Fermi in 1934 [17] in which nuclear β-decay was considered to be a vector current reaction with a coupling constant G_F. Using this model good agreement was found between the predictions and the experimental observations of β-decay. The Lagrangian developed for this model was invariant with respect to Lorentz transformations and spatial inversions. Spatial inversions are known as parity operations, and it was thought that parity was always conserved in weak interactions.

Later, the observation of parity violating effects led to much theoretical and experimental work and a generalization of the Fermi theory was developed by Gell-Mann and Feynman. In this generalization, which was called V-A theory, the currents contained terms of the form $\bar{\psi}\gamma_\mu(1-\gamma^5)\psi$, which contains a vector current and also what is known as an axial vector current. An important result from this model was that the $(1-\gamma^5)\psi$ factor implies that only left-handed neutrinos and right-handed antineutrinos, i.e. those with negative helicity ($H = -\frac{1}{2}$), can participate in weak interactions [18]. The helicity of the electron-neutrino, which is the projection of its

spin $\vec{S}$ along the direction of its momentum vector $\vec{P}$ as defined by equation 1.20,

$$H \equiv \frac{\vec{S} \cdot \vec{P}}{|\vec{P}|}, \tag{1.20}$$

was measured in an experiment by Goldhaber et al. [19], and the result of this experiment gave support to this model.

The V-A theory provided an excellent phenomenological account of the observed charged weak interactions. But the theory suffered from large divergences in the cross-section calculations at large energies due to higher order corrections which violated the conservation of probability, also known as Unitarity. This was because the cross-sections were directly proportional to the energy brought into the interaction and so would increase as the energy increased. In QED, similar divergences are removed by absorbing the higher order corrections into the particle charges and masses, and then equating these to their experimentally determined values. This process, known as 'Renormalization', saves QED from these infinities. The V-A theory, on the other hand, is non-renormalizable because to remove all divergences to all orders would require an infinite number of parameters. So this theory, although having some success, could not be used as the basis for a set of complete predictions at all energies.

1.3.1 The Intermediate Vector Boson Model.

A partial solution to these problems was to consider the interactions as taking place via the exchange of massive intermediate vector bosons which are the carriers of the weak force. This theory, known as the intermediate vector boson model (IVB), has its origins in QED and the Yukawa theory of nuclear interactions [20], and uses the idea that the charged weak interactions take place via the mediation of two charged bosons, the W^+ and the W^-, each having the same mass M_W. The IVB model was applied to the subject of muon decay and was found to describe this process well at low energies or momentum transfers q, i.e when $q^2 \ll M_W^2$. This was also the case for the V-A

theory. By equating the coefficients of the matrix element equations for both models, as shown in equation 1.21,

$$\frac{G_F}{\sqrt{2}} = \frac{g^2}{8M_W^2}, \tag{1.21}$$

it was found that there were two possible explanations for the fact that the weak interaction strength is small when compared with that of the electromagnetic interaction. Either the dimensionless coupling constant g was small or the mass of the weak bosons was large. The start of the unification of these two interactions into one scheme occurs when the assumption is made that the couplings in these two theories are of equal strength and that the weakness of the weak interactions is due to the massiveness of the W^+ and W^- bosons.

The IVB theory worked well at low energies as did the V-A theory. But it too had the problems of being non-renormalizable at high energies and once again unitarity was violated. This is due to the fact that real $W^{\pm}$'s have longitudinal polarization states and this results in cross-sections, for processes such as $\nu_\mu \overline{\nu}_\mu \rightarrow W^+W^-$, which increase with energy. For the case of virtual $W^{\pm}$ particles, which mediate the weak force, unitarity is not violated because the couplings here are dimensionless and so are independent of energy. In order to solve this problem theorists turned to QED for help and considered the analogous process $e^+e^- \rightarrow \gamma\gamma$. The cross-section for this process does not violate unitarity at high energies since real photons do not possess longitudinal polarization states, and this can be traced to the gauge invariance property of QED. It was this fact which led theorists to try to construct a gauge theory of weak interactions.

Even though the IVB model was not completely successful theorists still believed that the weak and electromagnetic forces could be unified. In order to construct a unified theory, it was thought that the $W^{\pm}$'s and the γ should all be part of a triplet of vector bosons, with one coupling constant. It was shown by Glashow [21] that this was not possible and that a new neutral vector boson must be included, the W^0. This triplet formed from the W^+, W^-, and the W^0, coupling to a weak neutral current, could

be described using the $SU(2)_L$ group of symmetry transformations. The handedness or 'Chirality' of the V-A theory is retained here, due to the fact that these weak bosons have only left handed couplings and this is denoted by the letter L. In order to include the photon in the theory the $U(1)_Y$ group was introduced. (The Y subscript will be explained shortly.) By requiring local gauge invariance, as in QED, under $SU(2)_L \times U(1)_Y$ transformations, four gauge bosons must enter the theory. The first two real particles in this new theory are formed from the first two members of the $SU(2)_L$ triplet, i.e. the W^+ and the W^-, and the last two are formed from a mixture of the third member W^0 with the $U(1)_Y$ component. One of these particles is the familiar photon and the other is a new particle, the weak neutral vector boson Z^0; the amount of mixing is measured by the Weinberg angle θ_W.

In the earlier section on QED, it was explained that the Lagrangian could not be locally gauge invariant if mass terms were included. Since the photon is massless, everything was fine. But since the W^+ and W^- were assumed to be massive this presented a big problem for some time. The solution to this lay in the ideas of 'Spontaneous Symmetry Breaking', and these will now be explained.

1.3.2 The Higgs Mechanism

Here it is imagined that the symmetry of the ground state around which the theory is built, i.e the vacuum, is broken even though the symmetry in the Lagrangian is manifest. By requiring global gauge invariance, a massive scalar particle is introduced as well as massless scalars, which are unwanted by the theory. But by demanding local gauge invariance in a similar way to section 1.2, the massless scalars are 'eaten' by the W's, giving them mass and appearing as the longitudinal polarization state of the W's. The application of this to the $SU(2)_L \times U(1)_Y$ gauge symmetry is known as the Higgs mechanism and the remaining massive scalar particle is called the Higgs boson [22] which is at present still being looked for [23].

Now that the main ideas of the weak interaction theory and QED have been described the ideas of the electroweak model can be explained.

1.4 The Electroweak Model.

The electroweak model is a gauge theory built from $SU(2)_L \times U(1)_Y$ symmetry. Work was done on this theory independently by Weinberg [24], and Salam [25], who used the ideas of Glashow and Higgs. It was postulated that this theory was renormalizable due to the fact that only massless gauge bosons are contained in the unbroken Lagrangian. This was later shown to be correct by t'Hooft and Veltman in 1971 [26].

Due to the V-A structure the left-handed and right-handed fields transform differently under local $SU(2)_L \times U(1)_Y$ gauge transformations. In this model the left-handed components are grouped together to form doublets while the right-handed components are treated as singlets. This is illustrated for the first generation of quarks and leptons.

$$\chi_L = \begin{pmatrix} \nu_e \\ e^- \end{pmatrix}_L , \begin{pmatrix} u \\ d \end{pmatrix}_L \tag{1.22}$$

$$\psi_R = e_R^-, u_R, d_R \tag{1.23}$$

It must be remembered here that there are no corresponding right-handed neutrinos. The elements of a doublet are considered to be different states of the same particle which are related by an internal symmetry transformation.

As in QED, the requirement that the Lagrangian is invariant under local $SU(2)_L \times U(1)_Y$ gauge transformations forces the introduction of interactions between the gauge bosons and fermions and shows the existence of conserved currents. For the left-handed doublets, the invariance of the Lagrangian under $SU(2)_L$ transformations introduces the interactions between left-handed particles. Also it shows the existence of three conserved 'Weak Isospin' currents. By requiring the invariance of the Lagrangian under $U(1)_Y$ transformations, the interactions between the left-handed and right-handed

Leptons	Q	T	T_3	Y
$\nu_e\ \nu_\mu\ \nu_\tau$	0	$\frac{1}{2}$	$\frac{1}{2}$	-1
$e_L^-\ \mu_L^-\ \tau_L^-$	-1	$\frac{1}{2}$	$-\frac{1}{2}$	-1
$e_R^-\ \mu_R^-\ \tau_R^-$	-1	0	0	-2

Table 1.4: *The electroweak quantum numbers of the leptons.*

states are introduced. Also this shows the existence of a conserved 'Weak Hypercharge' current. Due to the existence of the conserved currents the left-handed doublets and right-handed singlets can be assigned new types of charge called weak isospin T and weak hypercharge Y, and these are related to the electric charge Q from the $U(1)$ by equation 1.24,

$$Q = \mathrm{T}_3 + \frac{\mathrm{Y}}{2}, \tag{1.24}$$

where T_3 is the third component of weak isospin. The values of T, T_3, Y, and Q for the leptons are given in table 1.4.

In this model the left-handed and right-handed components transform differently, i.e.

$$\begin{aligned} \chi_\mathrm{L} &\rightarrow \chi'_\mathrm{L} = e^{i\alpha(x)\mathrm{T}+i\beta(x)\mathrm{Y}}\chi_\mathrm{L} \\ \psi_\mathrm{R} &\rightarrow \psi'_\mathrm{R} = e^{i\beta(x)\mathrm{Y}}\psi_\mathrm{R} \end{aligned} \tag{1.25}$$

Here T is called the generator of the $SU(2)_\mathrm{L}$ gauge group and Y is the called the generator of the $U(1)_\mathrm{Y}$ gauge group.

Using similar arguments to those presented in section 1.2 a locally gauge invariant Lagrangian for the electroweak theory can be constructed, viz

$$\begin{aligned}\mathcal{L} &= \bar{\chi}_{\rm L}\gamma^{\mu}\left[i\partial_{\mu} - g\frac{1}{2}\mathrm{T}\cdot W_{\mu} - g'\frac{\mathrm{Y}}{2}B_{\mu}\right]\chi_{\rm L} \\ &\quad + \bar{\psi}_{\rm R}\gamma^{\mu}\left[i\partial_{\mu} - g'\frac{\mathrm{Y}}{2}B_{\mu}\right]\psi_{\rm R} - \frac{1}{4}W_{\mu\nu}\cdot W^{\mu\nu} - \frac{1}{4}B_{\mu\nu}B^{\mu\nu}, \qquad (1.26)\end{aligned}$$

where the expressions contained within the [ ] are the covariant derivatives for the left and right handed states. The fermions couple to the triplet of fields W_{μ} from $SU(2)_{\rm L}$ and the field B_{μ} from $U(1)_{\rm Y}$ with couplings g and g' respectively. The last two terms in equation 1.26 represent the kinetic energy and self-coupling of the W_{μ} fields and the kinetic energy of the B_{μ} field. To allow the $W^{\pm}$ and Z^{0} fields to possess mass and to keep the photon massless the Higgs mechanism is introduced into the theory via the addition of an extra term to the Lagrangian. This is given by equation 1.27.

$$\mathcal{L}_{H} = \left|\left(i\partial_{\mu} - g\mathrm{T}\cdot W_{\mu} - g'\frac{\mathrm{Y}}{2}B_{\mu}\right)\phi\right|^{2} - \mu^{2}(\phi^{\dagger}\phi) - \lambda(\phi^{\dagger}\phi)^{2} \qquad (1.27)$$

This is necessary because the introduction of a mass term of the form $m\psi\bar{\psi}$ would stop the Lagrangian from being invariant. This Lagrangian contains ϕ which is a complex scalar doublet.

$$\phi = \begin{pmatrix}\phi^{+}\\ \phi^{o}\end{pmatrix} = \sqrt{\frac{1}{2}}\begin{pmatrix}\phi_1 + i\phi_2\\ \phi_3 + i\phi_4\end{pmatrix} \qquad (1.28)$$

The introduction of the Higgs mechanism into the theory allows the $U(1)$ symmetry, from QED, to remain unbroken while the $SU(2)_{\rm L}\times U(1)_{\rm Y}$ is broken, so that the QED sector of the theory is kept. The last two terms of $\mathcal{L}_{H}$ taken together are known as the Higgs potential. To generate the masses of the gauge bosons in the theory the case where $\mu^{2} < 0$ and $\lambda > 0$ is considered. In this case the minimum of the potential term, which is called the vacuum state, is defined as:

$$\phi^{\dagger}\phi \equiv \frac{1}{2}(\phi_1^{2} + \phi_2^{2} + \phi_3^{2} + \phi_4^{2}) = \frac{-\mu^{2}}{2\lambda}. \qquad (1.29)$$

A particular vacuum state can be chosen by setting ϕ_1, ϕ_2 and ϕ_4 equal to zero. The

vacuum state ϕ_{vac} is then given by

$$\phi_{vac} = \sqrt{\frac{1}{2}} \begin{pmatrix} 0 \\ v \end{pmatrix}, \tag{1.30}$$

where

$$v = \sqrt{\frac{-\mu^2}{\lambda}}. \tag{1.31}$$

The symmetry of the Lagrangian $\mathcal{L}_H$ has now been broken by the selection of a particular vacuum and the gauge bosons can now acquire mass in the theory. Due to gauge invariance we can rewrite equation 1.30 as:

$$\phi(x) = e^{i\mathbf{T}\cdot\theta(x)/v} \sqrt{\frac{1}{2}} \begin{pmatrix} 0 \\ v + h(x) \end{pmatrix}, \tag{1.32}$$

so that fluctuations around the vacuum state can be taken into account. This is parameterized in terms of four fields, $\theta_1, \theta_2, \theta_3$ and h. Here h is a real field and the $\theta_i(x)$'s are three phase degrees of freedom. The Lagrangian is locally $SU(2)_{\mathrm{L}}$ invariant so the three fields $\theta_i(x)$ can be gauged away. The three fields which are gauged describe the particles known as Goldstone bosons [27]. The remaining field is that of a massive scalar, and it is this state which is known as the Higgs boson. By substituting ϕ_{vac} into the Lagrangian the boson masses can be identified. The relevant term in the Lagrangian is then given by:

$$\frac{1}{8}v^2g^2\left[(W_\mu^1)^2 + (W_\mu^2)^2\right] + \frac{1}{8}v^2(g'B_\mu - gW_\mu^3)(g'B^\mu - gW^{3\mu}) + \cdots \tag{1.33}$$

So now the mass terms for the vector bosons and also the scalar Higgs particle, of mass μ, are all contained within this Lagrangian. The physical fields W^+ and W^- are obtained from the following combinations:

$$W^+ = \frac{1}{\sqrt{2}}(W^1 - iW^2) \tag{1.34}$$

and

$$W^- = \frac{1}{\sqrt{2}}(W^1 + iW^2) \tag{1.35}$$

and the mass of these bosons is given simply by

$$M_W = \frac{1}{2}vg. \tag{1.36}$$

Also two neutral fields are obtained which are a mixture of the W_μ and B_μ fields:

$$\begin{aligned} Z_\mu &= -\sin\theta_W B_\mu + \cos\theta_W W_\mu^3 \\ A_\mu &= \cos\theta_W B_\mu + \sin\theta_W W_\mu^3 \end{aligned} \tag{1.37}$$

where Z_μ and A_μ are identified as the Z^0 and photon fields respectively. The Weinberg mixing angle θ_W can be written as:

$$g\sin\theta_W = g'\cos\theta_W = e \tag{1.38}$$

relating the strength of the weak interactions to the electromagnetic coupling of QED. The particle masses of these fields are found to be:

$$M_Z = \frac{1}{2}v\sqrt{g^2+g'^2} \quad \text{and} \quad M_A = 0. \tag{1.39}$$

By combining the above equations a relation between the masses of the weak bosons is obtained:

$$\frac{M_W}{M_Z} = \cos\theta_W \tag{1.40}$$

Using the Higgs mechanism masses can also be acquired by the fermions by the addition of an extra term to the Lagrangian. But the theory as it stands cannot predict their masses and so these remain as experimental inputs to the model.

The physics research being carried out by the LEP experiments at CERN is concentrated in the region of the Z^0 resonance. That part of the total electroweak Lagrangian which is applicable to the interactions in this region is given by equation 1.41.

$$\mathcal{L}_{NC} = -e\overline{\psi}\gamma^\mu Q_f \psi A_\mu - \frac{g}{cos\theta_W}\overline{\psi}\gamma^\mu\left(\left(1-\gamma^5\right)\mathrm{T}_3 - 2Q_f sin^2\theta_w\right)\psi Z_\mu \tag{1.41}$$

This can be rewritten in terms of the axial (a_f) and vector (v_f) couplings for the Z^0 component. These are defined as:

$$a_f = \mathrm{T}_3 \tag{1.42}$$

Final State	v_f	a_f
$e^+e^-, \mu^+\mu^-, \tau^+\tau^-$	$-\frac{1}{2}[1-4\sin^2\theta_W]$	$\frac{1}{2}$
$\nu_e\bar{\nu_e}, \nu_\mu\bar{\nu_\mu}, \nu_\tau\bar{\nu_\tau}$	$\frac{1}{2}$	$\frac{1}{2}$

Table 1.5: *The axial and vector couplings for the leptons.*

$$v_f = T_3 - 2Q_f \sin^2\theta_W. \tag{1.43}$$

This gives:

$$\mathcal{L}_{NC} = -e\bar{\psi}\gamma^\mu Q_f \psi A_\mu - \frac{g}{\cos\theta_W}\bar{\psi}\gamma^\mu(v_f - a_f\gamma^5)\psi Z_\mu. \tag{1.44}$$

The vector and axial couplings for the leptons are given in table 1.5.

From the electroweak Lagrangian the 'Feynman rules' can be obtained simply by inspection, and using this information it is possible to calculate the cross-sections and asymmetries for processes which occur in e^+e^- annihilation in the region of the Z^0 resonance. The Feynman rules obtained from this Lagrangian are given in figure 1.1.

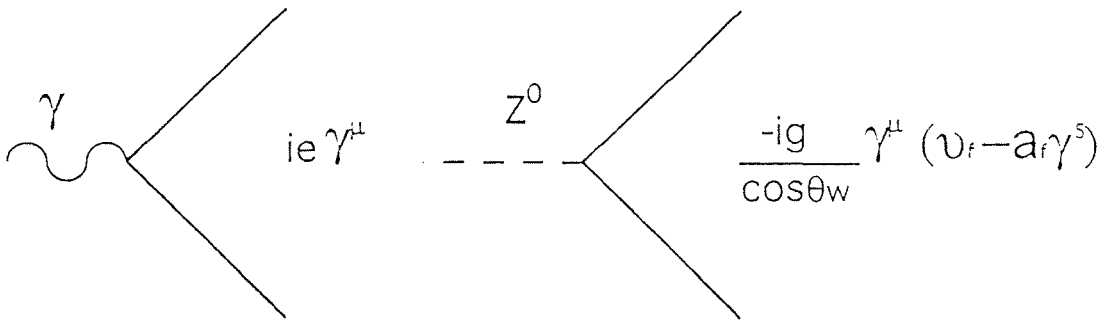

Figure 1.1: *Feynman rules obtained from the electroweak Lagrangian.*

By way of example, the two lowest order Feynman diagrams which describe the process in which an electron and a positron annihilate to form a muon pair, i.e. $e^+e^- \rightarrow \mu^+\mu^-$, are shown in figures 1.2a and 1.2b.

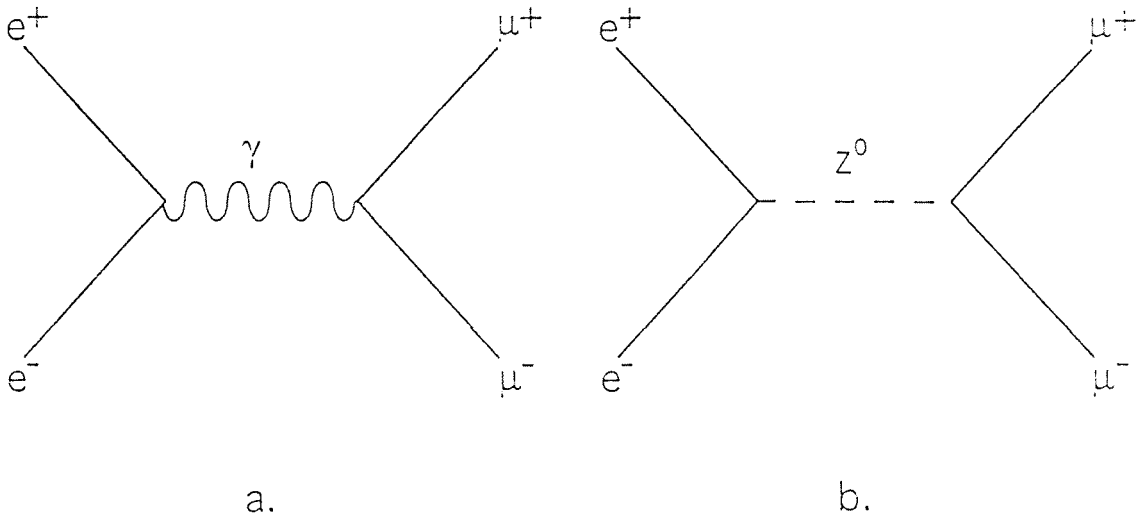

Figure 1.2: *Feynman diagrams for the process* $e^+e^- \rightarrow \mu^+\mu^-$.

1.5 The Theory of Radiative Muon Pair Production

1.5.1 Introduction

Radiative muon pair production is the process where a muon pair, produced in an electron positron annihilation, is accompanied by at least one photon, radiated in either the initial or the final state of the interaction. Research in this area of physics allows tests to be made of both QED and the electroweak theory. Also, it is possible to test for the existence of the excited state of the muon, which has been predicted by compositeness models.

Radiative muon pair production has been studied by several experiments covering a range of centre of mass energies well below the Z^0 resonance. The results of these experiments can be found in references [28,29,30,31,32].

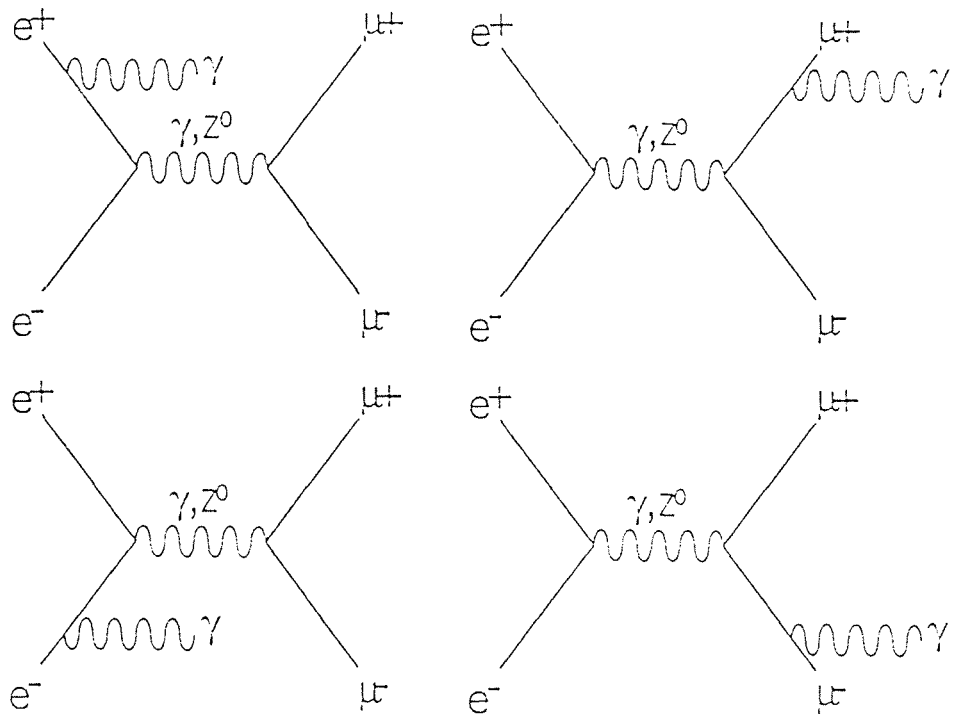

Figure 1.3: *The lowest order Feynman diagrams for the process* $e^+e^- \rightarrow \mu^+\mu^-\gamma$.

1.5.2 The Total Cross Section for $e^+e^- \rightarrow \mu^+\mu^-\gamma$

The $\mu^+\mu^-\gamma$ final state can be created via any one of eight different production routes. The routes are illustrated by the set of Feynman diagrams shown in figure 1.3. The processes can be mediated by either the photon or the Z^0 with the latter being the dominant propagator at LEP.

The diagrams represent the lowest order contributions to the process $e^+e^- \rightarrow \mu^+\mu^-\gamma$, and are of order α^3, where α is a dimensionless QED coupling constant, which is defined as $\alpha = \frac{e^2}{4\pi}$ (in Heaviside-Lorentz units [12]) [4], and has a value of about $\frac{1}{137}$.

By considering these diagrams, it is possible to obtain analytical expressions for the lowest order total and differential cross-sections for the process $e^+e^- \rightarrow \mu^+\mu^-\gamma$, within the context of the electroweak model. The full analytical expressions are given

[4]For momentum transfers of the order of M_W the value is approximately $\frac{1}{128}$.

in reference [33]. It is the initial state radiation diagrams which give rise to the largest contributions to the radiative muon pair cross-sections. This is due to terms of the form $\ln s/m_e^2$ which are large due to the smallness of the electron mass m_e. Hence, we would expect to see more initial state photons than final state photons. But bremsstrahlung from charged particles tends to be strongly forward peaked in the direction of motion of the radiating particle. This being the case most of the initial state radiation (ISR) passes down the beam pipe undetected. At the Z^0 pole ISR is further suppressed because of the shift in $\sqrt{s}$ from M_Z so we are more likely to detect events containing final state radiation (FSR). By way of example the theoretical predictions for the angular distributions of both initial and final state photons in radiative muon pair events at 91.2 GeV are shown in figure 1.4.

1.5.3 Electroweak Radiative Corrections

Experimentally, it is not possible to measure directly the lowest order cross-section for the process $e^+e^- \rightarrow \mu^+\mu^-\gamma$, where the minimum photon energy is above some threshold. This is because there are many other contributions from higher order Feynman diagrams which can give rise to exactly the same final state as $\mu^+\mu^-\gamma$, and on an event by event basis are indistinguishable from this final state. So experiments would not observe the same number of events as predicted by this lowest order cross-section. The higher order contributions are known as 'Electroweak Radiative Corrections' (EWRC's). In the region of the Z^0 resonance these corrections are large and in order to compare experimental observations with theoretical predictions, the EWRC's are included in the cross-section calculations [34].

There are two types of correction which are applicable here. The first type is known as QED or photonic radiative corrections. The second is known as weak or non-photonic radiative corrections. The QED and weak corrections are listed in table 1.6. At the level of the $e^+e^- \rightarrow \mu^+\mu^-$ lowest order cross-section, these corrections form two

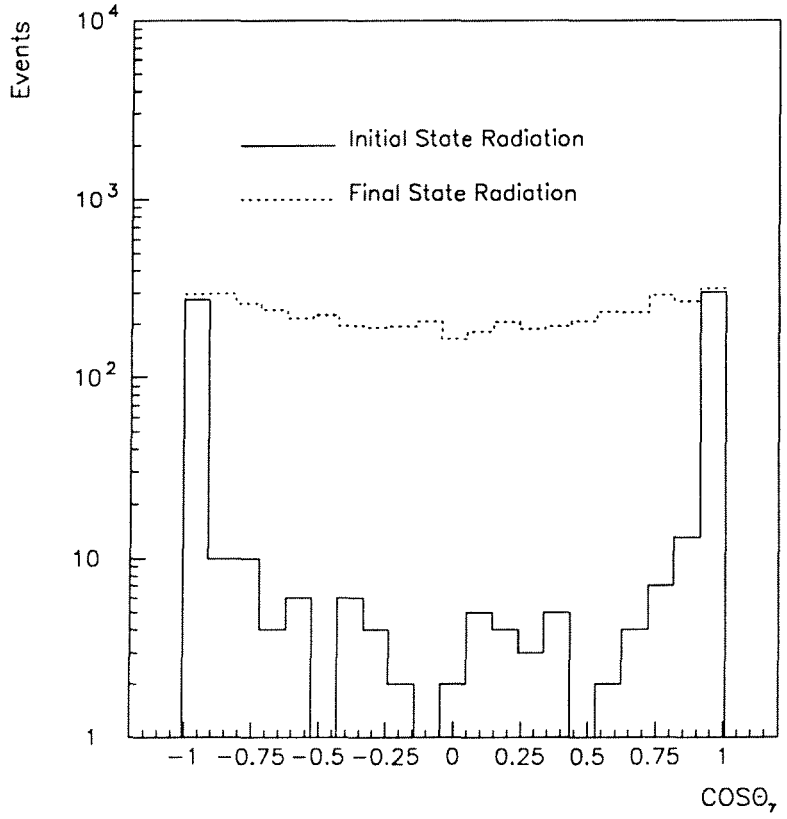

Figure 1.4: *The polar angle distributions of initial and final state photons of energy $E_\gamma \geq 2$ GeV at a centre of mass energy of 91.2 GeV.*

QED Corrections		*Weak Corrections*	
Real γ (Hard bremsstrahlung, Soft bremsstrahlung)	Virtual γ (Fermion self-energy, Vertex corrections, Box diagrams)	γ self energy, Z, W self energy, γ-Z mixing	Virtual Z, W, etc.

Table 1.6: $O(\alpha)$ *Electroweak Radiative Corrections.*

distinct groups, up to the one-loop level. But at higher orders they become mixed. At LEP energies it is the QED corrections which give rise to the largest contributions to the EWRC's. But these corrections are very well-known and depend only on the global parameters of the Z^0 exchange such as the Z^0 mass M_Z and width Γ_Z. The weak corrections on the other hand have a strong dependence on some of the unknown parameters of the electroweak model such as the Higgs mass and the top quark mass, since these can appear as contributions to virtual loop corrections. But when a suitable renormalization scheme is employed [34] the size of these corrections can be small in comparison to the QED corrections, of the order of a few percent.

Now in order to compare the predictions of the electroweak theory with the experimental observations, Monte Carlo event generators are used which incorporate these corrections. Event generators are large computer programs which simulate real physics events by producing sets of four momentum vectors corresponding to those of real particles. These programs contain the analytical cross-section formulae for a particular physics process and use Monte Carlo techniques [35] to create a random set of events whose distributions correspond to the calculated cross-sections. By studying Monte Carlo events it is possible to develop selection criteria for the real events under investigation and to correct the observed event yield for the losses incurred in applying those criteria. The generator used in this work to simulate radiative muon pair events is known as KORALZ. KORALZ simulates the complete muon-pair cross-section, $e^+e^- \rightarrow \mu^+\mu^-(n\gamma)$ [5]. The cross-section for events with a detectable photon can be deduced using equation 1.45,

$$\sigma_{\mu^+\mu^- N\gamma} = \frac{N_{\mu^+\mu^- N\gamma}}{N_{total}} \sigma_{total}, \tag{1.45}$$

where $N_{\mu^+\mu^- N\gamma}$ is the number of generated muon pair events containing $N(\geq 1)$ photons with an energy above an arbitrary minimum, and any number of lower energy

[5] $(n\gamma)$ signifies the inclusion of electroweak radiative corrections.

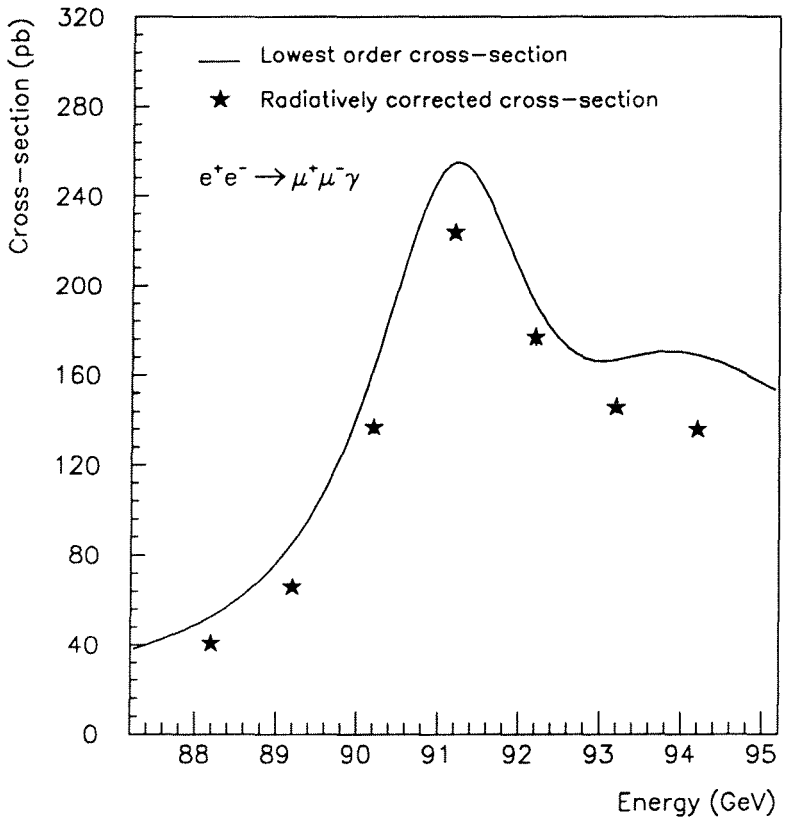

Figure 1.5: *The lowest order and radiatively corrected cross-sections for the process* $e^+e^- \rightarrow \mu^+\mu^-\gamma$ *where the minimum photon energy is 2 GeV. The radiatively corrected cross-section was calculated for 7 centre of mass energies which correspond to the points in the scan of the* Z^0 *resonance made using the LEP collider at CERN.*

photons, σ_{total} is the total generated muon pair cross-section calculated by KORALZ, and N_{total} is the total number of generated muon pair events. A more detailed account of KORALZ can be found in section 4.2.1. The effect of these higher order radiative corrections is illustrated by figure 1.5 which shows the variation with $\sqrt{s}$ of the lowest order cross-section for the process $e^+e^- \rightarrow \mu^+\mu^-\gamma$ and the radiatively corrected cross-section, calculated from the Monte Carlo. The effect of the EWRC's is to reduce the cross-sections and also to shift the position of the peak towards higher energies.

1.5.4 Forward Backward Charge Asymmetry

In the process $e^+e^- \rightarrow \mu^+\mu^-$ the muons emerge back to back, travelling in opposite directions. At low centre of mass energies far away from the Z^0 resonance, i.e. when $s - M_Z^2 \ll \Gamma_Z$, it is the photon exchange diagram given in figure 1.2a which best describes this process. The muon angular distribution for this process is then given by a differential scattering cross-section of the form [6]:

$$\frac{d\sigma}{d\Omega} = \frac{\alpha^2}{4s} N_c Q_e^2 Q_\mu^2 \left(1 + \cos^2\theta\right). \tag{1.46}$$

Here θ is the scattering angle between the incoming e^- and the outgoing μ^-, which

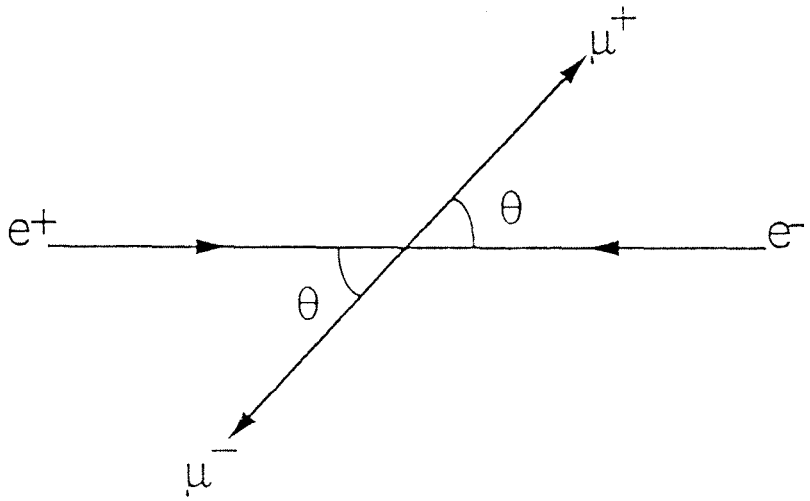

Figure 1.6: *Definition of the scattering angle θ.*

is defined in figure 1.6, N_c is the number of QCD colour degrees of freedom (N_C = 1 for leptons). In this case the angular distribution of the muons is symmetric in θ, i.e. the number of muons which are produced travelling at a direction θ is the same as the number at $\pi - \theta$. By including the Z^0 exchange diagram given in figure 1.2b the scattering probabilities are changed and the differential cross-section is then given by equation 1.47.

$$\frac{d\sigma}{d\Omega} = \frac{\alpha^2}{4s} N_c \left[G_1(s)\left(1 + \cos^2\theta\right) + G_2(s)\cos\theta\right], \tag{1.47}$$

[6] The fermion masses have been neglected here.

where $G_1(s)$ and $G_2(s)$ are energy dependent functions which are defined as:

$$G_1(s) = Q_e^2 Q_\mu^2 + 2Q_e Q_\mu v_e v_\mu Re(\chi_0) + \left(a_e^2 + v_e^2\right)\left(a_\mu^2 + v_\mu^2\right)\left|\chi_0^2\right| \tag{1.48}$$

and

$$G_2(s) = 4Q_e Q_\mu a_e a_\mu Re(\chi_0) + 8a_e a_\mu v_e v_\mu \left|\chi_0^2\right|. \tag{1.49}$$

Here Q_e and Q_μ are the electric charges of the electron and muon, a_e, a_μ, v_e, v_μ are their axial and vector couplings to the Z^0 and χ_0 is the Z^0 propagator, which is defined in equation 1.50.

$$\chi_0(s) = \frac{s}{s - M_Z^2 + iM_Z\Gamma_Z} \tag{1.50}$$

It can be seen that expression 1.47 reduces to equation 1.46 when low centre of mass energies are considered. By including the Z^0 exchange diagram an extra term containing $\cos\theta$ appears, giving rise to an asymmetry in the angular distribution so that the muons are no longer produced at directions θ and $\pi - \theta$ with equal probabilities. There are two contributions to this asymmetry and these are given by equation 1.49, where the first term is due to the interference between the γ and Z^0 exchange diagrams, and the second term is due entirely to the Z^0 exchange. At the energies accessible at PEP and PETRA [36,37] it is the interference term which controls the asymmetry. In e^+e^- collisions at LEP where the centre of mass energy is in the region of the Z^0 mass, i.e. when $s \approx M_Z^2$, it is the term due to the Z^0 exchange which determines the asymmetry of the muon angular distribution. The asymmetry can be measured by forming a forward-backward charge asymmetry A_{fb}:

$$A_{fb} = \frac{\int_0^1 \frac{d\sigma}{d\Omega} d\cos\theta - \int_{-1}^0 \frac{d\sigma}{d\Omega} d\cos\theta}{\int_0^1 \frac{d\sigma}{d\Omega} d\cos\theta + \int_{-1}^0 \frac{d\sigma}{d\Omega} d\cos\theta} \tag{1.51}$$

The differential cross-section given in equation 1.47 can be written in terms of A_{fb}:

$$\frac{d\sigma}{d\Omega} \propto \left(1 + cos^2\theta + \frac{8}{3} A_{fb} cos\theta\right). \tag{1.52}$$

At the pole of the Z^0 resonance, i.e. when $s \approx M_Z^2$, A_{fb} is close to zero [38]. For the case of radiative muon pair events, there is an additional contribution to A_{fb} due

to the interference between the initial state and final state radiation diagrams. At the Z^0 peak the contribution to the asymmetry from the interference is negligible in the absence of strong cut offs [39]. But when hard cuts are applied to kinematic variables such as photon energy and muon-photon angular separation this asymmetry is no longer negligible and its magnitude depends upon the cuts.

As in the case of the total cross-section, radiative corrections must be applied to the lowest order predictions for the asymmetries, and this is done within the Monte Carlo.

From the measurement of the cross-sections and asymmetries for these radiative processes it is possible to test the predictions of the electroweak model. The results of these measurements are given in chapter 5.

1.6 Compositeness

The standard model of particle physics provides a good description of the available data [40]. Despite this, there are still a large number of unsatisfactory features in the model, the principal ones being the large number of arbitrary parameters, the lack of direct evidence for the mass generation mechanism, and also the fermion spectrum.

The fact that the quarks and leptons can be grouped into a pattern of three generations, differing in mass, is reminiscent of the fact that the chemical elements could be arranged into a pattern called the periodic table and also that the hadrons were found to follow a pattern. In both of these cases the patterns formed could be explained by the existence of another layer of structure. In an attempt to overcome some of the problems of the standard model, theories have been developed which are based on the idea that the pattern and masses of the quarks and leptons, and possibly the gauge bosons, can also be explained by some simple underlying structure. There are many such composite models [41], but so far, none gives a satisfactory explanation

of the above problems. A prediction which is common to these models is the existence of excited states of the quarks and leptons. Direct searches for such particles have been conducted, but so far there is no evidence for their existence [42]: instead limits are placed on their masses and couplings within the different models of compositeness.

The excited muon postulated in compositeness theories is normally denoted $\mu^\star$. If light enough, it could be produced in Z^0 decays, either singly or in pairs. Once produced, the $\mu^\star$ would decay radiatively to its ground state, the μ, thus yielding $\mu^+\mu^-\gamma$ or $\mu^+\mu^-\gamma\gamma$ final states. The presence of such a contribution to the $\mu^+\mu^-\gamma\,(\gamma)$ cross-section would be demonstrated by a narrow peak in the $\mu\gamma$ invariant mass distribution. A study of this will be presented in chapter 5.

Chapter 2

The ALEPH Detector

2.1 The LEP Collider

In order to test the theories of high energy particle physics, particle accelerators have been constructed which are capable of colliding elementary particles at high energies. One such research tool is the Large Electron Positron (LEP) collider [43], which is based at the European Laboratory for Particle Physics, CERN, in Geneva, Switzerland. LEP is 27 km is circumference and is housed underground in a 3.8 m diameter tunnel. This tunnel straddles the Franco-Swiss border with an inclination of 1.42 % to the horizontal with its shallowest and deepest points at about 70 m and 150 m below ground level respectively. The accelerator itself consists of eight straight sections and eight arcs of lengths 490 m and 2840 m respectively. The orbit of the particle beams is maintained by some 3400 bending and 1902 focusing and correction magnets. Radio frequency (RF) cavities are distributed along the length of the collider and it is these which provide the particle acceleration mechanism.

To study the production and subsequent decay of the Z^0 boson in e^+e^- annihilations, centre of mass energies of around 91 GeV are required. At LEP the process of particle acceleration up to the required 45 GeV per beam is done in several stages. The system for particle injection into the LEP ring is shown in figure 2.1. The first step is to

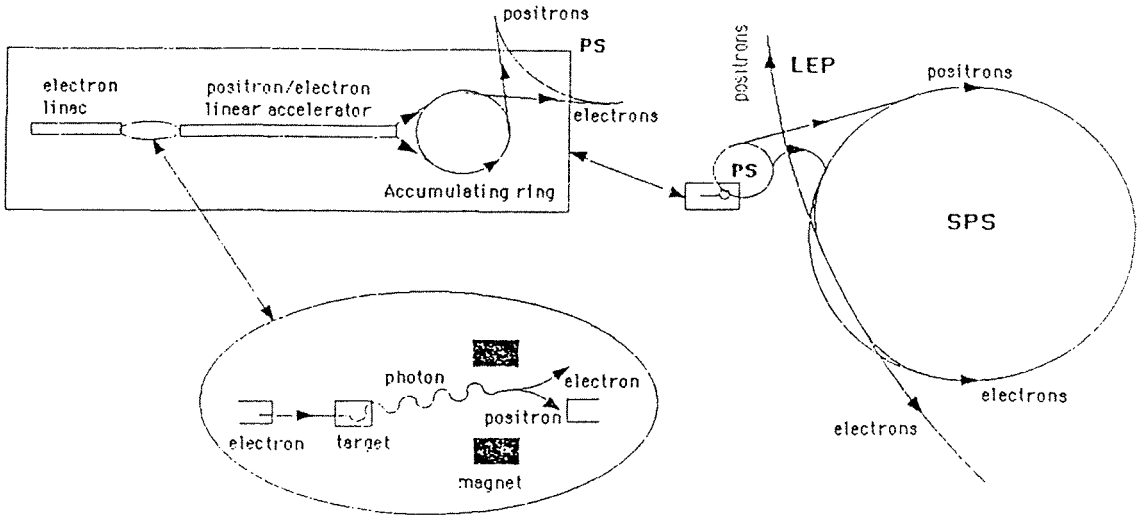

Figure 2.1: *The LEP injection scheme.*

produce the positron bunches. In order to do this short rapid bursts of electrons, which are fired from a hot filament, are accelerated up to an energy of 200 MeV by a linear accelerator (linac) and made to strike a tungsten target. The bremsstrahlung from this process pair produces into an electron-positron pair. The positrons are accelerated by a second linac up to an energy of 600 MeV and are then injected into the Electron Positron Accumulator ring (EPA). There they remain until 2×10^{11} positrons are stored. Next, the beam is injected into the proton synchrotron (PS) in around 11 s. When an energy of 3.5 GeV is attained, the beam is transferred into the super proton synchrotron (SPS). Here the positrons are accelerated to around 20 GeV before the final injection into LEP. The electron beam enters the LEP ring in a similar manner with the exception that it comes directly from the hot filament, and is itself initially accelerated by the 600 MeV linac before entering the EPA. The electron collection time is far quicker than for the positrons. This is due to the high intensity of the beam from the hot filament which allows the 2×10^{11} electrons to be collected in only 1 s. Full injection of the beams of particles into LEP takes approximately 15 minutes. Over this

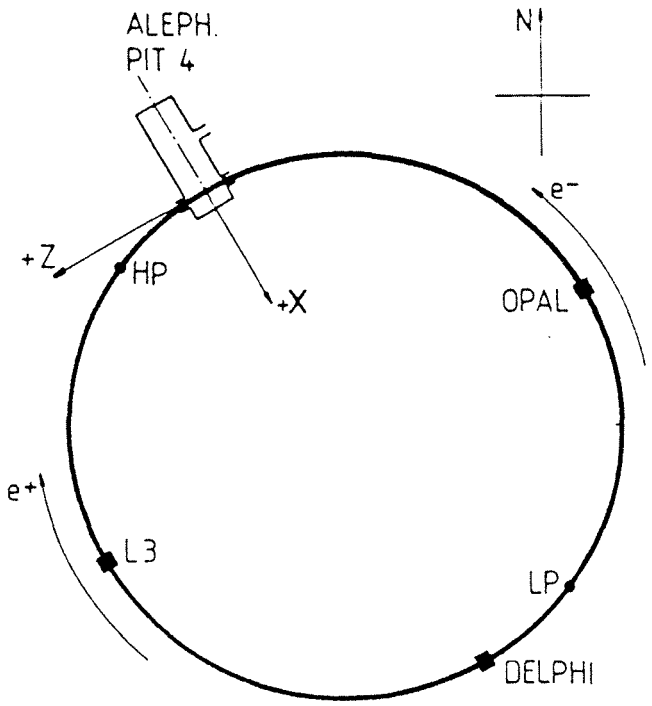

Figure 2.2: *The LEP Collider and the location of the four LEP experiments. N indicates the direction of north, HP and LP are the high and low points of the inclined ring.*

period of time the electrons and positrons are continually injected on a 15 s cycle. This continues until the beams each contain around 2×10^{12} particles. From 20 GeV, the electrons and positrons are accelerated, in opposite directions, up to energies of about 45 GeV. The beams of electrons and positrons can attain luminosities of the order of $10^{31}\text{cm}^{-2}\text{s}^{-1}$. Each of these beams consists of four bunches, which are synchronized to allow simultaneous collisions to occur at four points sited on the LEP ring. At these sites are the four LEP experiments known as ALEPH, DELPHI, OPAL and L3; housed in huge underground experimental halls whose positions on the LEP ring are shown in figure 2.2. When LEP is running, the collisions can be sustained for about 12 hours before the beam intensities fall to a level where a new fill is desirable. Losses in beam intensity can be due to collisions with gas molecules inside the beam pipe. Fortunately, the LEP vacuum is very good and the gas pressure of 3×10^{-9} torr is low enough for this not to present a real problem. The second and more important loss mechanism is

the emission of synchrotron radiation, which causes the beam particles to lose energy and fail to maintain their orbit in LEP. The energy loss per particle after each orbit of the ring, δE, is given by equation 2.1.

$$\delta E(\text{MeV}) = \frac{4\pi}{3}\frac{e^2}{R}\beta^3\frac{E^4}{m_e^4}, \tag{2.1}$$

where R is the radius of the LEP ring, m_e is the electron mass, and β is the particle velocity in units of the speed of light. For an electron in LEP this amounts to approximately 260 MeV per revolution. This energy is given back to most of the particles within the bunches by the RF cavities, so the loss in intensity due to particles falling from the beams is gradual. From equation 2.1 it can be seen that the energy loss is inversely proportional to the radius of the accelerator. This was one of the many factors which had to be taken into consideration in the design of LEP. A summary of the main parameters of LEP is given in table 2.1.

In the present stage of operation, known as LEP 1, a maximum centre of mass energy of around 110 GeV is attainable. In the next stage, which will commence in 1994, this energy will be stepped up to around 200 GeV. So the physics analysis will move away from the Z^0 pole and will be conducted near the W^+W^- pair production threshold. For the upgrade the RF power has to be increased from 16 MW to 48 MW. This will be done by replacing the copper coupled RF cavities by superconducting ones.

The physics results presented here were obtained using the ALEPH detector. In the following sections of this chapter, a short overview of the ALEPH subdetector components is given. Then greater attention is paid to the TPC and ECAL subdetectors, which are the principal devices used in this analysis for the identification of radiative muon pair events. Also, since the measurement of the total cross-section requires knowledge of the total integrated luminosity, the detectors used to obtain this information will be described.

Circumference of LEP	26.658	km
Inner diameter of the tunnel	3.80	m
Radius of curvature in one dipole	3096	m
Total number of intersections	8	
Injection energy	20	GeV
Number of e^+ and e^- bunches	4	
Bunch length	0.013 to 0.04	m
Maximum luminosity	1.7×10^{31}	$cm^{-2}s^{-1}$
Circulating current per beam	3.0	mA
Equipped Experimental areas	4	
Number of iron-concrete dipoles	3304	
Total number of quadrupoles	816	
Number of focusing sextupoles	248	
Number of defocusing sextupoles	256	
Synchrotron energy loss per particle	260	MeV/turn
Total synchrotron radiation power	1.6	MW

Table 2.1: *The LEP parameters.*

2.2 ALEPH : Apparatus for LEP Physics

ALEPH was designed for the study of the decay products of the Z^0. In typical events there can be around 40 neutral and charged particles, which are distributed over the whole solid angle. The event rate at LEP is about 1 Hz at the Z^0 pole, which is low when compared with fixed-target experiments and hadron colliders. Therefore, the ALEPH detector was designed to cover as much of the total solid angle as was practically possible, and to collect the maximum amount of information from each event. The general layout of ALEPH is shown in figure 2.3.

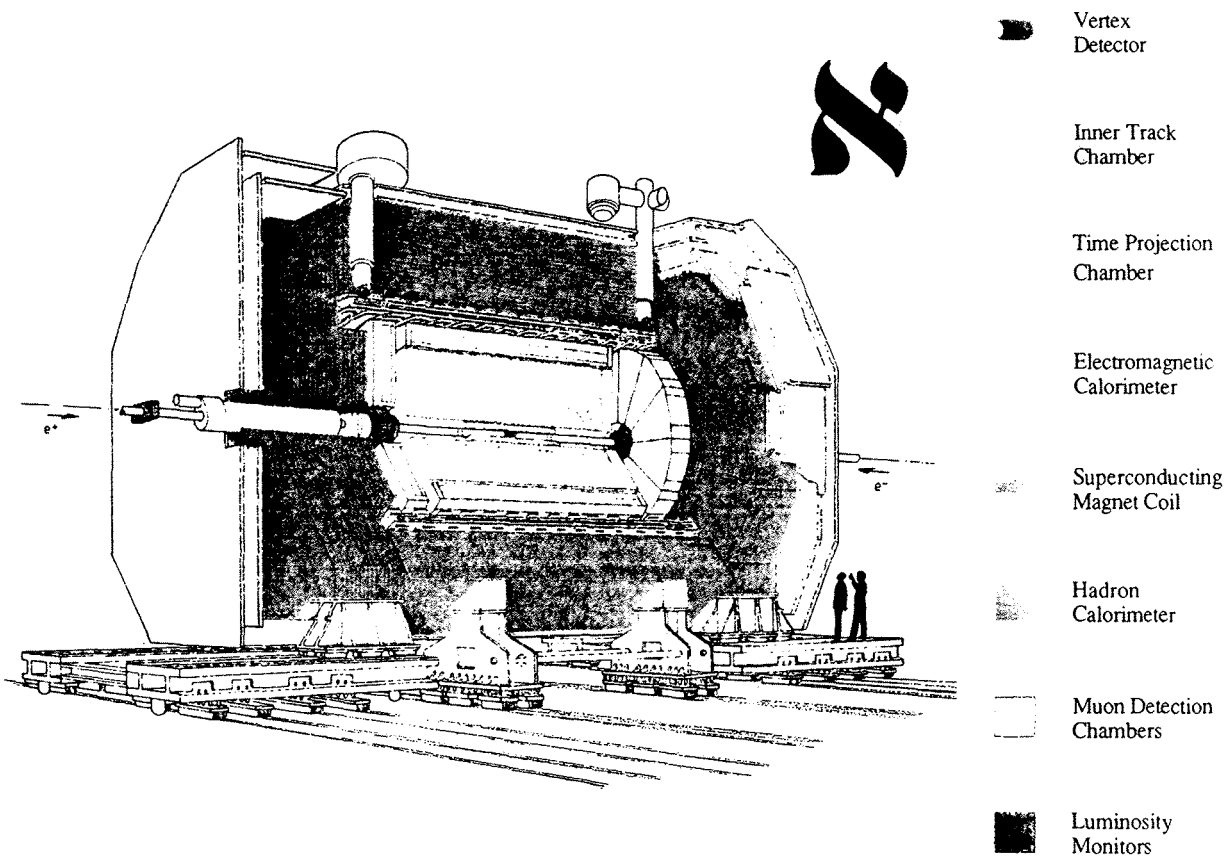

Figure 2.3: *The Aleph Detector.*

ALEPH is sited in an experimental hall 143 m below ground level. It was built in three main sections, a barrel and two endcaps, which form a cylinder surrounding the beam pipe. This was done to ease the assembly and maintenance of the subdetectors.

The subdetectors which make up the ALEPH detector can be separated into two types: tracking detectors, which determine the trajectories of charged particles, and calorimeters, which are used to measure energy deposition. In the tracking detectors, the momenta of the charged particles are obtained from the curvature of their tracks in the presence of a magnetic field. This field is provided by a large superconducting solenoid which surrounds the LEP beam pipe and produces an axial field of 1.5 T. The

solenoid is 5.3 m in diameter and 6.4 m in length.

In 1990 and 1991, ALEPH had two tracking detectors inside the solenoid, each cylindrical in shape and centred on the interaction point. The outer track detector is known as the time projection chamber (TPC). The TPC is a drift chamber which is used for making measurements of all track segments in three dimensions, and to perform momentum measurements. It can also be used for particle identification, via dE/dx measurements of the tracks. This subdetector is described in more detail in section 2.3.

The readout time of the TPC is approximately 45 μs, and as the bunch crossings at ALEPH occur every 22 μs, two events are lost before the TPC is ready to work again. The TPC cannot therefore be used to trigger ALEPH, and to perform this essential function a second tracking device is located immediately inside the TPC. This is known as the inner tracking chamber (ITC). It is a cylindrical multiwire drift chamber which is used to produce a fast trigger signal for charged particles emerging from the interaction region, i.e. within 2-3μs of the beam crossing. The sense wires in the ITC are in eight layers, and run parallel to the beam axis from 13 cm to 29 cm in radius. Charged particles with polar angles in the range 14° to 166° traverse all eight layers. The ITC can provide up to eight accurate r-ϕ coordinates for every track by measuring the drift time to the sense wires, giving a precision of about 100 μm. The z-coordinates are obtained by measuring the difference in the arrival times of pulses at the two ends of each sense wire. The z resolution is about 3 cm and is much poorer than that attainable by the TPC. When the ITC and TPC are used together the transverse momentum of a track, p_T, can be determined to an accuracy of $\Delta p_T/p_T^2 \simeq 10^{-3}\,(\mathrm{GeV/c})^{-1}$.

The calorimeter closest to the beam line is called the electromagnetic calorimeter (ECAL). This surrounds the tracking detectors, but is itself still within the solenoid. Its position was chosen in order to minimize the amount of material that the particles have to pass through before reaching the ECAL. The ECAL is made from

a lead/proportional-chamber sandwich, and is used to sample the electromagnetic showers which are induced in the lead by the outgoing particles. It is built in three subsections, each of differing depths, and is read out in 73,728 towers which point towards the vertex. It was designed for good electron and photon identification and has a high spatial resolution. The ECAL is described in more detail in section 2.4.

Surrounding the solenoid is the hadron calorimeter (HCAL), a 23 layer iron/streamer-tube sampling calorimeter read out in a similar way to the ECAL in 4788 projective towers. The iron structure of the HCAL provides the main support for all of the subdectors, and acts as a return yoke for the solenoid. The HCAL covers a polar angle range from 6° to 174° and its function is to measure hadronic energy deposits and detect muons. The former is achieved using the analogue readout of the projective towers, while the latter relies mainly on a digital readout of hit tubes. In the final layer of ALEPH are a set of muon chambers, which are composed of two double layers of limited streamer tubes. These provide hit coordinates for the muons which are the most penetrating particles of all.

In 1990 the ALEPH beam pipe was made from an alloy of aluminium (96%) and magnesium (3.2%) and had a diameter of 156 mm and a thickness of 0.5 mm. In 1991 this was replaced by a beam pipe made from beryllium which had a diameter of 106 mm and a thickness of 1 mm. This reduced the effective thickness of the beampipe from 0.56% of a radiation length to 0.312%.

The closest detector to the beam pipe is a silicon strip vertex detector. This was designed to obtain extra track coordinates for resolving the secondary vertices of short-lived particles. It is constructed from two double layers of silicon strips arranged in a dodecagonal structure around the LEP beam pipe, and covers an angular range of $44° \leq \theta \leq 136°$. Very little of this detector was in place in 1990 and it is not used in this analysis.

From the measurement of small angle Bhabha scattering the absolute luminosity

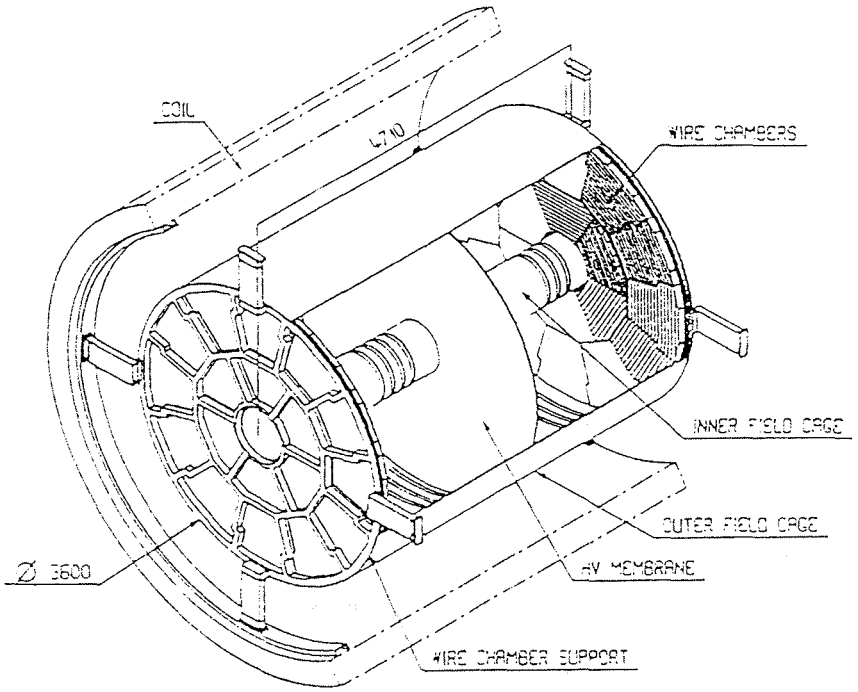

Figure 2.4: *Overall view of the TPC.*

supplied to ALEPH can be determined. For this purpose there is a set of subdetectors in position around the beam pipe, on either side of the interaction vertex, and these are described in section 2.5.

A full explanation of the ALEPH detector and its components can be found in references [44,45].

2.3 The Time Projection Chamber

2.3.1 Introduction

The time projection chamber (TPC) is the main charged particle tracking device in ALEPH. It can provide coordinates for each track in three dimensions, i.e. (r,ϕ,z), and has the ability to measure track momenta and emission angles with good resolution. Also, ionization density (dE/dx) measurements can be made, which provide a method of particle identification. An overall view of the TPC is shown in figure 2.4. It is cylindrical in construction with its axis parallel to the ALEPH magnetic field. The

chamber is formed from two coaxial cylinders, called the inner and outer field cages, and is closed at each end by an end-plate. Also the chamber is subdivided into two halves by a central membrane.

The TPC has an axial electric drift field which is created by a difference in potential between the central membrane and the end-plates. The charged particles created from the e^+e^- annihilations pass through the chamber and ionize the gas inside the TPC. The electrons which are produced from this drift along the E-field lines towards one end of the TPC where they induce ionization avalanches in a set of wire chambers fixed to the end-plate. In total there are 18 wire chambers or 'sectors' mounted on each end-plate. From the signals derived from the wire chambers, the arrival time and the impact point of the drift electrons can be obtained. The z-coordinate is determined from the drift time and the known drift velocity in the TPC. The r-ϕ coordinate is found from the signals which are induced on a set of cathode 'pads', which are situated on the wire chambers. The r-coordinate is found from the radial position of the pads giving the signals, and the ϕ coordinate is calculated from a gaussian model fit to the pads charge response. The methods employed to obtain these coordinates are described in more detail in section 3.4

The momenta of the charged particles emerging from the vertex are obtained in the following way. Charged particles spiral in the ALEPH magnetic field and so their trajectories are helical. The projection of this helix onto an end-plate is the arc of a circle. The momentum can be obtained because the measurement of the sagitta of this arc yields the radius of curvature, which is proportional to the modulus of the component of momentum perpendicular to the magnetic field. The transverse momentum resolution Δp_T [GeV/c] is proportional to the resolution in the sagitta measurement Δs [mm] and this relation is given by equation 2.2.

$$\frac{\Delta p_T}{p_T} = 0.027 p_T \frac{\Delta s}{\ell^2 B} \tag{2.2}$$

where B [T] is the modulus of the magnetic field in tesla and ℓ [m] is the length of the projected trajectory.

The construction and operation of the main components of the TPC will now be described.

2.3.2 The TPC Field Cages

The coaxial cylinders which form the inner and outer field cages of the TPC are both 4.4 m in length and have diameters of 0.6 m and 3.6 m respectively. The outer cylinder consists of two aluminium skins which are kept apart by an aluminium honeycomb spacer. A similar design is used for the inner cylinder except that the honeycomb spacer is made from nomex. The TPC is divided into two halves by a central membrane which is made from a 25 μm thick mylar sheet, coated with conducting graphite paint. At the outer and inner periphery there are two rings of 0.33 mm thick mylar which are used to support the membrane. Also the tension in this membrane is supported by a $10 \times 8\,\mathrm{mm}^2$ aluminium ring, which is glued onto the outer cylinder.

The drift field within the TPC volume is shaped by the coaxial cylinders, the central membrane, and the end-plate sectors. The end-plates are at ground potential and the membrane is at −27 kV. This produces a drift field of $115\,\mathrm{Vcm}^{-1}$. The surfaces of the inner and outer cylinders, which are at earth potential, are covered with electrodes which are all at high potentials. These keep the drift field between them constant and parallel to the axis. An electrical insulator between the cylinders and the electrodes is required so a 75 μm sheet of kapton is used. The structure of these electrodes can be seen in figure 2.5. The electrodes are formed from copper bands each of pitch 10.16 mm. These are separated by gaps of 1.55 mm, and are positioned as two layers on either side of the insulating sheet. For the outer cylinder these bands are 35 μm thick, for the inner cylinder they are 19 μm thick. The electrodes on both sides of the kapton are staggered, in order to increase the uniformity of the drift field, and to shield the TPC

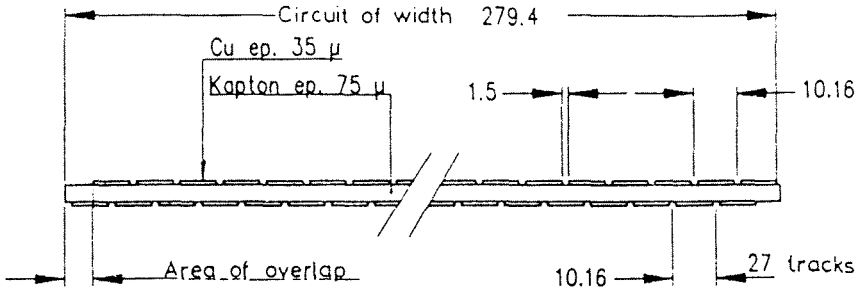

Figure 2.5: *The TPC electrode structure.*

volume from high fields in the insulator.

The gaseous medium contained within the volume of the TPC is a non-flammable mixture of argon (91 %) and methane (9 %) which is held at atmospheric pressure and a temperature of 21° C.

In the electric field of the TPC the drift velocity of the electrons, which are liberated by the ionization of the gas, is about 5.2 cm/μs.

2.3.3 The Wire Chambers

The 18 wire chambers are arranged in the staggered structure shown in figure 2.6. This layout ensures only small loss of tracks at the sector boundaries.

There are three different types of sector. In each end-plate there are 6 sectors which are labelled K (Kind), surrounded by a ring of 12 alternating sectors labelled M (Mann) and W (Weib). The structure of these sectors can be seen in figure 2.7. Also shown in figure 2.7 are the positions of the cathode pads within the sectors.

The cathode pads have dimensions $\sim 6 \times 30\,\mathrm{mm}^2$ with a pitch of about 7 mm. Between the radii of 399 mm and 1706 mm there are 21 pad rows. Each K sector consists of 9 rows of pads with a total of 909 pads. The W and M type sectors both contain 12 pad rows; in each W sector there are 1182 pads, and in an M sector 1326 pads. Altogether there are 41,004 pads within the TPC. Positioned in between the pad

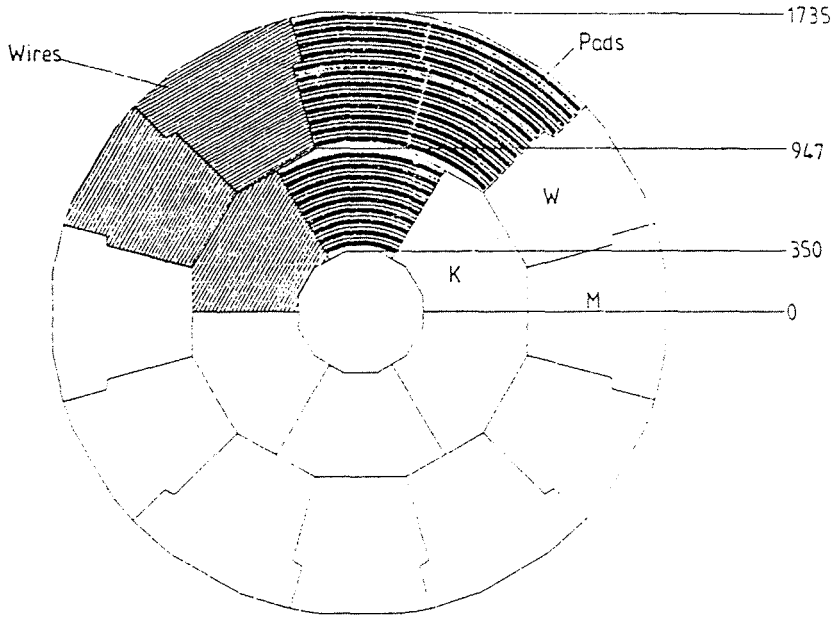

Figure 2.6: *The overall geometry of a TPC end-plate.*

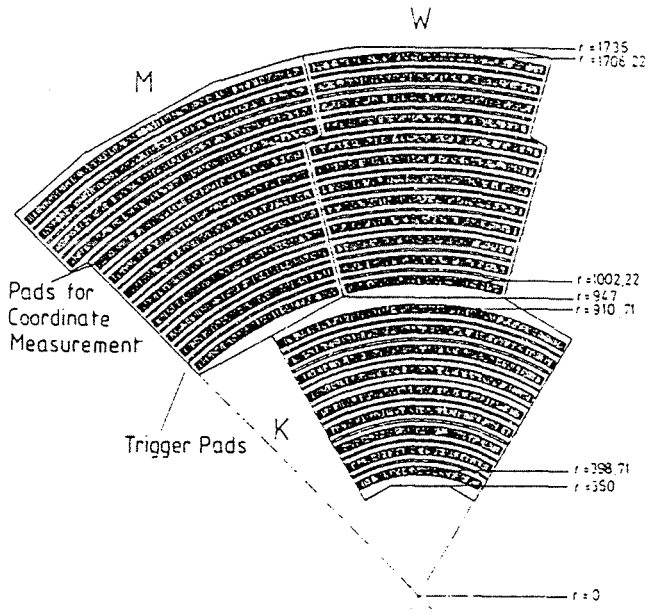

Figure 2.7: *A more detailed view of the M, W, and K sectors.*

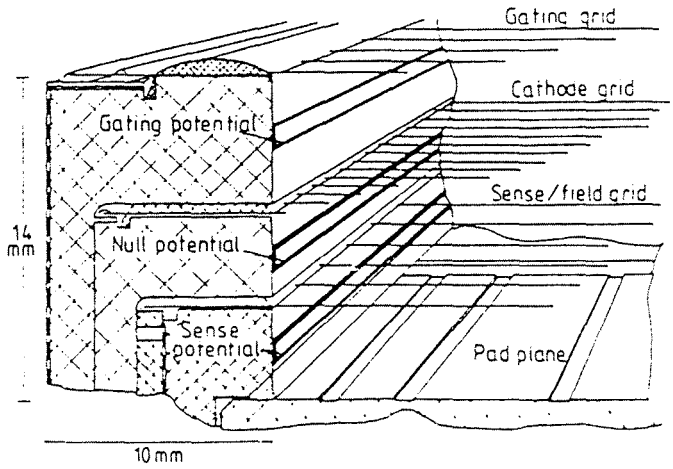

Figure 2.8: *Schematic diagram of a sector edge, showing wire attachments, pad plane, wire grids, and potential strips.*

rows there are long 'trigger' pads. These are used for the second level trigger, which is explained in section 3.2. The trigger pads are 6.3 mm wide in r and subtend an angle of 15° in ϕ, except for the five outermost rows where each pad subtends 7.5° in ϕ.

The sectors are made from an aluminium sandwich onto which is glued a copper clad, glass fibre reinforced, epoxy sheet. This sheet has the pads milled onto its surface. These pads are all connected to preamplifiers via wires which pass through the sandwich structure.

In each of the sectors there are 3 wire planes and these are illustrated in figure 2.8 which shows a schematic diagram of the wire attachments to the TPC sector edge. The first of these planes is called the gating grid and this is explained in section 2.3.4. This is followed by a cathode wire plane, and finally by a sense wire plane which is interleaved by field shaping wires. The sense wires are formed from gold plated tungsten wires 0.02 mm in diameter which are at a positive potential of around 1400 V. In the same layer as the sense wires are a set of 0.127 mm gold plated copper field wires. These alternate with the sense wires and are used to shape the field in such a way that the

drift electrons are made to avalanche towards the sense wires. The next layer of wires is the cathode grid. Its purpose is to define the end of the main drift field. The wires in this plane are made from 0.076 mm copper wires which are at earth potential and are 4 mm away from the sense layer. These wires screen the main drift field from the high fields produced by the sense wires.

The ionization avalanches, which are created around the sense wires by the drift electrons, induce signals on the cathode pads which are 4 mm away from the sense wires. The signals on these pads are then read out to give position and timing information for the charged particles. The signals on the wires are used to obtain dE/dx information. There are 330 possible dE/dx wire signals per track which can be used to determine this quantity.

2.3.4 The Gating Grid

The gating grid is positioned at a distance of 6 mm away from the cathode wire plane and it consists of a set of 0.076 mm diameter copper wires. The purpose of this plane of wires is to stop positive ions from getting into the drift region. When ionization avalanches occur near the sense wires, large numbers of positive ions are formed which can enter the drift region. This creates a space charge which modifies the local electric fields, and so the tracks can be distorted. The TPC operates in a continuous, sensitive mode, and that is why the grid is needed. The gating grid works in the following way. The gate can be in either an open or closed state. When the gate is open the wires are at a potential of $V_g = -67$ V. This allows all charged particles to move unhindered. When the gate is closed alternate wires in the grid have the potentials $V_g + \Delta V_g$ and $V_g - \Delta V_g$. This produces a dipole field which does not allow the charged particles to pass. To stop the heavy slow moving positive ions a potential of $\Delta V_g \geq 40$ V is required. A larger potential of ~ 150 V is needed to stop incoming electrons. This is because the force exerted by the magnetic field is proportional to the particles velocity,

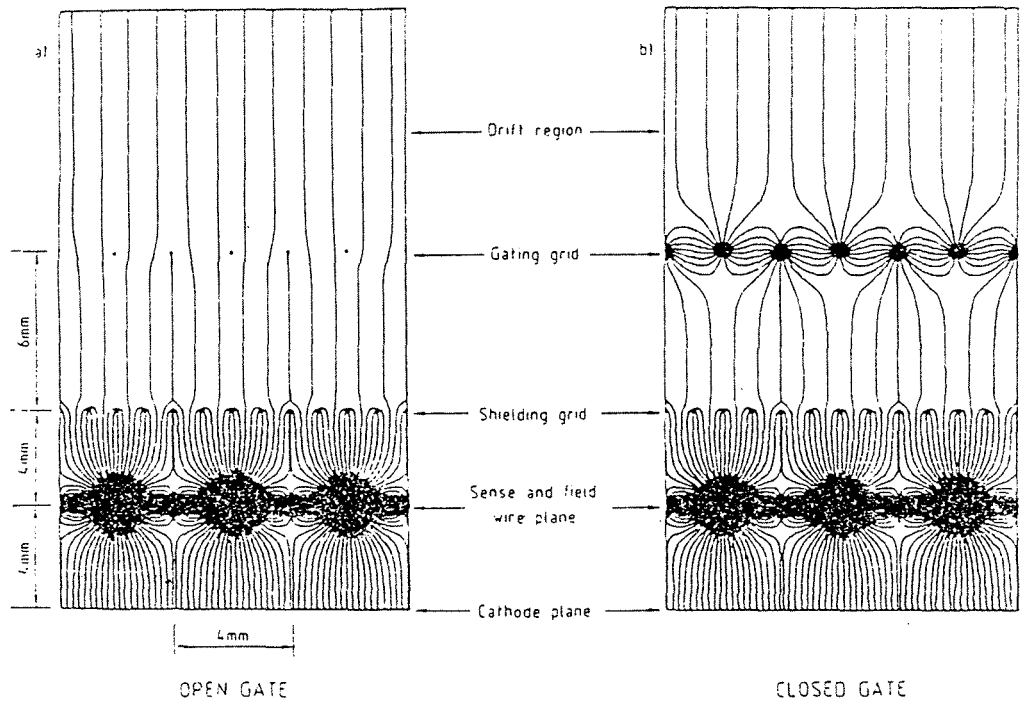

Figure 2.9: *The gating grid of the TPC with electric field lines; (a) gate open, (b) gate closed.*

and so is greater for the fast moving, light electrons, than for the heavier slow moving ions.

At a period of 3 μs before the beam crossing time the grid is opened. If there is a level-1 trigger 'no', then it is closed 5.5 μs after the bunch crossing. If a level-1 trigger 'yes' is received, then the gate is kept open for a time of 45 μs. This is the maximum time needed by the drift electrons to travel the full distance between the central membrane and one end-plate.

The pattern of E-field lines surrounding the wires inside the TPC is shown in figure 2.9 for the cases when the gating grid is on and also off.

2.3.5 Laser Calibration

The TPC has a laser system for field calibration. This is used to measure the vector of the drift velocity within the TPC and can provide information on particle track distortions. This system comprises two ultraviolet lasers. When these are fired into the volume of the TPC, 30 straight ionization tracks are produced which are arranged to originate approximately from the interaction point. The curvature of these tracks is measured and used to correct the sagitta of the particle tracks. The drift velocity is determined from the reconstructed polar angles. Also this system can be used to correct for any inhomogeneities in the electric or magnetic field.

The lasers are mounted on top of a platform above the magnet. From this position the laser beams have a path length of about 10 m. Initially each beam is steered by a system of mirrors to one end of the TPC. The beams then pass through splitter rings. These rings surround the vacuum pipe at a radius between 35 cm and 40 cm. The beam is split into 3 rays of equal intensity which travel into the volume of the TPC along axial paths close to the surface of the inner field cage. The beams then pass through four semitransparent mirrors and one pentaprism that directs a fraction of the laser light towards the volume of the TPC. This creates ionization tracks at the polar angles θ of 18°, 30°, 39°, 67° and 90° and at three azimuthal angles ϕ of 84°, 204° and 324°.

2.3.6 TPC Performance

The general performance of the TPC is summarized in table 2.2. The r-ϕ resolution depends upon the angle of the track segment with respect to the wires and pads, and also on the magnetic field, which determines the rate of diffusion of the drifting electrons. The main systematic contribution to the z spatial resolution is from the drift time. At low angles θ with respect to the beam line, poorer spatial resolutions are obtained due to the signal on the pads being much longer in time. Also the z spatial resolution becomes worse for low momentum tracks where the pad crossing angle is large. The

r-ϕ spatial resolution:			
	Pad crossing angle	0^o	10^o
	Resolution:	160 μm	400 μm
z spatial resolution:			
	$\theta =$	90^o	45^o 20^o
	Resolution per pad row:	1 mm	2 mm 5 mm
	Resolution per wire:	3 mm	2 mm 2 mm
Momentum resolution:			
	$\Delta p/p \approx$	$1.5 \times 10^{-3} p\,(\mathrm{GeV/c})^{-1}$	

Table 2.2: *The performance of the TPC.*

momentum resolution depends on two factors, the first being multiple scattering by gas molecules within the TPC chamber and the second the polar angle of the track. Tracks which are produced at low angles with respect to the beam line only generate a few space points along the track and a short track length in the r-ϕ projection, reducing the resolution. The momentum resolution can also be affected by any inhomogeneities in the electric and magnetic fields.

2.4 The Electromagnetic Calorimeter

2.4.1 Introduction

The electromagnetic calorimeter (ECAL) was designed for good electron and photon identification, with high spatial and energy resolutions. An overall view of the ECAL is shown in figure 2.10. This is a 45 layer lead/proportional wire-chamber sampling device, which is 22 radiation lengths (X_0) thick and is built from 3 main assemblies, a barrel section and two end-caps.

The readout from the ECAL comes from signals which are induced on wire planes

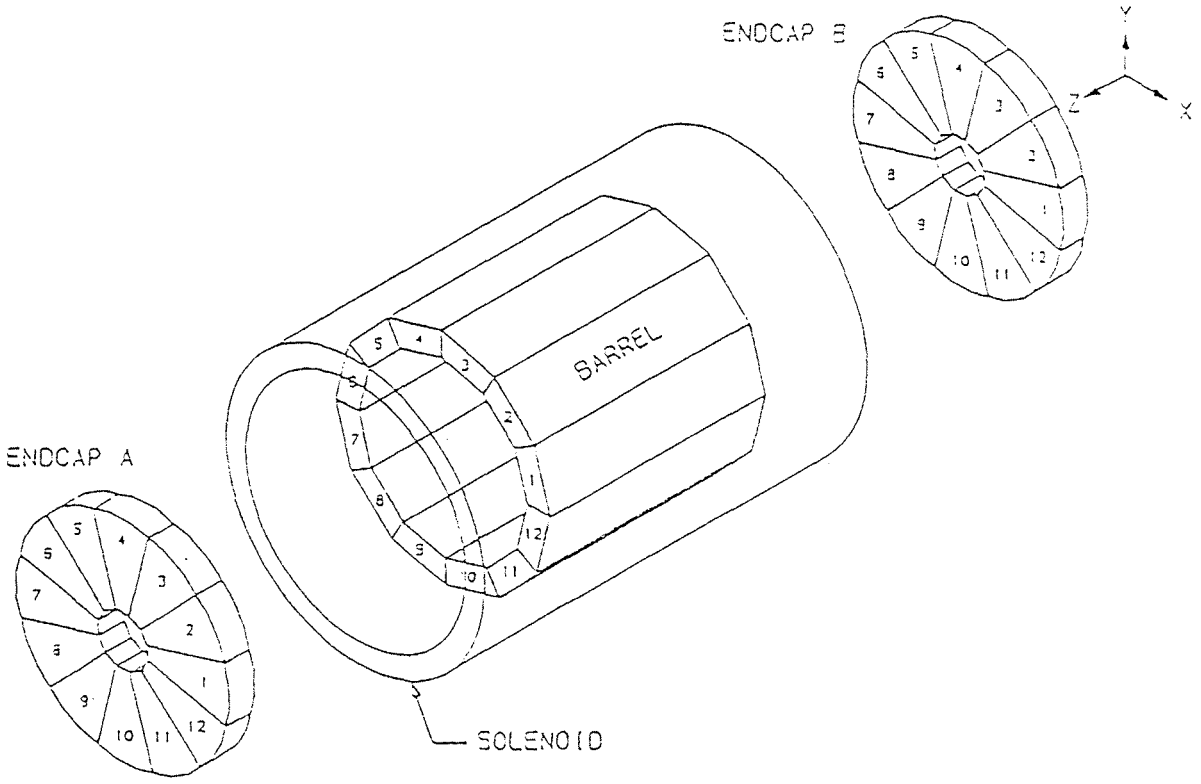

Figure 2.10: *An overall view of the Electromagnetic Calorimeter.*

and a set of cathode pads. The ECAL is built in three levels called 'stacks'. The first stack has 10 layers of 2 mm thick lead ($4X_0$), the second contains 23 layers of 2 mm thick lead ($9X_0$), and the third consists of 12 layers of 4 mm thick lead ($9X_0$). The average radiation length in stacks 1 and 2 is between 2.0 cm and 2.4 cm, and in stack 3 it is 1.4 cm. The cathode pads are connected internally to form 'towers' which point towards the interaction vertex. The towers are read out from three sections in depth corresponding to the three stacks, and these are known as 'storeys'. Altogether there are 73,728 towers which cover 3.9π sr of the solid angle with polar angle coverage down to 12° above the beam axis. A further 6 % of the end-cap and 2 % of the barrel acceptance is affected by the existence of cracks between ECAL modules. Nonetheless the ECAL is a comparatively hermetic detector and the small size of the cathode pads

gives it extremely high granularity.

2.4.2 Calorimeter Construction and Operation

The main assemblies of the ECAL are divided into modules. The barrel is built from 12 modules each subtending an angle of 30° in azimuthal angle ϕ, and weighing about 10.4 tonnes. The end-caps are each built from 12 modules which are known as 'petals'. These subtend the same angle in ϕ as those in the barrel, and weigh approximately 2.6 tonnes.

Figures 2.11 and 2.12 show the structure of a barrel and an end-cap module respectively. The main difference between the barrel and end-cap modules is in their

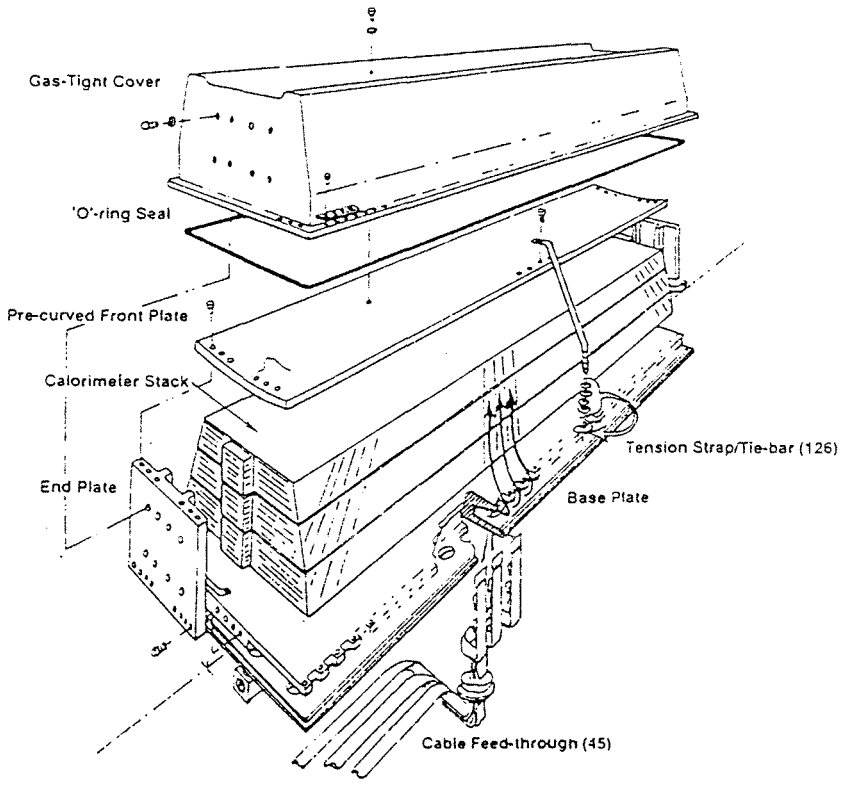

Figure 2.11: *The structure of an ECAL barrel module.*

shapes, which were chosen in order to cover as much of the solid angle as possible. The barrel modules are 4774 mm long and are 448 mm in thickness. They are trapezoidal in

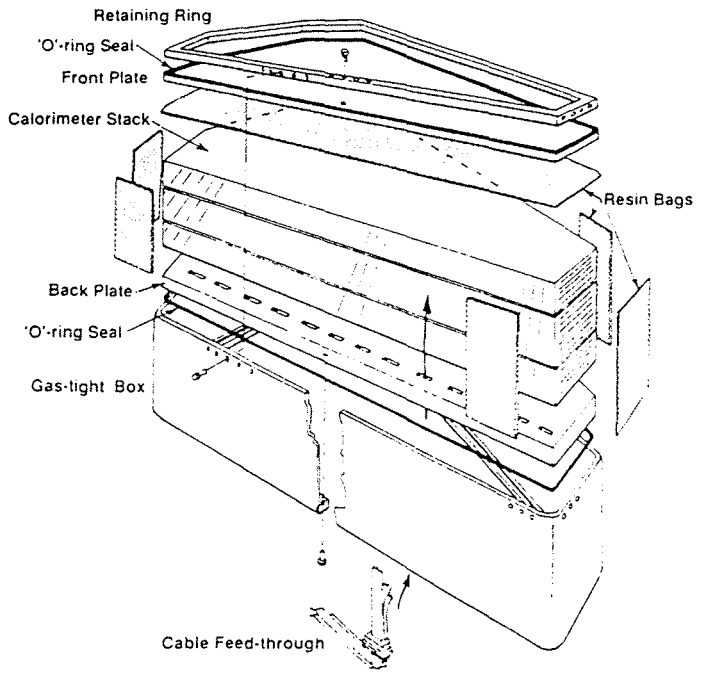

Figure 2.12: *The structure of an ECAL end-cap module.*

cross-section with a width varying from 984 mm at the inner surface to 1224 mm at the outer surface. The inner radius of the barrel is 1850 mm as measured to the centre of the front plate of each module. In the end-caps the petals are positioned in a circular arrangement with an inner radius of 564 mm and an outer radius of 2350 mm. The thickness of each of these modules is 526 mm.

The modules within the end-cap are rotated by $-1.875°$ with respect to the barrel and the whole of the ECAL is rotated by 15° with respect to the hadron calorimeter, ensuring that cracks do not overlap. This helps to reduce the number of undetected particles.

Each module is constructed from a 45 layer lead/proportional wire chamber sandwich. The structure of one layer is shown in figure 2.13. The wire chambers are formed from an aluminium 'comb' extrusion. The channels which are formed have inner

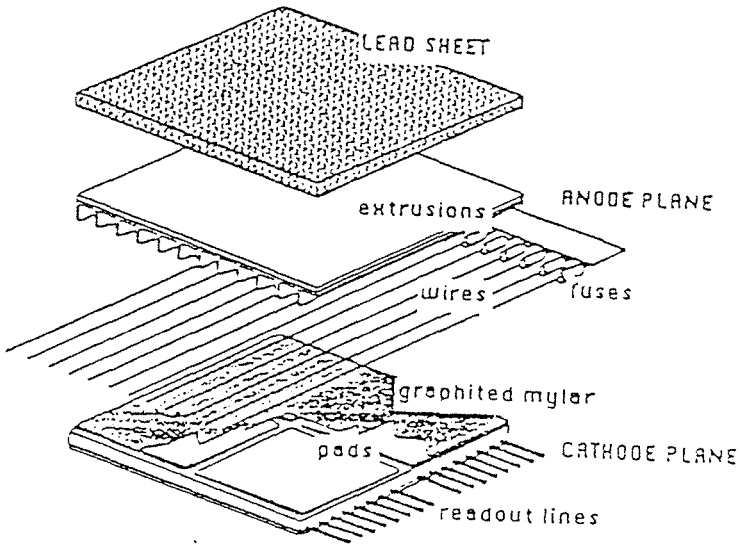

Figure 2.13: *A typical layer in the Electromagnetic Calorimeter.*

dimensions 3.2 mm × 4.5 mm, with a rib thickness of 0.5 mm, and a base which is 0.6 mm thick. Along these channels pass the anode wires. These are 25 μm diameter gold plated tungsten wires which operate in the proportional mode at a potential of $\sim$ 1400 V. These wire chambers work using a gas mixture of xenon(80 %) and CO_2 (20 %) at approximately 60 mbar above atmospheric pressure. The wires contained within the barrel modules run parallel to the beam line. Those wires within the end-caps run parallel to the left hand edge of a petal when viewed from the outside of ALEPH with the broad end uppermost. Closing the open side of the wire chamber cells are copper cathode pads which are placed behind highly resistive, graphite coated, mylar 'windows'. The pads have dimensions $\sim 30 \times 30\,\mathrm{mm}^2$, and are 35 μm thick. The pads from consecutive layers are associated to form the towers pointing towards the vertex.

Ionization from an electromagnetic shower developed in the lead sheets is amplified in avalanches around the wires. The signals on the wires are then induced onto the cathode pads. These signals are then summed independently in the three storeys which make up a tower.

The barrel modules each contain 4096 towers, and both end-caps contain 1024 towers, and since these are read out in three storeys there are 221,184 tower readout channels in total.

Besides the tower readout there are a set of analogue wire signals which are available for each plane. The signals in each plane are summed together so there are 45 wire readouts per module. The wires can also be used to test for missing pads and missing wires within a module.

Over a period of time the temperature and pressure of the gas within the ECAL can vary. This causes the gas gain to change and will alter the calibration constants that are required. In order to monitor these changes there are small wire chambers $3.5\times$ 3.5 $\times$ 20 mm^3 contained within each module. These contain an Fe^{55} radioactive source. The charge collected on the wires, initiated by the 6 keV X-rays from these sources, can be measured and the gas variations followed.

The energy and position resolutions within the ECAL are summarised in table 2.3. These quantities were obtained from a combination of Monte Carlo, test beam studies

Energy Resolution:	$\sigma_E/E = 0.18\ GeV^{1/2}/\sqrt{E}$
Position Resolution:	$\sigma_x = \sigma_y = 6.8\ mm\ GeV^{1/2}/\sqrt{E}$
Granularity at $\theta = 90°$ (barrel):	$17 \times 17\ (mrad)^2$
Granularity at $\theta = 45°$ (barrel):	$12 \times 12\ (mrad)^2$
Granularity at $\theta = 40°$ (end-cap):	$9 \times 10\ (mrad)^2$
Granularity at $\theta = 27°$ (end-cap):	$10 \times 14\ (mrad)^2$

Table 2.3: *The ECAL resolutions parameters.*

and cosmic ray tests [46,47,48]. Table 2.3 also shows the granularity of the ECAL towers for different polar angles.

2.5 The Luminosity Monitors

The determination of the luminosity delivered by LEP and detected by ALEPH is of great importance. This is because this information is required in cross-section determinations as expressed by equation 2.3.

$$\sigma = \frac{N}{\epsilon \int \mathcal{L} dt} \tag{2.3}$$

Here, N is the number of events produced, ϵ is the overall detection efficiency and $\mathcal{L}$ is the luminosity. The same expression is used to determine the luminosity from the measured number of events due to a process with known, large cross-section. For an e^+e^- collider like LEP the ideal reference reaction is small-angle Bhabha scattering. This process is very well known from QED and the differential cross-section in the lowest order of α, for small scattering angles θ and electron beam energy E, is given by equation 2.4.

$$\frac{d\sigma}{d\Omega} = \frac{4\alpha^2(\hbar c)^2}{E^2\theta^4} \tag{2.4}$$

The number of events in which a scattered electron and positron are detected in coincidence on both sides of the interaction point is counted using the luminosity monitors. These monitors consist of two instruments, the luminosity calorimeter (LCAL), and the small angle tracking device (SATR). One tracker and calorimeter together form one monitor, and these are positioned approximately 2.7 m on either side of the interaction vertex. Using this combination of detectors the systematic uncertainty in the luminosity measurement was reduced to 0.67 % for the 1990 data set and 0.54 % for 1991.

The SATR is made up from a set of drift tubes which are capable of detecting scattered particles with polar angles in the range 40-90 mrad. The LCAL accepts the particles between 45 mrad and 155 mrad. This is formed from a lead/proportional-tube sandwich which has a similar structure to that of the ECAL. There is an overlap

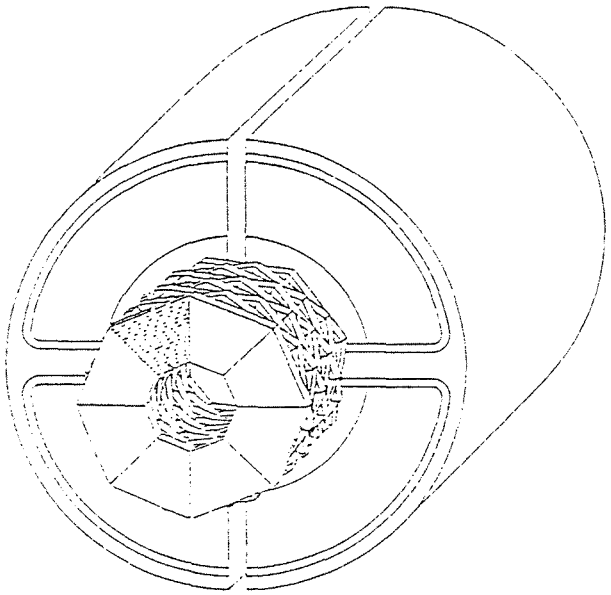

Figure 2.14: *One half of the main luminosity monitor.*

region between these two detectors, in the range 45-90 mrad. The arrangement of these detectors is shown in figure 2.14.

Chapter 3

Data Acquisition and Event Reconstruction

3.1 Introduction

In an e^+e^- annihilation the decay products of the Z^0 boson are sprayed outwards with a range of directions and momenta. As well as these e^+e^- events there are other kinds of events which can occur around the vertex such as cosmic ray showers, beam-gas interactions, and off-momentum beam particles hitting the edges of the collimators or the vacuum chamber walls. These background events are not of relevance to the physics under study at LEP. It is the purpose of the ALEPH trigger and data acquisition systems to reduce these backgrounds to a manageable level, and also to read in the information from as many real Z^0 decay events as possible. In each event over 700,000 electronics channels have to be read out from eight subdetectors and the average event size is over 100 kilobytes. To cope with this very well organized trigger and data acquisition systems are required. These are discussed in section 3.2 and section 3.3 respectively.

When the wire and pad signals from the detector have been obtained by the data

acquisition system they must then be processed in order that the real physics event which caused them can be reconstructed. This event reconstruction procedure is explained in section 3.4.

3.2 The Trigger System

There are several criteria which must be met to ensure that the ALEPH trigger system [49,50] is effective. The frequency at which the triggers fire must be low enough to permit the gating of the TPC, i.e. to allow sufficient time when the gating grid is on to prevent the build up of space charge. Also, the rate of triggering must be such that the dead time in the readout of the front-end electronics is low. Finally, the trigger system must not exceed the rate acceptable for writing data to disk.

The physics triggers for the trigger system are formed using information from the following components:

- tracking detectors
  - ITC track candidates from a dedicated processor
  - TPC track candidates from a dedicated processor
- calorimeters
  - ECAL signals from wires and towers
  - LCAL signals from wires and towers
  - HCAL signals from wires and towers

The detector is subdivided into trigger segments which follow closely the mechanical structure of both the ECAL and HCAL modules. The signals obtained from the segments of a detector which are above a preset threshold are ORed to provide a trigger for that detector. A total of 32 physics triggers from combinations of different detector triggers are possible. The physics triggers which were in use in 1990 and 1991

Trigger	Sub-detectors used
Single muon	HCAL,ITC,TPC
Single charged electromagnetic energy	ECAL,ITC,TPC
Single neutral electromagnetic energy	ECAL
Single charged hadronic energy	HCAL,ITC,TPC
Single neutral hadronic energy	HCAL
Isolated photon (veto LCAL and ITC)	ECAL,LCAL,ITC
Bhabha	LCAL
Single-arm Bhabha	LCAL
Total energy	ECAL and HCAL
Cosmic	ECAL and HCAL
n-tracks	ITC,TPC
Random	

Table 3.1: *The subdetectors employed in trigger formation.*

are listed in table 3.1. After each bunch crossing these triggers are ORed so that a global 'YES/NO' trigger decision can be made. In any e^+e^- interaction several of these triggers may fire, and it is this redundancy which can be used to determine the trigger efficiency. This must be done since the measured cross-sections depend upon it. The determination of this efficiency for $e^+e^- \to \mu^+\mu^-\gamma$ is given in section 4.4.2.

The ALEPH trigger system is separated into three levels of refinement. The level-1 trigger gives a decision on an event within $5\,\mu$s. This is fast in comparison to the $22\,\mu$s interval between successive bunch crossings, so no dead-time is introduced. The rate at which this trigger fires must be at most a few hundred hertz, to keep space charge effects inside the TPC small. The level-1 trigger decision is made using ECAL, HCAL, LCAL and ITC information. If the decision is 'YES', level-2 is invoked. This uses the information from the TPC trigger pads to check for the presence of charged particle

tracks in the TPC coming from the interaction point. A 'YES/NO' decision is then made by recalculating the trigger OR using this new information. A time of about 50 μs is required to make a decision at level-2 due to the TPC drift time. If an event is rejected then the detector must be made ready to accept new data. This takes an extra 17 μs due to the refresh cycle of the ECAL so ALEPH is ready for the third bunch crossing after the trigger, i.e. about 67 μs later. The rate of triggering at level-2 is reduced to about 10 Hz. When a level-2 'YES' is obtained the event is then passed on to level-3. This is a 'software' trigger which runs on a farm of independent computers known as the 'ALEPH Event Processor', and is only applied after the event readout. Level-3 has access to information from all subdetectors which it uses to separate the genuine e^+e^- interactions from the background triggers, and validates them for writing to disk. The trigger rate at this level is reduced to 1-2 Hz, which is an acceptable rate for data storage.

3.3 The Data Acquisition System

The ALEPH data acquisition system (DAQ) [51] has several tasks to perform. Firstly, it must optimize the event processing and minimize the dead time. Secondly, it must synchronize the readout from each subdetector so that only the data from a particular bunch crossing are used to build an event. Finally, it has to reduce the incoming data to a manageable level and produce a formatted output.

The subdetectors can produce over 500 kbytes of raw data every second and this needs to be reduced to about 100 kbytes per second for the transferral to disk. The process of data reduction is achieved via the trigger system, and 'zero suppression'. Zero suppression is the technique in which only the channels having signals above a preselected threshold are read out.

The calibration and formatting of the signals which are read out from the front end

electronics is done using specially designed FASTBUS modules [52] known as readout controllers (ROCs), which are associated to all subdectors. ROCs also perform the tasks of initializing and controlling the readout sequence of the front end electronics, and the digitization and storage of their output signals.

The readout of an event by the DAQ is done in several stages. As the e^+ and e^- bunches approach the interaction region they generate signals in beam pickups which are positioned inside the beam pipe. A timing unit called the 'T0' Module receives these signals and then synchronizes the readout electronics to the accelerator, and tells the system when to expect the next bunch crossing. It generates two signals, an early bunch crossing warning (EBX), and a bunch crossing warning (BX), and these are passed onto modules known as trigger supervisors (TS). The job of the trigger supervisors is to keep track of the readout protocol and the synchronization of all ROCs. If the system is not busy and is ready to take an event, the trigger supervisor warns all ROCs to get ready to receive data, and this is done via a 'gated bunch crossing' signal (GBX). At a time of 5 μs after the bunch crossing the trigger electronics informs the trigger supervisors that a level-1 decision has been made. The trigger decision is then delivered to all ROCs. If there is a level-1 'NO' then the ROCs reset themselves ready for the next GBX signal. If there is a level-1 'YES' then the digitization of the event and its storage on an output buffer is continued. When the level-2 decision has been made the trigger supervisor again informs all ROCs of the outcome. Again a level-2 'NO' decision resets the ROCs ready for the next GBX signal. On a level-2 'YES' the full readout of the event is initiated. Once the data from the front end electronics have been fully digitized and read into a ROCs output buffer, it is then passed onto another FASTBUS module known as an event builder (EB). The subdetector event builders perform the tasks of collecting the data from the ROCs of each subdetector and then building a subevent from this information. The subevents from each EB are then passed onto the main event builder (MEB). The MEB ensures that every EB is read out and that the data

obtained are all from the same event.

The complete physics event is then passed on from the MEB to one of the 'ALEPH Event Processors' which make up the level-3 trigger. If the event passes the level-3 trigger it is then read into an event buffer from where it is written out to disk ready for the reconstruction stage.

To permit the detailed monitoring of subdetector events during data taking without slowing down the on-line system spy channels have been added to the DAQ system. These operate by taking a copy of an event as it passes through a subdetector event builder and then transferring this copy to another computer where the event can be studied without affecting the rate of data taking.

The DAQ system has a main host computer and several subdetector computers. During the 1990 and 1991 data taking periods the main host computer was a VAX 8700 which was used to collect all of the data for storage, on-line analysis, and for event displays. It also had the task of providing common services. During the same period there were three VAX 8200/8250 machines which were used to monitor the main subdetectors, these being the TPC, ECAL, and HCAL. These were also used to gather the 'spy events'.

The event reconstruction is done 'quasi on-line' at the experiment by the ALEPH Event Reconstruction Facility, which is coupled to the main DAQ computer through shared disks. During 1990 and 1991 this facility consisted of a central computer and 12 diskless VAX station 3100 CPUs. Shortly after the end of a physics run the raw data files are made available to the Reconstruction Facility. The central computer does a preliminary scan of the events and this produces an event directory, which contains the address of each event within the files, and also the constants for the reconstruction program. The events are then distributed between the 12 processors for the reconstruction to take place. Once this is complete the events are then joined to form a single file on the central computer, with the order of these events being preserved.

The reconstructed event files are then passed directly to the off-line computers for the physics analysis to begin.

3.4 Event Reconstruction

The reconstruction of the physics events from the electrical signals obtained by ALEPH is done using a large computer program called JULIA (Job to Unveil LEP Interactions in Aleph) [53]. The reconstruction stage is done in three parts. First of all off-line calibrations and corrections are performed on the data from each subdetector. After this has been done JULIA performs the following tasks:

- coordinate finding;
- track fitting;
- calorimeter cluster formation;
- track and calorimeter cluster association;
- dE/dx calculations;
- vertex reconstruction.

Finally, all of this information is used for particle identification.

Since the process under study here, radiative muon pair production, involves only two charged tracks and isolated calorimeter energy deposits, only the track and calorimeter reconstructions are of relevance here and so these will now be explained.

3.4.1 Coordinate Finding

To reconstruct the outgoing particle trajectories, the coordinates of their ITC and TPC hits are found and then tracks are formed by linking these hits together.

The ITC r-ϕ coordinate of a hit is calculated from the drift time to the anode wires of the ionization charge created by the passage of charged particles through the ITC

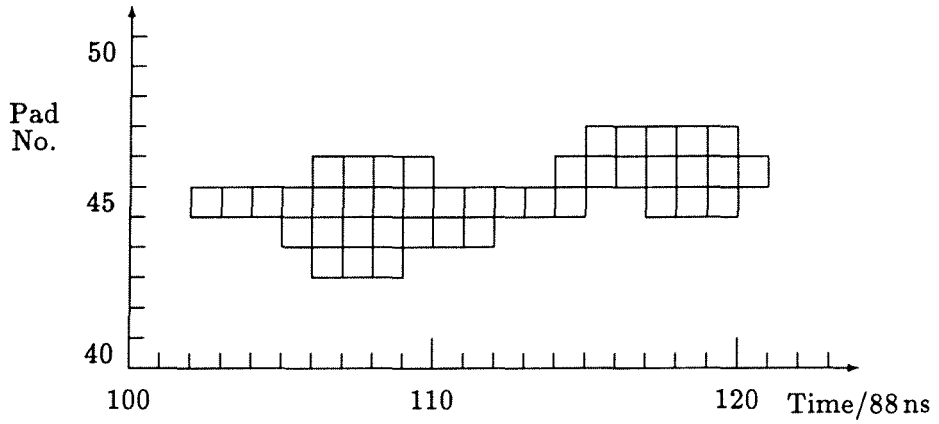

Figure 3.1: *Pad row cluster formed by two nearby tracks.*

gas. The drift time defines a circle around the anode wire on which the coordinate lies. The precise position of this coordinate can only be determined at the track fitting stage. The ITC z coordinate of a hit is obtained by calculating the difference in arrival times of the generated pulses at the ends of the anode wires.

From the measurements of the drift time and the ionization charge produced in the TPC, two pieces of information are obtained which allow the TPC (r,ϕ,z) coordinates to be found, and these are:

- Pad hits. This includes the pad addresses, the pulse arrival times, and the temporal length of the pulses.
- Digitized pulse heights per unit time. The digitization of these pulse heights is done over a period of 512 'time-slices' each of duration 88 ns.

The coordinates of hits produced by tracks in the TPC are found in two steps. Firstly, the plane formed by pad number versus drift time for each pad row is searched to find two dimensional clusters. This plane is illustrated in figure 3.1 which shows the clusters formed by two nearby tracks. Clusters are formed by hits on adjacent pads which overlap by at least one time slice. To obtain a good cluster the following criteria have to be fulfilled.

- $2 \leq number\ of\ pads \leq 20$

- $5 \leq$ *number of time slices* ≤ 35

For the first criterion the upper limit was selected in order to accommodate looping tracks. Any clusters which do not pass these criteria are not used for the track finding phase. After this has been done the second stage is to find the contributions or 'subclusters' within the main cluster which belong to single tracks. In order to do this another object has to be defined: a 'subpulse'. This is a set of time slices within a pulse which has a single maximum in the pulse height distribution. The subclusters are formed from groups of these subpulses from adjacent pads which have a similar drift time. This method of looking for subclusters is demonstrated by figure 3.2, which

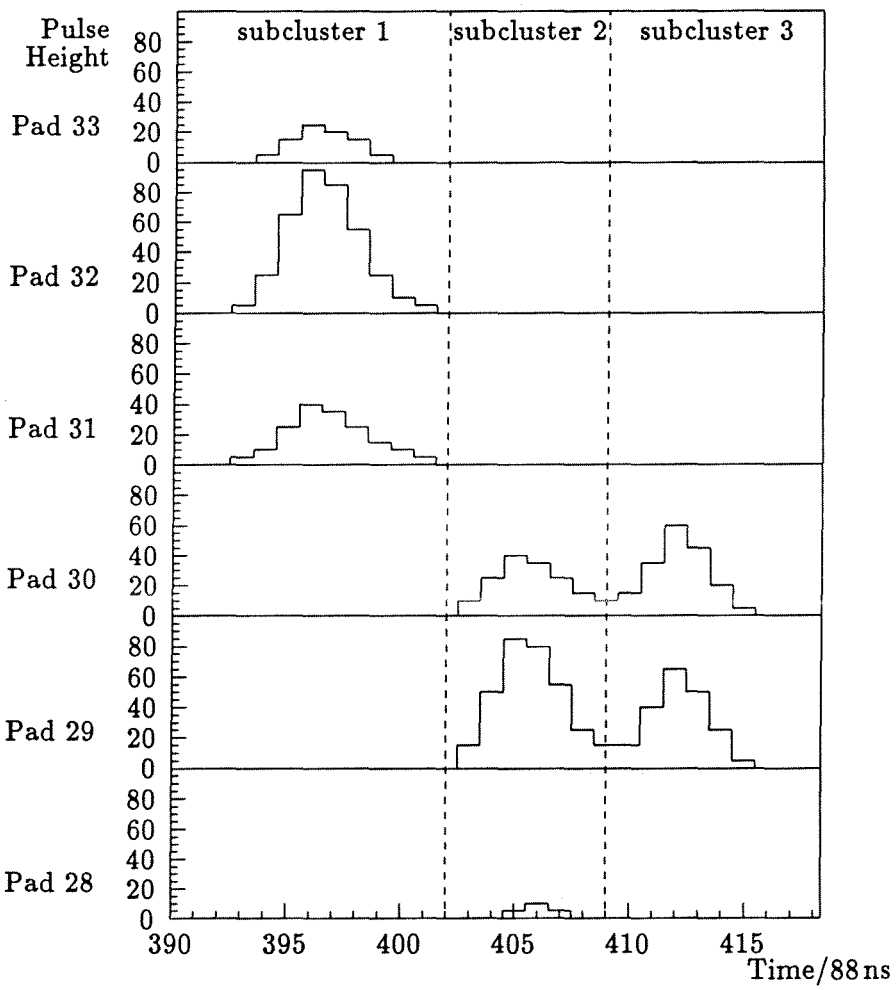

Figure 3.2: *The splitting of a cluster into three subclusters.*

shows how three subclusters can be separated from one main cluster. By looking for maxima in the plane formed by the pulse height distribution versus the pad number, it is possible to divide the subclusters in r-ϕ. This is only done if the number of pads in a subcluster is between 3 and 6. Each of these subclusters is used to calculate a z and r-ϕ coordinate. This is done via charge and time estimators for each subpulse within a subcluster. A measure of the charge of a subpulse is taken to be the sum of all time slices above a threshold of two ADC counts. For the time estimate a threshold is defined as a quarter of the mean sample pulse height for that subpulse. The time estimate is then taken as the halfway point between the threshold crossings on the leading and trailing edge of the subpulse. The determination of the r-ϕ coordinate depends upon the number of pads contained within a subcluster. For subclusters with between 2 and 3 pads, a gaussian fit is made to the response of the pads. A charge weighted mean of the positions of the pads is used if there are more than 3 pads in the subcluster. The z coordinate is calculated from the charge weighted average of subpulse times within the subcluster. The known drift velocity is used to convert the time into a drift length.

3.4.2 Track Fitting

Once the hit coordinates have been determined, JULIA's task is to link these hits into tracks. To do this radially ordered TPC hits consistent with lying on the same helix are linked to form chains. The chains are then combined to form the tracks, and finally the parameters of the tracks are obtained from a fit. In the x-y or r-ϕ plane, tracks appear as arcs of circles, while in the s_{xy}-z plane,[1] they are straight lines. Table 3.2 defines all of the helix parameters, and these are shown in figure 3.3.

A three stage algorithm, which is based on the idea of adding track segments or chains together, is used to associate coordinates to the helices.

The final chains may be linked for two reasons. Firstly, low momentum tracks spiral

[1] s_{xy} is defined as the arc length from the point of closest approach to the vertex.

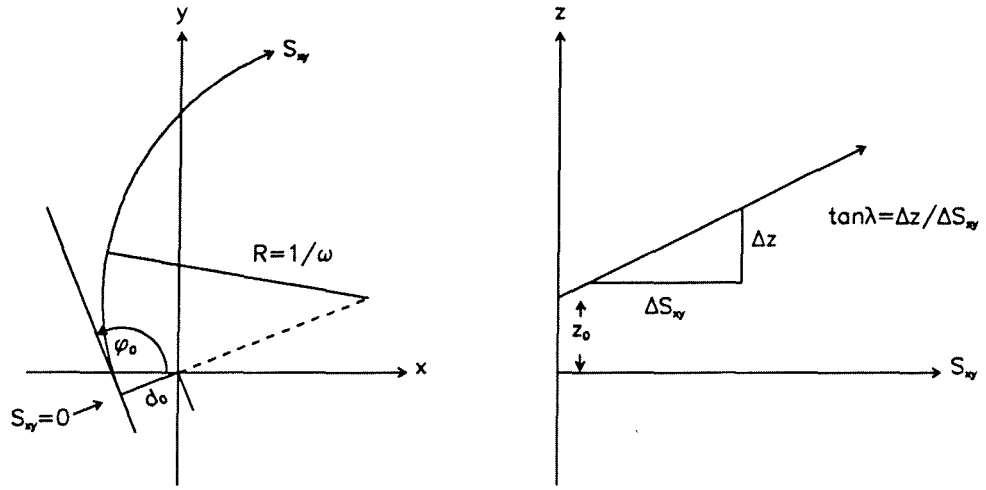

Figure 3.3: *Helix parameters used in TPC tracking.*

Parameter	Definition
R	Radius of curvature in (x,y).
d_0	Closest point of approach to the beam in (x,y).
z_0	z position at the point of closest approach.
ϕ_0	Initial angle of the track in the (x,y) plane.
tanλ	Angle of the track in the (s_{xy}, z) plane.

Table 3.2: *The fitted helix parameters and their definitions.*

around the magnetic field lines which thread the TPC, so producing many chains. The second reason is that occasionally a track is split into two pieces by the track fitting algorithm. JULIA takes into account the effect of multiple scattering at each stage. This effect increases coordinate error, and causes successive spirals to have smaller radii of curvature, due to the energy loss involved. Once the TPC track has been fitted it is extrapolated back into the ITC. If at least one hit in the outer two layers of the ITC is found within a road set up around this track then the extrapolation is continued. If there are three associated hits out of a maximum possible of eight then the whole track is refitted including these ITC hits.

3.4.3 Calorimeter Cluster Formation

In order that the energy deposit within the calorimeters can be reconstructed from the raw data, a set of corrections has to be made to the tower energy measurements. These corrections have to take into account the following:

- dead pads, wires, and storeys;
- overlap regions;
- cracks;
- leakage effects;
- saturation effects.

Also, threshold adjustments and refined calibrations have to be included. The algorithm which performs the clustering within JULIA operates in the following way. A storey is accepted into a cluster if it shares at least one corner with a cluster member and has an energy deposition greater than a threshold t_{low}. At this stage the ECAL and HCAL are treated separately. For a collection of storeys passing this criterion, at least one storey must exceed a second threshold t_{high} in order to form a cluster. For the ECAL it has been determined from both Monte Carlo and test beam studies that the thresholds should have the following values:

- $t_{low} = 30$ MeV;
- $t_{high} = 90$ MeV.

3.4.4 Track and Calorimeter Cluster Association

When the track and calorimeter cluster formation is complete the next step is to perform the association tests. First of all the ECAL clusters are associated to the TPC tracks. This is done by making a helical extrapolation into the three stacks of the ECAL. The road width surrounding the extrapolated track is one ECAL storey wide, which is

approximately 3 cm. A cluster is associated to the track if any of its constituent storeys lie within this road. This allows the possibility of many to many track to cluster relations. So as a final task these many to many relationships are converted into one to many ECAL object to track relationships, by grouping together all clusters which are associated to the same track. A similar method of track extrapolation is then used for the association test for HCAL clusters. The algorithm inside JULIA takes into account the energy loss, multiple scattering and the magnetic field inside the detector.

The association of HCAL objects to neutral isolated ECAL clusters or track associated ECAL objects is done on the basis of a 'relative transverse momentum' P_t with respect to the track. A TPC track which is associated to an ECAL cluster is extrapolated into the HCAL and the minimum separation between the track and an HCAL cluster is calculated. From knowledge of this distance and the HCAL cluster energy it is possible to determine the relative P_t of the HCAL object with respect to the track. The association is made with the track-ECAL object if the P_t is less than a certain threshold value. For the case of an isolated ECAL object, a straight line from the origin is extrapolated through the HCAL.

When all of the data are finally reconstructed they are stored on cartridges known as 'processed output tapes', or POT's. From these POT's smaller data sets are created by removing certain unnecessary or seldom used banks. These smaller data sets are known as 'data summary tapes', or DST's. Most physics analyses start from DST's, although if specialized information on a particular subdetector is required it may be necessary to go back to the POT's.

Chapter 4

Radiative Muon Pair Selection

4.1 Introduction

In an e^+e^- annihilation at LEP, a Z^0 boson is created which decays almost instantaneously into a pair of fermions. In approximately 3% of these decays, muon pairs are formed.

It can be said of all muon pair events, and indeed of all charged fermion pairs created in this way, that photons are always radiated in these interactions. But most of these photons carry away extremely low quantities of energy. Thus, these 'soft' photons do not appreciably affect the kinematics of the muon pair system, and indeed cannot even be registered by the detector. These final states are seen as a pair of collinear muons each possessing half of the centre of mass energy. But some events do contain high energy photons, which can be observed, if falling within the acceptance of the detector. An example of this kind of occurrence is shown in figure 4.1. This type of event provides a very clean signature compared to the hadronic decays of the Z^0. There are simply two highly penetrating, acollinear charged tracks, which deposit only a small amount of energy in the ECAL, and one or more isolated ECAL energy deposits. Also, most if not all of the available energy and momentum in these events is measured within the detector. This kind of event topology can be searched for by the use of very simple

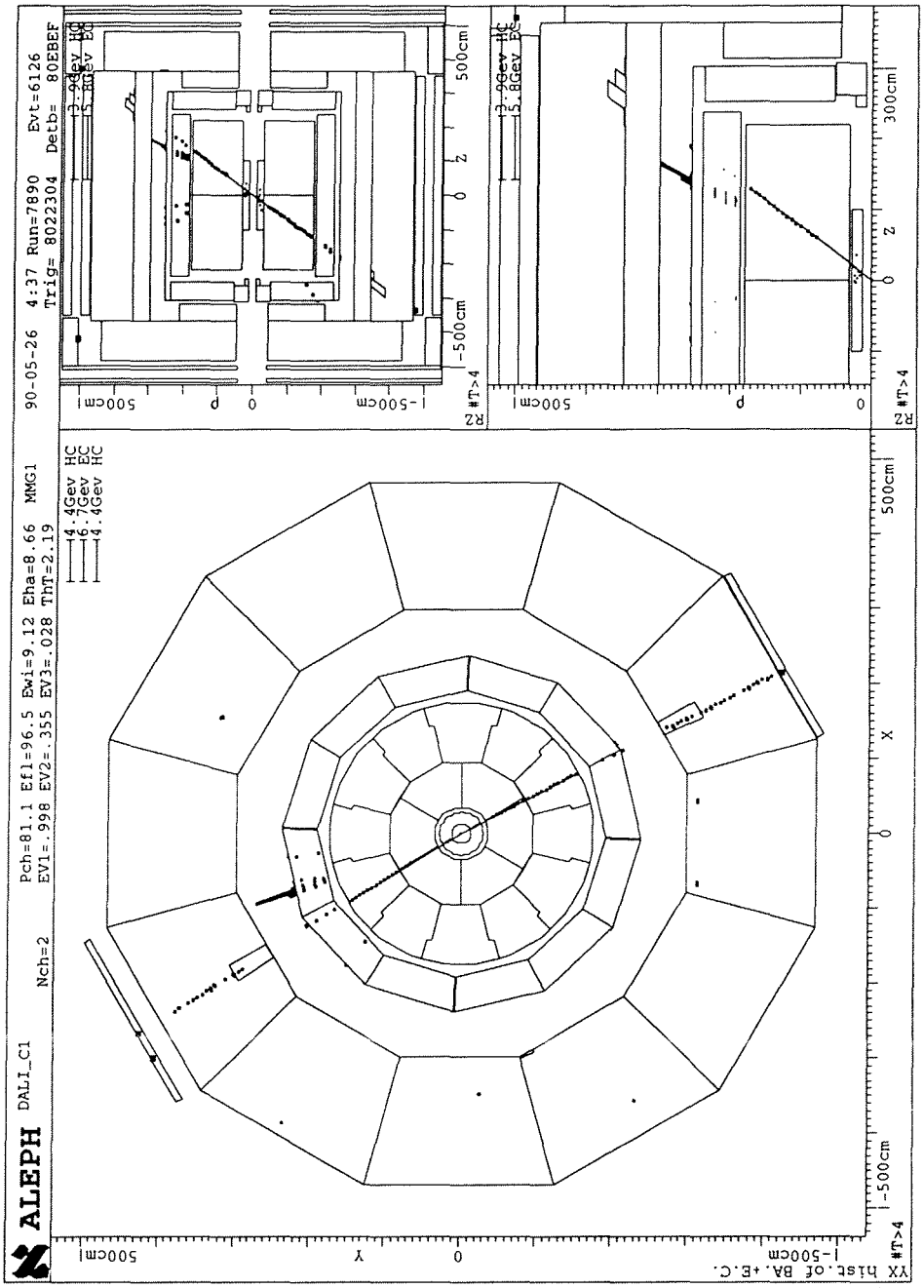

Figure 4.1: *An example of a radiative muon pair event.*

selection criteria.

There are several sources of background which can produce a similar set of signals within the detector to those of radiative muon pair events. It is necessary to remove as many of these events as possible from the data in order to obtain measurements of the cross-sections and asymmetries for the processes under study. Each of these backgrounds has its own characteristics on which rejection criteria can be based.

An example of such a background is radiative Bhabha pair production i.e. $e^+e^- \rightarrow e^+e^-N\gamma$. These events have a similar topology to that of the radiative muon pair events, but the electrons deposit all of their energy within the ECAL, in the form of electromagnetic showers.

A second source of background is from the process $e^+e^- \rightarrow \tau^+\tau^-(\gamma)$. In these events it is possible for the tau particles to decay into a charged particle such as an electron, muon, or pion ($\pi^{\pm}$). The charged pions are minimum ionizing particles, like the muons, depositing only a small amount of their energy within the ECAL. If any of these events also contain photons or neutral pions (π^0), which decay into a pair of photons, then the radiative muon pair event topology is again simulated. But in all tau decays neutrinos are created which cannot be detected, so there is missing energy and momentum in these events. All of the main tau decay modes of concern are listed in table 4.1 along with their branching fractions [1].

Another source of background is from two photon events, which are purely QED driven processes. These events are due to the interactions between photons emitted by an incoming beam electron and positron as they pass one another. The interaction can be represented by $e^+e^- \rightarrow e^+e^-\mathrm{X}$, where the final state X is of low momentum and can either be a pair of acollinear leptons or a multihadronic state or a single hadronic resonance. These processes are listed below.

- $e^+e^- \rightarrow e^+e^-\mu^+\mu^-(\gamma)$

[1]The τ^+ decay modes are the charge conjugates of the τ^- decay modes.

τ^- Decay Products	Branching Fraction $\frac{\Gamma_i}{\Gamma}$
$\mu^-\overline{\nu_\mu}\nu_\tau$	$(17.8 \pm 0.4)\%$
$e^-\overline{\nu_e}\nu_\tau$	$(17.7 \pm 0.4)\%$
$\pi^-\nu_\tau$	$(11.0 \pm 0.5)\%$
$\pi^-\pi^0\nu_\tau$	$(24.0 \pm 0.6)\%$
$\pi^-2\pi^0\nu_\tau$	$(7.5 \pm 0.9)\%$
$\pi^-3\pi^0\nu_\tau$	$(3.0 \pm 2.7)\%$

Table 4.1: *Table of Important Tau Branching Ratios.*

- $e^+e^- \rightarrow e^+e^-e^+e^-(\gamma)$
- $e^+e^- \rightarrow e^+e^-\tau^+\tau^-(\gamma)$
- $e^+e^- \rightarrow e^+e^-q\bar{q}(\gamma)$

In these interactions the created particles tend to pass undetected along the beam pipe. But sometimes they do enter the detector and two charged tracks can be observed, which may radiate photons. Sometimes the beam electron or positron, in these interactions, will be scattered at a large enough angle to enter the detector, often leaving little or no track within the TPC and depositing its energy within the ECAL. This combination of tracks and energy deposits again simulates the radiative muon final state, but these events possess missing energy and momentum.

A source of background which is not beam related is due to cosmic ray muons passing through the interaction region while the beam crossing gate is open. These particles can have energies of the order of several hundred GeV. They are produced high up in the atmosphere from the decay of pions and kaons. For example,

$$\pi^+ \rightarrow \mu^+\nu_\mu \tag{4.1}$$

These mesons are themselves the by-product of ultra high energy collisions between

atomic nuclei, such as nitrogen, and the primary cosmic rays, these being protons (87 %), and α-particles (12 %) [54,55,56]. Since the cosmic muons pass all the way through the detector, these events appear as two back to back tracks. Occasionally, the energetic, incoming cosmic muons will create large electromagnetic showers inside the ECAL, and the satellite clusters which are formed will simulate photons. Also it is possible for two or more cosmic muons to be passing through the detector at the same time. The tracks of these additional cosmic muons may not be reconstructed and selected, but their ECAL energy deposits will be measured. Again this kind of background would emulate a radiative muon pair event.

Backgrounds can arise from beam-gas collisions, and also from hadronic Z^0 decays in which most of the tracks are sprayed along the beam line. But in these events energy and momentum are missing.

In any of the aforementioned events, it is possible for electronic noise signals to be produced within the ECAL subdetector, which can be an unwelcome source of fake photons. Noise signals tend to occur in tightly packed groups of ECAL towers, and often appear in only one stack.

Finally, the $\mu^+\mu^-\gamma$ and $\mu^+\mu^- N\gamma$ final states can be easily confused. It is quite possible for two or more photons to be created above the detection threshold. If one of these photons passes undetected down a crack, or along the beam pipe, then this would give a similar signature to the single bremsstrahlung case. Also, it is possible for additional photons to be generated as the muons and photons from the Z^0 pass through the detector.

4.2 Event Simulation

In chapter 1 it was stated that the comparison of the electroweak model with the experimental observations is done with the aid of Monte Carlo event generators. This

section contains a brief description of the event generators which are used in this analysis.

4.2.1 KORALZ

KORALZ [35,57] is a Monte Carlo event generator which is capable of simulating the production of μ pairs in e^+e^- annihilation, at centre of mass energies in the region of the Z^0 resonance. This program takes into account both the photon and Z^0 exchange diagrams and includes the following higher order corrections:

- Multiple QED hard bremsstrahlung from the initial state $e^{\pm}$.
- Single photon bremsstrahlung only, from the final state $\mu^{\pm}$.
- $O(\alpha)$ radiative corrections from the standard electroweak model.

These corrections may be switched on and off. Also KORALZ can be run in single bremsstrahlung mode. There are two limitations of this generator which must be taken note of:

- Multiple final state radiation is not included.
- The QED initial-final state bremsstrahlung interference is not included when the generator is working in multiple bremsstrahlung mode.

KORALZ is also used to simulate the production and subsequent decay of tau pairs produced in Z^0 events. This generator simulates all decays of the tau lepton and includes spin polarization effects in the decay processes.

4.2.2 BABAMC

Bhabha events are simulated using a program called BABAMC [58]. This program takes into account both the photon and Z^0 annihilation diagrams, otherwise known as 's-channel' diagrams, and includes full $O(\alpha)$ electroweak radiative corrections. Also, this generator includes the QED scattering diagrams, known as 't-channel' diagrams.

One disadvantage of this program is that it can only generate at most one hard photon. Thus the absence of higher order photon corrections leads to an overestimate of about 30 % in the number of radiative bhabha events.

4.2.3 HVFL02

The simulation of the hadronic decays of the Z^0 is done using a program called HVFL02. HVFL02 is itself made up from two other programs. The first program, DYMU3 [35,59], simulates the decay of the Z^0 into a quark and an antiquark pair, and includes initial state radiation from the e^+ and e^- up to $O(\alpha^2)$, while the second, JETSET 7.3 [60], deals with the fragmentation process which converts the quarks into observable hadrons. In JETSET this is done in two stages: first the emission of gluons in a 'parton shower' described by a leading-log approximation to QCD, and secondly the production of hadrons from the quarks and gluons of the shower, which in JETSET is achieved using the string model. Final state photon radiation from the initial $q\bar{q}$ pair is also simulated in JETSET.

4.2.4 Two-Photon Simulation

The event generator used to simulate these events is based on a program by Vermaseren [61,62]. Lepton and quark pair production is simulated according to QED. The final hadronization stage for $q\bar{q}$ pairs is performed by using JETSET.

There is a second route for the production of hadrons in two-photon events. When the photons are emitted from the beam particles they are continually fluctuating into fermion antifermion pairs. If both photons are nearly 'real' they can fluctuate into a quark and an antiquark which form a bound state, namely one of the vector mesons, e.g. ρ^0. The vector mesons then interact to form other hadrons. Being a soft hadronic process, this interaction is not calculable in perturbative QCD, so to simulate it a phenomenological model, the Vector Dominance Model (VDM) [63], is used, and the

parameters of this model are tuned to fit the ALEPH data.

4.2.5 GALEPH

The above generators produce output in the form of four-vectors. To compare this with ALEPH measurements, it is necessary to convert it to a form equivalent to ALEPH data. This is done by the program GALEPH (Generator for ALEPH) [64], which is a mathematical description of the ALEPH detector. This program converts the four-vectors produced by the generators into the raw data output which would be produced by real particles passing through the ALEPH detector. The raw output is then fully reconstructed by JULIA in exactly the same way as the real data. This allows a proper comparison of the experimental observations with the theory.

4.3 Event Selection

In order to illustrate the effect of the event selection criteria, the following distributions are shown for the data collected in 1991 at the Z^0 peak at 91.2 GeV, unless otherwise stated. The forms of the distributions show no strong energy dependence. All Monte Carlo distributions are normalized to the same integrated luminosity as the real data, and the resultant Monte Carlo distributions include the contributions from all of the aforementioned Z^0 mediated processes as well as two photon events.

The following physics analysis was carried out using the entire data set collected by ALEPH during 1990 and 1991. In order to select the radiative muon pair events from the data set, the event selection procedure was split up into two parts:

- preselection;
- radiative muon pair selection.

The criteria used to select the events were decided upon only after extensive studies of both the real and Monte Carlo data distributions. The philosophy behind these

criteria was to suppress all possible backgrounds, without requiring the positive muon identification offered by the ALEPH HCAL and muon chambers. This was done as an alternative method to that used by the ALEPH muon group [65], and to obtain as many radiative muon pair events as possible without requiring the muon chambers to be fully operational.

Monte Carlo events were generated and fully reconstructed for each of the different backgrounds, as well as for the radiative muons. This was done at seven different centre of mass energies, corresponding to the seven points in the scan of the Z^0 resonance made by LEP, i.e. at the peak and also off peak at $\pm 1, \pm 2, \pm 3$ GeV. In order to minimize the statistical errors, more than five times the expected number of events at each $\sqrt{s}$ value were generated.

The two analysis steps will now be explained.

4.3.1 Preselection

The aim of this first step was simply to reduce the entire data set down to all events containing between 2 and 4 tracks. This was done so that the data could be stored on a few cartridges, which would allow faster processing during the second step of the analysis.

In order to select all 2, 3 and 4 track events, a set of criteria is needed to define a good track. The basic quantities used for this purpose are d_0 and z_0, which were defined in section 3.4.2, and the number of TPC hits associated to the track, N_{tpc}.

The d_0 and z_0 define a cylindrical volume around the nominal beam collision point, from which the tracks must emanate. A cut on these quantities can remove beam-gas events as well as some cosmic ray muons, and also badly reconstructed tracks. The standard set of loose cuts used at this stage are $|d_0| \leq 5cm$, and $|z_0| \leq 20cm$. Also the minimum number of TPC hits required to ensure that a track is well reconstructed is four.

Applying these criteria to the 1990 data yielded a total of 123,129 events and a further 223,829 events from the 1991 data set, which were then used for the following analysis.

4.3.2 Radiative Muon Pair Selection

The aim of this second stage was to obtain a pure sample of radiative muon pair events, by removing all of the possible background sources.

The experimental method presented here is based mainly upon the data obtained from the TPC and ECAL subdetectors. From the preselected data, all events containing only 2 good tracks were chosen. The criteria for good track selection were again based on the quantities used in the preselection step. But this time the criteria were tightened, i.e.

- $|d_0| \leq 2\text{cm}$
- $|z_0| \leq 8\text{cm}$
- $N_{tpc} \geq 5$

In addition to these requirements, the charge sum of the tracks must be zero, and also the polar angle of both tracks must satisfy $|\cos\theta| \leq 0.93$. The d_0 and z_0 real data distributions are shown in figures 4.2 and 4.3.

These track cuts remove nearly all of the multi-track beam-gas and hadronic Z^0 decay events as well as all of the multiprong tau decays. One further requirement is that the two tracks must be acollinear. The acollinearity angle η is defined by equation 4.2.

$$\eta \equiv \pi - \theta_{\mu^+\mu^-} \tag{4.2}$$

For the event to be selected, the tracks must satisfy the requirement:

- $\eta \geq 10\ mrad$

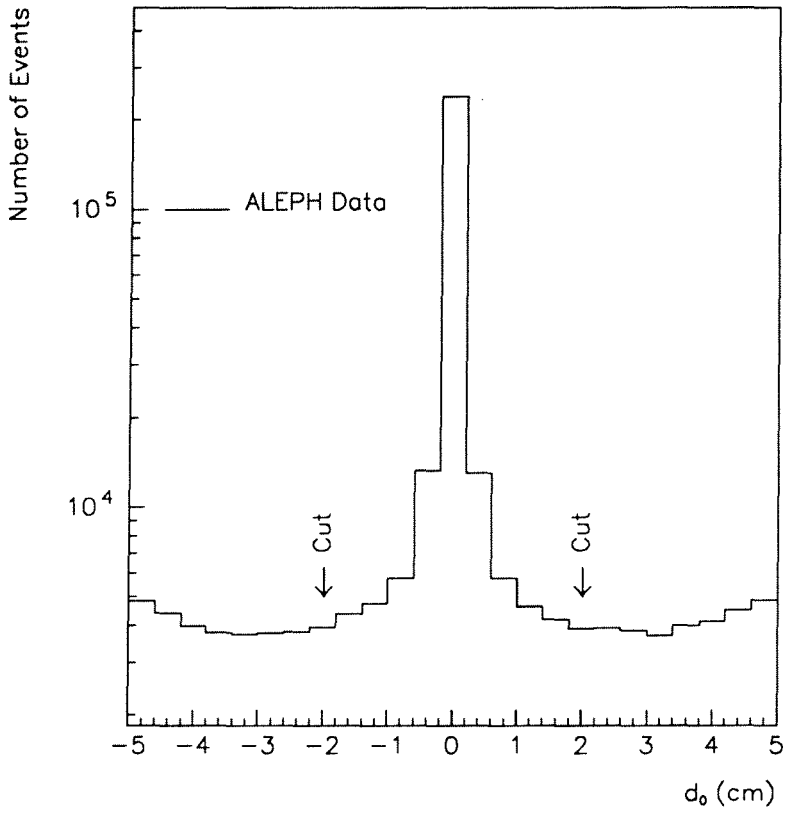

Figure 4.2: *The d_0 distribution for all 2, 3 and 4 track events in the real data at 91.2 GeV.*

This removes back to back tracks due to non-radiative lepton pairs and also cosmic ray muons. Another reason for the implementation of this cut will be given shortly.

From this set of 2 track events, the final sample of radiative muon pair events was obtained after the following steps:

- photon identification;
- tau background rejection;
- electron background rejection;
- cosmic ray rejection;
- event scanning.

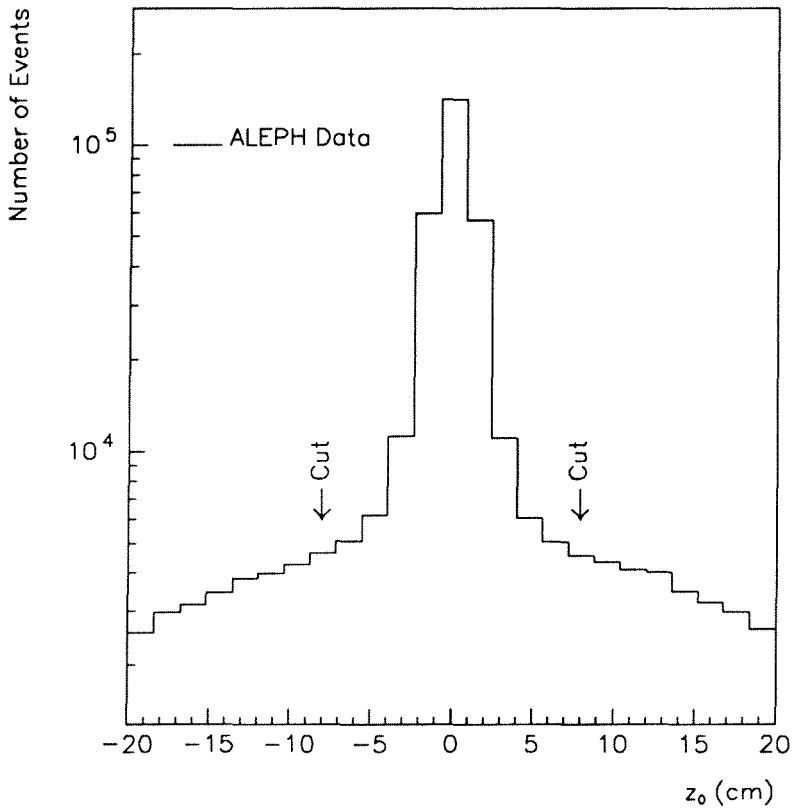

Figure 4.3: *The z_0 distribution for all 2, 3 and 4 track events in the real data at 91.2 GeV.*

These will now be explained in detail.

Photon Identification

First of all, a search was conducted within the ECAL for photon-like objects, and secondly, the events were classified according to the number of good clusters present. The following criteria were used in order to select good ECAL clusters.

- The ECAL cluster must not be associated to a track, though it is allowed to have an association with the HCAL.
- The cluster must occupy two or three stacks of the ECAL. This requirement removes some noise signals which often occur in one stack only.

- The cluster energy, $E_{cluster} \geq 2.0$ GeV.
- The polar angle of the cluster must satisfy $|\cos\theta_{cluster}| \leq 0.93$.
- The fractional energy deposit in the four highest energy towers of a cluster, F_4, must satisfy the requirement, $0.8 \leq F_4 \leq 0.98$. This is used to reject noise clusters and π^0s and is discussed in more detail below.
- The minimum angle between a cluster and a track $\theta_{min} \geq 140$ mrad. This ensures a clear separation between the two. This is discussed in more detail below.

The fractional energy deposit in the four highest energy towers of a cluster is one of the standard ALEPH estimators used in the analysis of ECAL clusters, and from Monte Carlo studies the range of this quantity stated here is suitable for photon identification [67]. The distribution of F_4 values for the real data is shown in figure 4.4. In figure 4.4 it can be seen that there are ECAL clusters possessing F_4 values of around 1.0, where all of the cluster's energy is found in just four towers. This is unphysical and can only be attributed to noise signals occurring on the pads in neighbouring towers. There is also a small spike around the value of zero due to tracks which deposit only a little energy within the calorimeter.

The largest number of ECAL towers fired by the clusters passing the previous cuts was found to be 30. Using this information as well as the largest angular width of the ECAL towers, which is 17 mrad for the barrel, the area of the largest cluster was estimated. By making the approximation that the clusters were circular in shape, and by using the equation for the area of a circle, the diameter of this cluster was estimated, and it was this number which was used for the minimum angular separation between a track and a cluster.

The number of good clusters selected by these cuts was then taken to be the number of photons present in the event. It must be remembered that the number of photons observed may not be the true number emitted in the event, due to acceptance

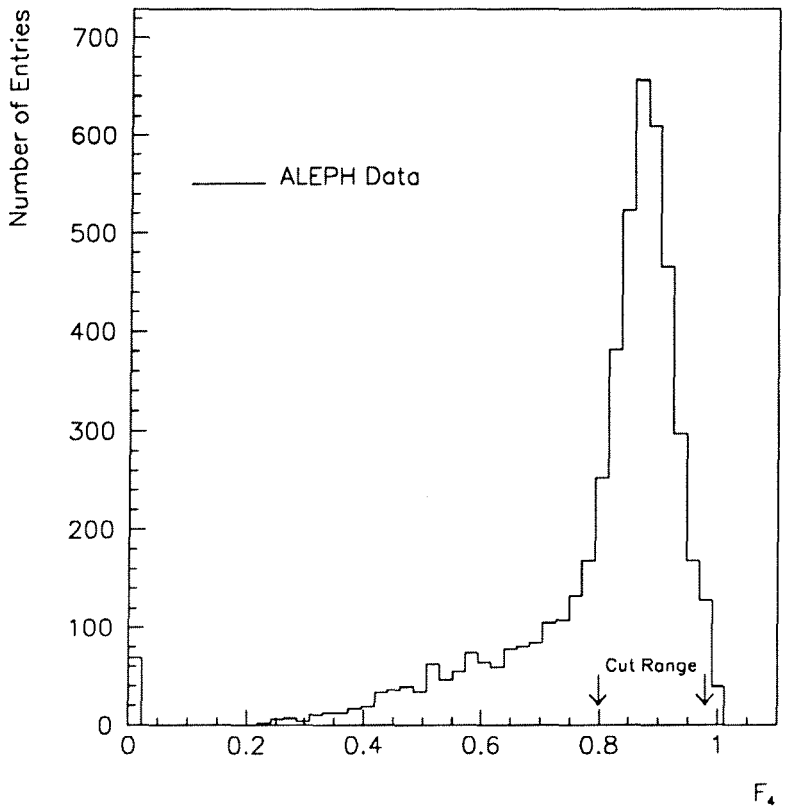

Figure 4.4: *The fractional energy deposit in the four highest energy towers of an ECAL cluster.*

and detection problems, but this can be corrected for later. With this in mind, all events containing only one cluster then undergo one further test, and this will now be explained.

In any three body decay, the trajectories of the outgoing particles are kinematically confined to lie in one plane. This is due to the conservation of energy and momentum. With the requirement that the two tracks are acollinear, it is possible to define a normal vector, $\underline{\hat{\mathbf{n}}}$. The definition of $\underline{\hat{\mathbf{n}}}$ is given by equation 4.3.

$$\underline{\hat{\mathbf{n}}} \equiv \frac{\mathbf{P_1} \times \mathbf{P_2}}{|\mathbf{P_1} \times \mathbf{P_2}|}, \tag{4.3}$$

where $\mathbf{P_1}$ and $\mathbf{P_2}$ are the momentum vectors of the positive and negative charged tracks respectively. This plane formed by $\underline{\hat{n}}$ is illustrated in figure 4.5a. The opening

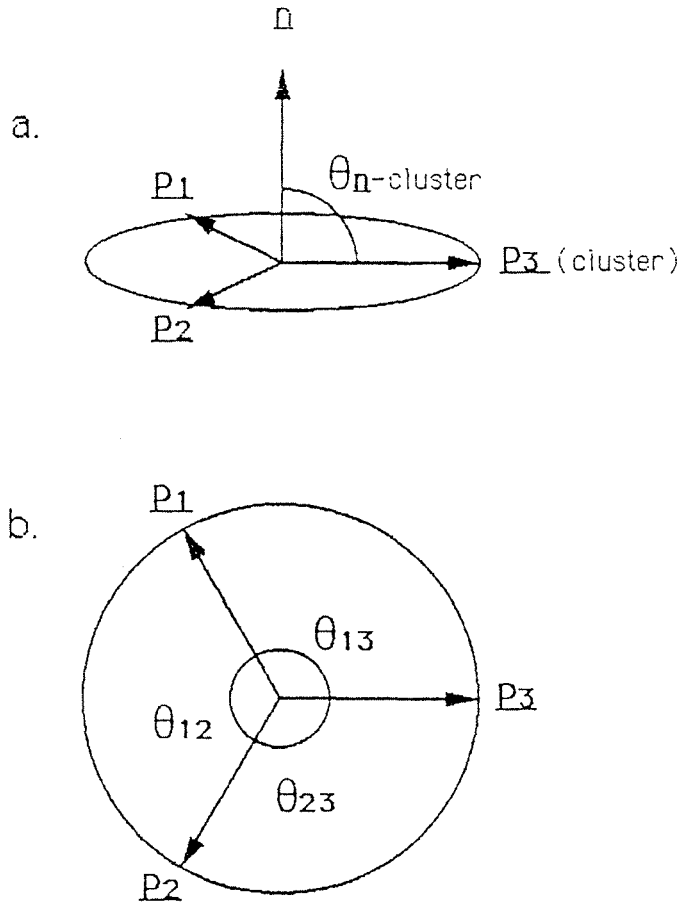

Figure 4.5: *(a) The definition of the event plane. (b) The opening angles between the momentum vectors within the event plane.*

angles between the momentum vectors of the particles within this plane are illustrated in figure 4.5b. So by searching for good clusters lying within the 'Event Plane', i.e. $\theta_{\underline{\hat{n}}-\text{cluster}} \approx 90^0$, it is possible to select events resembling a three body decay. The angular distribution of the ECAL clusters relative to the event plane is shown in figure 4.6. In this figure, the real data are represented by the dots, and the resultant Monte Carlo data are indicated by the histogram. Also shown is this plot are the signal and background contributions to the resultant Monte Carlo distribution. A cut was placed on this distribution at $|\cos\theta_{\underline{\hat{n}}-\text{cluster}}| \leq 0.15$. For the three body decay events

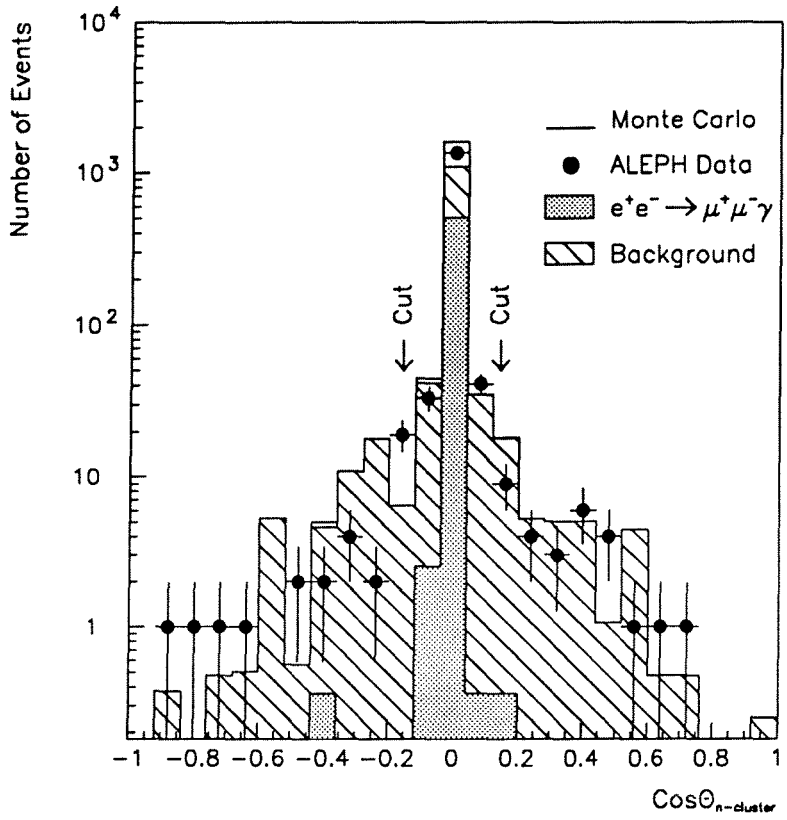

Figure 4.6: *The angular distribution of photon candidates relative to the event plane.*

which pass this test, it can be shown that the momentum of any particle is a function only of the opening angles between the particle vectors in the event plane, and the centre of mass energy. An expression for the photon's momentum, $\mathbf{P_3}$, is given by equation 4.4.

$$\mathbf{P_3} = \sqrt{s}\frac{\sin\theta_{12}}{\sin\theta_{12} + \sin\theta_{13} + \sin\theta_{23}} \tag{4.4}$$

Finally, the total photonic energy in the event, E_γ is defined by:

$$E_\gamma = \sum_{i=1}^{N} E_i, \tag{4.5}$$

where N is the number of good photon-like clusters found in the event.

The Total Energy Cut

Since most if not all of the available energy and momentum in a radiative muon pair event is measured, a cut on the total energy can be applied in order to reject background events in which this is not the case. The total energy, normalized to the centre of mass energy $\sqrt{s}$, is defined by equation 4.6.

$$E_{total} = \frac{P_{track1} + P_{track2} + E_{\gamma}}{\sqrt{s}}, \tag{4.6}$$

where P_{track1} and P_{track2} are the momenta of the charged tracks, measured using the TPC. The distribution of total energy values is shown in figure 4.7. This distribution

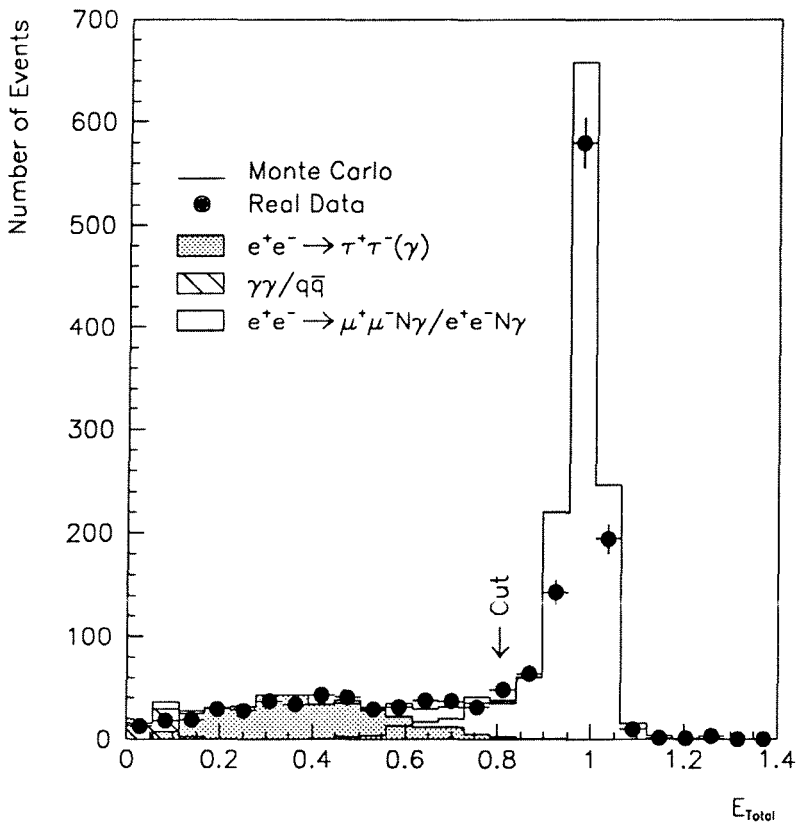

Figure 4.7: *The total energy distribution for events at 91.2 GeV.*

has a peak at a value of 1.0 which contains contributions from both radiative muon pair and radiative electron pair events. By applying a cut at $E_{total} \geq 0.8$, the muon

and electron event samples remain basically intact, while nearly all of the background from tau events, which are spread across a range of energies, is removed. Also all of the 2-photon and any remaining $q\bar{q}$ events are removed.

The E/P Cut

The next step was to remove the background from radiative electron pair events. This was done by applying a cut on the fractional energy deposit in the ECAL by the charged tracks. The fractional energy deposit, **E/P**, is defined by equation 4.7.

$$\mathbf{E/P} = \frac{E_{track1} + E_{track2}}{P_{track1} + P_{track2}}, \tag{4.7}$$

where E_{track1} and E_{track2} are the track ECAL deposits. The distribution of **E/P** values for the events remaining at this stage of the analysis, is shown in figures 4.8a and 4.8b.

These distributions show that the electron events cluster around a value of $\mathbf{E/P} \approx 1.0$, as the electrons deposit most of their energy in the ECAL, while the minimum ionizing muons peak around a value of $\mathbf{E/P} \approx 0.01$. By placing the cut at $\mathbf{E/P} \leq 0.1$, all of the electron events are removed, while the radiative muon sample remains intact.

It can be seen from figures 4.8a and 4.8b that the electron Monte Carlo distribution is about 30 % higher than the data distribution. This is due to the fact that the number of radiative bhabha events is overestimated as explained in section 4.2.2.

Cosmic Ray Rejection

At this stage a high purity sample of radiative muon pair events was obtained, with only a very small contamination from the Z^0 mediated backgrounds. Only one more background needs to be considered and this is cosmic ray muons. The requirement that the events contain acollinear tracks as well as isolated ECAL clusters will remove most if not all of the cosmic muons. But in addition to these, one final cut on the total

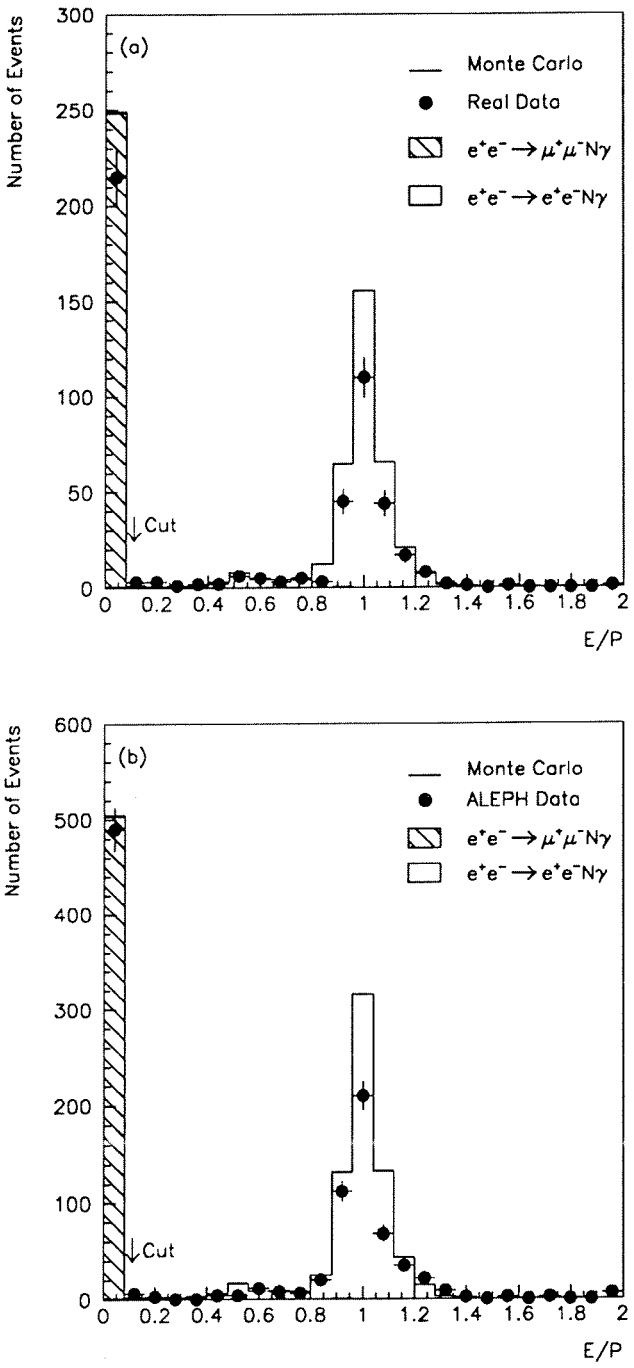

Figure 4.8: *a). The distribution of* **E/P** *values for all 2 track events selected from the 1990 data set at 91.2 GeV. b). The distribution of* **E/P** *values for all 2 track events selected from the 1991 data set at 91.2 GeV.*

momentum of the tracks is made, i.e.

$$P_1 + P_2 \leq \frac{3}{2}\sqrt{s} \tag{4.8}$$

This cut also removes events containing badly reconstructed tracks. It was found that only a few events were rejected by this cut.

Event Scanning

The last step in this analysis was to scan the final event sample, which contained 306 events from the 1990 data and 630 events from the 1991 data. Using an event display program called DALI [68], the fully reconstructed events were checked and all were found to be consistent with being radiative muon pair events.

4.4 Efficiencies and Corrections

The numbers of events selected at each centre of mass energy for the processes $e^+e^- \rightarrow \mu^+\mu^-\gamma$ and $e^+e^- \rightarrow \mu^+\mu^- N\gamma$ are given in tables 4.2, 4.3, 4.4 and 4.5. These tables also contain the predicted number of radiative muon events, N_{pred}, and also the estimated number of background events, which are due only to the taus and electrons. The backgrounds, N_{bg}, were estimated by counting the number of Monte Carlo events passing the selection criteria, and then weighting this number by the ratio of experimental to Monte Carlo luminosity as shown by equation 4.9.

$$N_{bg} = N_{accepted}\frac{\int \mathcal{L}_{exp}.dt}{\int \mathcal{L}_{mc}.dt} \tag{4.9}$$

A similar method was used to obtain the predicted number of radiative muon events.

The selected radiative muon pair events are only a fraction of the total number of these events being produced. This is due to the fact that events are lost because of some or all of the following reasons:

- reconstruction inefficiencies;

$\sqrt{s}$/GeV	$N_{\mu^+\mu^-\gamma}{}^{observed}$	$N_{\tau^+\tau^-}{}^{bg}$	$N_{e^+e^-}{}^{bg}$	$N_{\mu^+\mu^-\gamma}{}^{predicted}$
88.222	2.0	0.0	0.0	5.8
89.215	5.0	0.0	0.0	7.6
90.217	16.0	0.0	0.0	21.1
91.214	212.0	0.6	0.0	248.2
92.206	28.0	0.2	0.0	27.9
93.208	26.0	0.0	0.0	20.5
94.201	11.0	0.0	0.1	16.3

Table 4.2: *The number of* $e^+e^- \to \mu^+\mu^-\gamma$ *events selected from the 1990 data set.*

$\sqrt{s}$/GeV	$N_{\mu^+\mu^- N\gamma}{}^{observed}$	$N_{\tau^+\tau^-}{}^{bg}$	$N_{e^+e^-}{}^{bg}$	$N_{\mu^+\mu^- N\gamma}{}^{predicted}$
88.222	2.0	0.0	0.0	5.8
89.215	5.0	0.0	0.0	7.8
90.217	16.0	0.0	0.0	21.1
91.214	217.0	0.6	0.0	248.4
92.206	29.0	0.2	0.0	28.2
93.208	26.0	0.0	0.0	20.8
94.201	11.0	0.0	0.1	16.6

Table 4.3: *The number of* $e^+e^- \to \mu^+\mu^- N\gamma$ *events selected from the 1990 data set.*

$\sqrt{s}$/GeV	$N_{\mu^+\mu^-\gamma}{}^{observed}$	$N_{\tau^+\tau^-}{}^{bg}$	$N_{e^+e^-}{}^{bg}$	$N_{\mu^+\mu^-\gamma}{}^{predicted}$
88.464	3.0	0.0	0.0	8.0
89.456	25.0	0.1	0.0	15.1
90.212	20.0	0.0	0.0	29.4
91.215	484.0	1.2	0.0	496.7
91.952	34.0	0.2	0.0	31.7
92.952	24.0	0.0	0.0	22.6
93.701	28.0	0.0	0.1	19.4

Table 4.4: *The number of $e^+e^- \to \mu^+\mu^-\gamma$ events selected from the 1991 data set.*

$\sqrt{s}$/GeV	$N_{\mu^+\mu^-N\gamma}{}^{observed}$	$N_{\tau^+\tau^-}{}^{bg}$	$N_{e^+e^-}{}^{bg}$	$N_{\mu^+\mu^-N\gamma}{}^{predicted}$
88.464	3.0	0.0	0.0	8.0
89.456	25.0	0.1	0.0	15.3
90.212	20.0	0.0	0.0	29.5
91.215	494.0	1.2	0.0	497.1
91.952	36.0	0.2	0.0	32.0
92.952	24.0	0.0	0.0	22.9
93.701	28.0	0.0	0.1	19.8

Table 4.5: *The number of $e^+e^- \to \mu^+\mu^- N\gamma$ events selected from the 1991 data set.*

- detector inefficiencies;
- poor acceptance into the detector;
- trigger inefficiencies;
- photon conversions;
- event selection criteria.

In order to obtain cross-section and asymmetry values which can be compared with theory and also with the results of other experiments, the data need to be corrected for the above inefficiencies. Also, the data must be corrected for the background events which have passed the event selection criteria. These corrections will now be explained. In the following, the efficiencies for acceptance into the detector and for event selection are combined and collectively called the 'event selection efficiency'.

4.4.1 Event Selection Efficiency

In order to determine the selection efficiencies, a set of radiative muon pair Monte Carlo events were generated and passed through the reconstruction chain and finally the analysis program. The number of events passing the criteria were then used for the efficiency calculation. The efficiency for $e^+e^- \rightarrow \mu^+\mu^-\gamma$ was defined in the following way:

$$\epsilon_{\mu^+\mu^-\gamma} = \frac{N^{\mu^+\mu^-\gamma}_{selected}}{N^{\mu^+\mu^-\gamma}_{true}}, \tag{4.10}$$

where $N^{\mu^+\mu^-\gamma}_{selected}$ is the number of selected events, and $N^{\mu^+\mu^-\gamma}_{true}$ is the true number of $e^+e^- \rightarrow \mu^+\mu^-\gamma$ events contained within the radiative muon pair Monte Carlo sample. A similar expression was used for the $e^+e^- \rightarrow \mu^+\mu^- N\gamma$ case.

$$\epsilon_{\mu^+\mu^- N\gamma} = \frac{N^{\mu^+\mu^- N\gamma}_{selected}}{N^{\mu^+\mu^- N\gamma}_{true}} \tag{4.11}$$

$\sqrt{s}$/GeV	$\epsilon_{\mu^+\mu^-\gamma}$	$\epsilon_{\mu^+\mu^-N\gamma}$
88.222	0.299 ± 0.017	0.278 ± 0.016
89.215	0.288 ± 0.011	0.274 ± 0.011
90.217	0.293 ± 0.009	0.283 ± 0.009
91.214	0.298 ± 0.007	0.291 ± 0.007
92.206	0.263 ± 0.008	0.254 ± 0.008
93.208	0.232 ± 0.007	0.216 ± 0.007
94.201	0.188 ± 0.006	0.171 ± 0.005

Table 4.6: *The selection efficiencies for the processes* $e^+e^- \rightarrow \mu^+\mu^-\gamma$ *and* $e^+e^- \rightarrow \mu^+\mu^- N\gamma$ *for the 1990 data set.*

The efficiencies take into account both the acceptance into the detector and the possible misidentification of the number of photons within the event. Also the events lost due to photon conversions into e^+e^- pairs are taken into account. The conversion rates for photons within the ALEPH detector have been measured and found to be 6.82 % ± 0.21 % in 1990 and 8.16 % ± 0.14 % in 1991 [69]. The rate for 1991 was 1.34 % higher with respect to 1990 due to the fact that the vertex detector was fully in position around the beam pipe so the additional material increased the probability for photon conversions. At the time of this analysis a sufficient sample of Monte Carlo events was available only for the 1990 detector configuration. In order to take into account the reduction in the number of identified photon events, due to the increased conversion rate, the 1991 selection efficiencies were obtained by reducing the 1990 efficiencies by 1.34 %. The values of the efficiencies at each centre of mass energy are presented in tables 4.6 and 4.7, along with their statistical errors. The values quoted in this table are used in the calculation of the total cross-section. As well as this, efficiency corrections must be applied to the muon polar angle distributions, from which the

$\sqrt{s}$/GeV	$\epsilon_{\mu^+\mu^-\gamma}$	$\epsilon_{\mu^+\mu^- N\gamma}$
88.464	0.295 ± 0.017	0.274 ± 0.016
89.456	0.284 ± 0.011	0.270 ± 0.011
90.212	0.289 ± 0.009	0.279 ± 0.009
91.215	0.294 ± 0.007	0.287 ± 0.007
91.952	0.260 ± 0.008	0.251 ± 0.008
92.952	0.229 ± 0.007	0.213 ± 0.007
93.701	0.186 ± 0.006	0.169 ± 0.005

Table 4.7: *The selection efficiencies for the processes* $e^+e^- \to \mu^+\mu^-\gamma$ *and* $e^+e^- \to \mu^+\mu^- N\gamma$ *for the 1991 data set.*

forward-backward asymmetries are obtained. The number of entries in each bin of these distributions is divided by the selection efficiency for that bin. This is necessary since it is possible that the efficiency changes in different parts of the ALEPH detector due to dead areas and subdetector problems. The variation of $\epsilon_{\mu^+\mu^-\gamma}$ with the polar angle of the μ^-, for data at 91.2 GeV, is given in figure 4.9 by way of example. The errors given for the selection efficiencies in tables 4.6 and 4.7 and in figure 4.9 are statistical, and were calculated by assuming a binomial distribution. For a given efficiency, the statistical error is given by:

$$\delta\epsilon = \sqrt{\frac{\epsilon(1-\epsilon)}{N_{mc}}}, \tag{4.12}$$

where N_{mc} here is the total number of events used to estimate the efficiency.

4.4.2 Trigger Efficiencies

In this analysis, two totally independent triggers were used. These were the Single Muon Trigger, and the Single Neutral Electromagnetic Energy Trigger. The Single Muon Trigger requires coincidence between track signals in the ITC and in the HCAL,

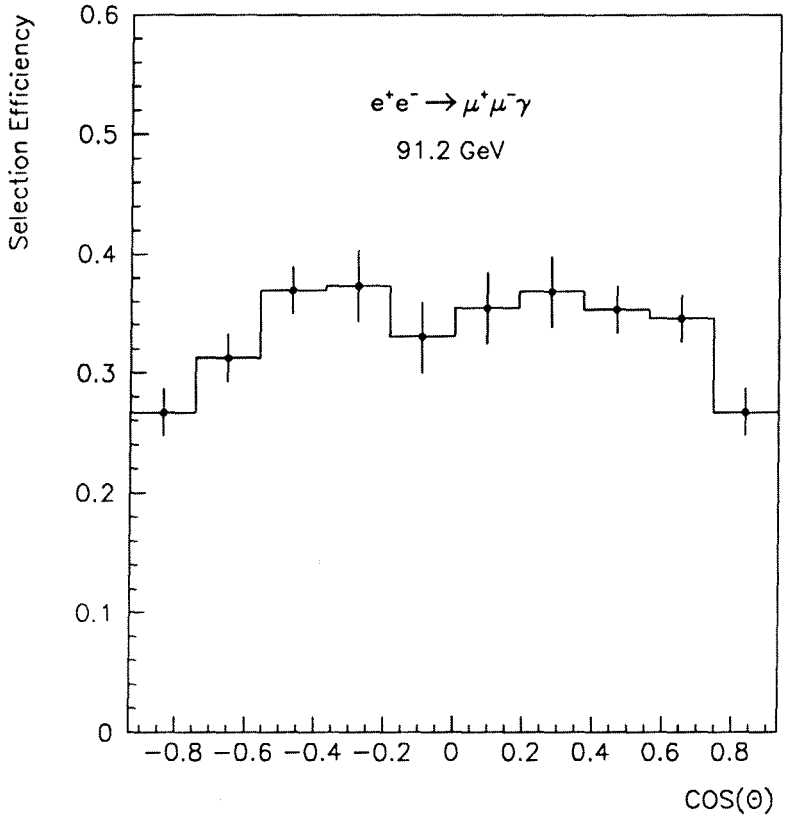

Figure 4.9: *The polar angle dependence of the selection efficiency for the process* $e^+e^- \rightarrow \mu^+\mu^-\gamma$ *at 91.2 GeV.*

while the Single Neutral Electromagnetic Energy Trigger requires the energy deposit on the odd and even ECAL wire planes both to be above a certain threshold [44]. The triggering efficiencies were calculated for the real data by counting how often these triggers fired in the selected event sample. The relations used to calculate these efficiencies will now be derived.

For the selected events, the number of times the single muon trigger is fired is given by:

$$N_\mu = \epsilon_\mu N. \tag{4.13}$$

Here ϵ_μ is the single muon trigger efficiency, and N is the number of events which would be selected if there where no trigger inefficiencies. The number of times the

ϵ_γ	ϵ_μ	N_μ	N_γ	N_{both}	Year
1.000	0.997	305	306	305	1990
1.000	0.998	629	630	629	1991

Table 4.8: *The trigger efficiencies for radiative muon pair events.*

single neutral trigger fired is given by the following equation:

$$N_\gamma = \epsilon_\gamma N, \tag{4.14}$$

where ϵ_γ is the efficiency of the single neutral trigger. The number of times both of these triggers fire is given by:

$$N_{both} = \epsilon_\mu \epsilon_\gamma N \tag{4.15}$$

So by manipulating equations 4.13, 4.14, and 4.15 the following expressions are obtained.

$$N = \frac{N_\mu N_\gamma}{N_{both}} \tag{4.16}$$

and

$$\epsilon_\mu = \frac{N_{both}}{N_\gamma} \tag{4.17}$$

and

$$\epsilon_\gamma = \frac{N_{both}}{N_\mu} \tag{4.18}$$

Using these equations the efficiencies for the triggers were calculated and these are presented in table 4.8 along with the number of times each of the triggers fired. From table 4.8 it can be seen that the combined trigger efficiency for radiative muon pair events is essentially 100 %.

Chapter 5

Results

5.1 Introduction

This analysis was conducted using the data obtained by ALEPH during 1990 and 1991. After the deletion of data not considered suitable for physics analysis, the total integrated luminosities were calculated to be 7.067 pb^{-1} for 1990 and 11.965 pb^{-1} for 1991 . These integrated luminosities were distributed across the scan of the Z^0 resonance, as indicated in tables 5.1 and 5.2. The centre of mass energies given in

$\sqrt{s}$ (GeV)	88.222	89.215	90.217	91.214	92.206	93.208	94.201
$\int \mathcal{L}.dt$ (pb^{-1})	0.482	0.412	0.537	3.775	0.608	0.611	0.642

Table 5.1: *The total integrated luminosities for the 1990 data taking period.*

$\sqrt{s}$ (GeV)	88.464	89.456	90.212	91.215	91.952	92.952	93.701
$\int \mathcal{L}.dt$ (pb^{-1})	0.668	0.797	0.753	7.609	0.693	0.677	0.768

Table 5.2: *The total integrated luminosities for the 1991 data taking period.*

tables 5.1 and 5.2 are the luminosity weighted mean values for the seven scan points.

In the following sections the results of the measurements of the cross-sections for

the processes $e^+e^- \rightarrow \mu^+\mu^-\gamma$ and $e^+e^- \rightarrow \mu^+\mu^- N\gamma$ will be presented along with the forward-backward charge asymmetries for the process $e^+e^- \rightarrow \mu^+\mu^-\gamma$. Also, a set of kinematical distributions will be given and compared with the standard model predictions. Included in these distributions are $\mu\gamma$ invariant mass plots which are used in a search for the occurrence of $\mu^\star$ production.

5.2 Cross Section Measurements

The total cross-sections for the processes $e^+e^- \rightarrow \mu^+\mu^-\gamma$ and $e^+e^- \rightarrow \mu^+\mu^- N\gamma$ are calculated using equations 5.1 and 5.2.

$$\sigma_{\mu^+\mu^-\gamma} = \frac{N_{\mu^+\mu^-\gamma} - N_{bg}}{\epsilon_{\mu^+\mu^-\gamma}\epsilon_{trig}\int \mathcal{L}.dt} \tag{5.1}$$

$$\sigma_{\mu^+\mu^- N\gamma} = \frac{N_{\mu^+\mu^- N\gamma} - N_{bg}}{\epsilon_{\mu^+\mu^- N\gamma}\epsilon_{trig}\int \mathcal{L}.dt} \tag{5.2}$$

where $N_{\mu^+\mu^-\gamma}$ and $N_{\mu^+\mu^- N\gamma}$ are the numbers of selected events and N_{bg} is the estimated total number of background events. Also contained within these equations are the combined acceptance and selection efficiencies for these final states $\epsilon_{\mu^+\mu^-\gamma}$ and $\epsilon_{\mu^+\mu^- N\gamma}$, the trigger efficiency ϵ_{trig}, and the integrated luminosity $\int \mathcal{L}.dt$. By inserting the data from tables 4.2, 4.3, 4.4, 4.5, 4.6, 4.7, 4.8, 5.1, and 5.2 into equations 5.1, and 5.2, the total cross-sections were calculated at each of the seven points of the scan of the Z^0 resonance. The results are presented in tables 5.4 and 5.5 and the predicted Monte Carlo cross-sections, which were calculated using equation 1.45, are given in table 5.3. Also the measured cross-sections are displayed in figures 5.1 and 5.2 along with the standard model predictions from KORALZ. The statistical errors quoted in tables 5.4, and 5.5 are due to the number of observed events, since all other contributions are negligible in comparison. The systematic errors arise from several sources:

- the luminosity measurement;
- event selection;

$\sqrt{s}$ (GeV)	$\sigma_{\mu^+\mu^-\gamma}$ (pb)	$\sigma_{\mu^+\mu^-N\gamma}$ (pb)
88.2	41 ± 2	44 ± 2
89.2	66 ± 2	70 ± 2
90.2	137 ± 3	140 ± 3
91.2	224 ± 3	228 ± 3
92.2	177 ± 4	184 ± 4
93.2	146 ± 3	158 ± 3
94.2	136 ± 2	153 ± 2

Table 5.3: *The predicted radiative muon pair cross-sections from KORALZ. The quoted errors are statistical and were obtained from the Monte Carlo.*

$\sqrt{s}$ (GeV)	$\int \mathcal{L}_{\rm exp}.dt$ (pb^{-1})	$\sigma_{\mu^+\mu^-\gamma}$ (pb)	$\sigma_{\mu^+\mu^-N\gamma}$ (pb)
88.222	0.482	14 ± 10 ± 1	15 ± 11 ± 2
89.215	0.412	42 ± 19 ± 4	44 ± 20 ± 5
90.217	0.537	102 ± 26 ± 9	105 ± 26 ± 11
91.214	3.775	188 ± 14 ± 17	197 ± 14 ± 21
92.206	0.608	174 ± 33 ± 16	187 ± 35 ± 20
93.208	0.611	184 ± 36 ± 17	197 ± 39 ± 21
94.201	0.642	90 ± 27 ± 8	99 ± 30 ± 11

Table 5.4: *The measured radiative muon pair cross-sections for the 1990 data set. The quoted errors are statistical and systematic respectively.*

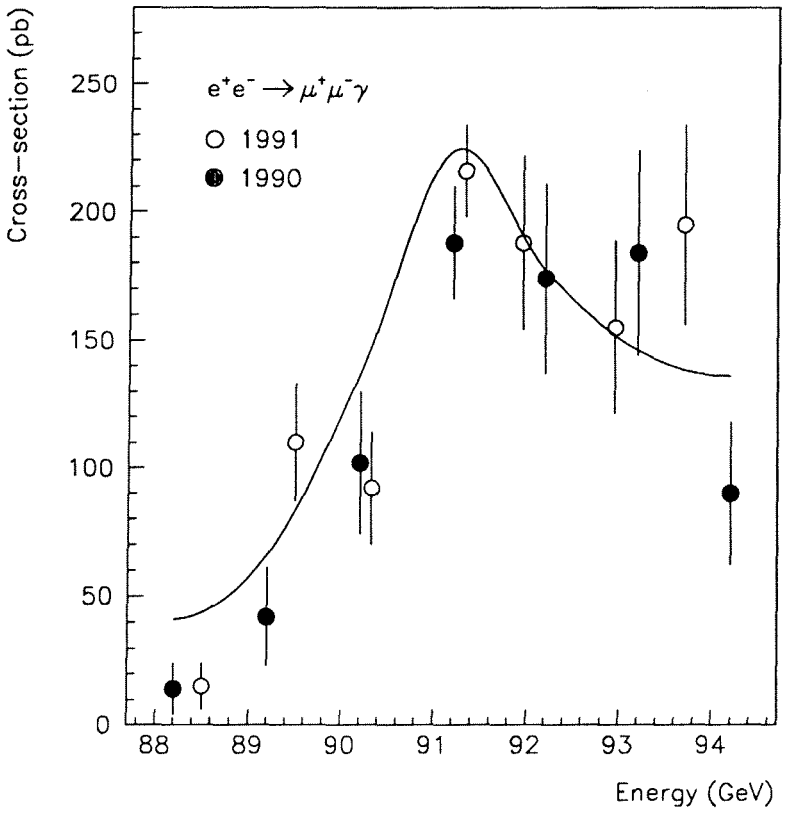

Figure 5.1: *The total cross-section for* $e^+e^- \rightarrow \mu^+\mu^-\gamma$. *The Monte Carlo cross-sections were calculated for the same 7 points in the scan of the* Z^0 *resonance as the real data and the predictions are shown here as a smooth curve drawn through these values. The dots with error bars are the measured values for 1990 and 1991. The error bars were obtained by adding in quadrature the statistical and systematic errors. The Monte Carlo statistical errors are very small and are not shown here. In order to show the full size of the errors the 1991 data points at 90.212 GeV and 91.215 GeV have been shifted to 90.325 GeV and 91.325 GeV respectively.*

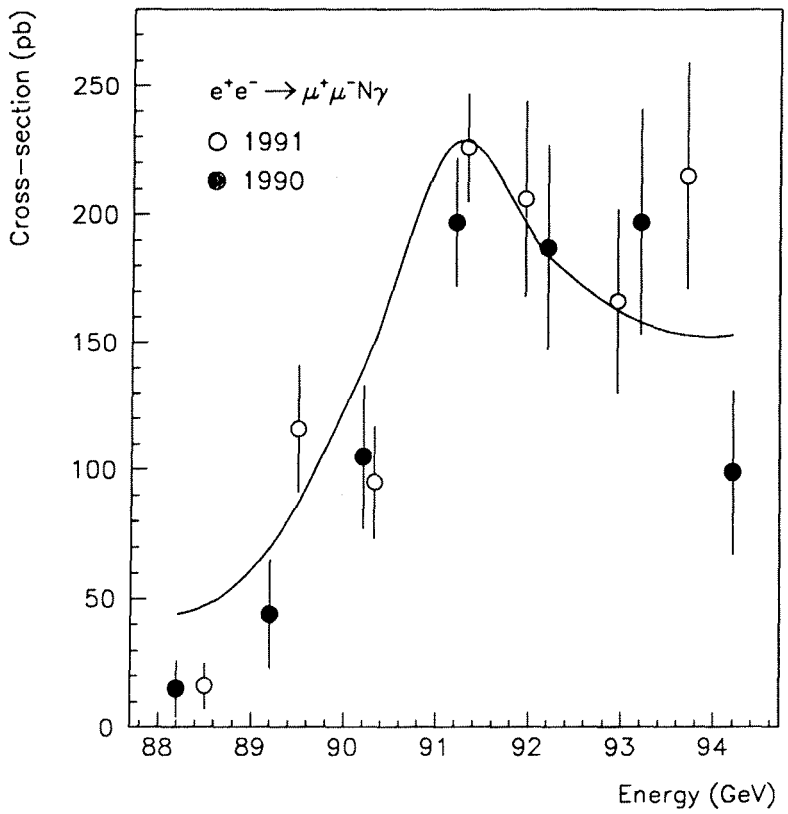

Figure 5.2: *The total cross-section for $e^+e^- \rightarrow \mu^+\mu^- N\gamma$. The Monte Carlo cross-sections were calculated for the same 7 points in the scan of the Z^0 resonance as the real data and the predictions are shown here as a smooth curve drawn through these values. The dots with error bars are the measured values for 1990 and 1991. The error bars were obtained by adding in quadrature the statistical and systematic errors. The Monte Carlo statistical errors are very small and are not shown here. In order to show the full size of the errors the 1991 data points at 90.212 GeV and 91.215 GeV have been shifted to 90.325 GeV and 91.325 GeV respectively.*

$\sqrt{s}$ (GeV)	$\int \mathcal{L}_{exp}.dt$ (pb^{-1})	$\sigma_{\mu^+\mu^-\gamma}$ (pb)	$\sigma_{\mu^+\mu^-N\gamma}$ (pb)
88.464	0.668	$15 \pm 9 \pm 1$	$16 \pm 9 \pm 1$
89.456	0.797	$110 \pm 22 \pm 7$	$116 \pm 23 \pm 9$
90.212	0.753	$92 \pm 21 \pm 6$	$95 \pm 21 \pm 7$
91.215	7.609	$216 \pm 11 \pm 14$	$226 \pm 12 \pm 17$
91.952	0.693	$188 \pm 32 \pm 12$	$206 \pm 34 \pm 16$
92.952	0.677	$155 \pm 32 \pm 10$	$166 \pm 34 \pm 13$
93.701	0.768	$195 \pm 37 \pm 13$	$215 \pm 41 \pm 16$

Table 5.5: *The measured radiative muon pair cross-sections for the 1991 data set. The quoted errors are statistical and systematic respectively.*

- trigger efficiencies;
- the background subtraction procedure.

The luminosity systematic error determination has been done elsewhere [70,71,66] and the results of this are summarised in table 5.6. The systematic errors from the event

Year	Experimental Error/ %	Theoretical Error/ %	Total Error/ %
1990	0.6	0.3	0.67
1991	0.45	0.3	0.54

Table 5.6: *The luminosity systematic errors. The total errors were determined by adding together in quadrature the experimental and theoretical contributions.*

selection were determined by varying the selection criteria one at a time, and the changes in the cross-sections which resulted were used as a measure of this error. The total contributions from this source are given in table 5.7. The error on the trigger efficiency was estimated to be negligible in comparison to the other errors. Finally, the systematic error on the background subtraction procedure was estimated from

Year	Error for $e^+e^- \rightarrow \mu^+\mu^-\gamma$/ %	Error for $e^+e^- \rightarrow \mu^+\mu^- N\gamma$/ %
1990	9.04	10.66
1991	6.48	7.52

Table 5.7: *The event selection systematic errors expressed as percentages.*

Monte Carlo and found to be negligible in comparison to the other sources. These contributions were then all added together in quadrature. The error bars displayed on the cross-section plots include both the statistical and the systematic errors added together in quadrature.

It was found that the 1990 cross-section measurements were mainly lower than the predicted values. As the statistics off peak were low and the 1990 peak cross-section was not in perfect agreement with the prediction the following systematic checks were performed on the data at the peak in order to test both the integrity of the data and the analysis technique. First of all the minimum photon energy cut was varied. This was done for several values over the range 0.5 GeV to 3 GeV. Although the cross-sections changed the deviations remained roughly the same. Next the radiative muon Monte Carlo sample, which was generated for this piece of analysis, was replaced by a standard ALEPH Monte Carlo sample which contained both radiative and non-radiative muon pair events. The predictions for the number of events and the cross-sections were in very good agreement with those used in this work. As a test, the same analysis code was applied to the identification of all $e^+e^- \rightarrow \mu^+\mu^- (\gamma)$ events. To do this the acollinearity cut was changed to $\eta \leq 0.4$ radians, and the number of photons in the event was allowed to be greater than or equal to zero. Results obtained with these cuts can be compared directly with the published work of the ALEPH muon group [65]. Using these criteria, a sample of 4516 muon events were selected with an estimated background of 20 events. This number of muon events was comparable with the published number. Also the

measured total muon cross-section for this data sample was found to be in very good agreement with the published value of $\sigma = 1.426\text{nb} \pm 0.022\text{nb}$. This measured cross-section is approximately 3 sigma lower than the prediction from KORALZ, which is 1.491 nb. This is thought to be a statistical fluctuation, since the measured value for the 1991 data set is in better agreement with the prediction [66]. These systematic checks confirm the accuracy of the analysis and indicate that the lower cross-sections may be due to a statistical fluctuation. When the 1991 results are included the cross-section measurements are found to be in acceptable agreement with KORALZ. One point which should be kept in mind is the fact that KORALZ does not include multiple final state bremsstrahlung, so the predicted cross-sections are slightly overestimated.

5.3 Asymmetry Measurements

Due to the fact that there are only a small number of identified radiative muon events, which are distributed across the scan of the resonance, it was decided that the forward-backward charge asymmetry, A_{fb}, should be measured for the data at the peak, and for the combined data at the three points below, and the three points above the peak. To obtain these asymmetries two methods were employed. The first method used here was to count the number of forward going muons, N_f, and the number of backward going muons, N_b. Here we use the angle between the incoming e^- and the outgoing μ^-, to define the forward and backward regions, i.e $N_f = N\left(\theta_{e^-\mu^-} < \frac{\pi}{2}\right)$, and $N_b = N\left(\theta_{e^-\mu^-} > \frac{\pi}{2}\right)$. By rewriting equation 1.51, given in chapter 1, in terms of N_f and N_b, the asymmetry for our acceptance into the ALEPH detector is given by:

$$A_{fb} = \frac{N_f - N_b}{N_f + N_b} \tag{5.3}$$

This must be corrected for the limited acceptance by using equation 5.4.

$$A_{fb}{}'\left(|cos\theta| \leq 1.0\right) = \frac{1}{k} A_{fb}\left(|cos\theta| \leq x\right) \tag{5.4}$$

where

$$\frac{1}{k} = \frac{3+x^2}{4x} \tag{5.5}$$

and x is the acceptance cut of 0.93. We call this method 1.

The second method used here, which is based on the differential cross-section expression 1.52, given in chapter 1, was to perform a χ^2-fit of the muon polar angle distribution to the function:

$$f(cos\theta) = 1 + \cos^2\theta + \frac{8}{3}A_{fb}\cos\theta \tag{5.6}$$

We call this Method 2.

Method 1 was used for the data at all energies while method 2 was only used for the data at the peak.

In order to make the asymmetry measurements using method 1, N_f and N_b had to be corrected for background and for selection efficiency. This was done in the following way. For the data at each centre of mass energy the $cos\theta_{e^-\mu^-}$ angular distribution was plotted on a 10 bin histogram. The number of entries in each bin were then background subtracted and then divided by the selection efficiency for that bin. It must be noted here that since the estimated background was low the subtraction made very little difference. The corrected values of N_f and N_b are given in tables 5.8 and 5.9 along with the uncorrected values obtained at each centre of mass energy.

The asymmetries were obtained by applying equations 5.3, 5.4, and 5.5 to the corrected data given in tables 5.8 and 5.9. These asymmetries are presented in tables 5.10 and 5.11 and are expressed as percentages. Tables 5.10 and 5.11 include the associated errors and the Monte Carlo predictions for the combined data below the peak, at the peak, and above it. The first errors are statistical, and due to the binomial nature of the measurements were determined using equation 5.7 which was taken from [72].

$$\delta A_{stat} = \sqrt{\frac{1 - {A_{fb}}^2}{k^2 N}} \tag{5.7}$$

$\sqrt{s}$/GeV	Uncorrected Data		Corrected Data	
	N_f	N_b	N_f	N_b
88.2	1.0	1.0	2.4	3.0
89.2	4.0	1.0	13.5	2.8
90.2	12.0	4.0	35.0	12.3
91.2	90.0	122.0	265.4	374.4
92.2	18.0	10.0	61.1	37.3
93.2	11.0	15.0	43.0	67.0
94.2	9.0	2.0	42.2	9.0

Table 5.8: *The numbers of forward and backward events from the 1990 data which are used in method 1. This table also includes the number of forward and backward events corrected for background and selection efficiency.*

$\sqrt{s}$/GeV	Uncorrected Data		Corrected Data	
	N_f	N_b	N_f	N_b
88.5	1.0	2.0	4.1	5.2
89.5	9.0	16.0	27.0	57.2
90.2	9.0	11.0	27.0	37.5
91.2	213.0	271.0	645.0	839.8
91.9	15.0	19.0	46.7	68.6
92.9	16.0	8.0	59.0	32.4
93.7	16.0	12.0	77.8	54.5

Table 5.9: *The numbers of forward and backward events from the 1991 data which are used in method 1. This table also includes the number of forward and backward events corrected for background and selection efficiency.*

$\sqrt{s}$/GeV	A_{fb}^{exp}/%	A_{fb}^{pred}/%
88.222, 89.2215, 90.217	-18 % ± 21 % ± 9 %	-19 % ± 8 %
91.214	-18 % ± 7 % ± 3 %	-1 % ± 3 %
92.206, 93.208, 94.201	+13 % ± 13 % ± 15 %	+3 % ± 6 %

Table 5.10: *The asymmetry measurements obtained from method 1 using the 1990 data. The errors are statistical and systematic respectively. This table also contains the predicted asymmetries obtained from a fit to MC truth level angular distributions and the statistical errors from the fit.*

$\sqrt{s}$/GeV	A_{fb}^{exp}/%	A_{fb}^{pred}/%
88.464, 89.456, 90.212	-27 % ± 14 % ± 11 %	-19 % ± 7 %
91.215	-14 % ± 5 % ± 1 %	-1 % ± 2 %
91.952, 92.952, 93.701	+9 % ± 11 % ± 7 %	+3 % ± 5 %

Table 5.11: *The asymmetry measurements obtained from method 1 using the 1991 data. The errors are statistical and systematic respectively. This table also contains the predicted asymmetries obtained from a fit to MC truth level angular distributions and the statistical errors from the fit.*

where N is the number of events and k is the acceptance correction given in equation 5.5. The systematic errors are discussed in section 5.3.1. The Monte Carlo truth predictions for these asymmetries were obtained by applying the same fit to the muon angular distributions as used in method 2. For the combined data sets the distributions at each centre of mass energy were normalized to the real data luminosities before the histograms were added together and the fit applied. The statistical errors for these predictions were obtained from the fits. The asymmetries obtained by applying the fits to the efficiency corrected reconstructed Monte Carlo data are not shown, but were

found to be in good agreement with the truth level predictions.

It can be seen from tables 5.10 and 5.11 that the asymmetry measurements for the combined data sets above and below the peak are in agreement with the predictions although the associated errors are large and of the same order as the asymmetries themselves. However, the magnitude of the peak asymmetries in the 1990 and 1991 are much larger than the prediction and do not agree within the errors. The deviations from the expected value are 2.2 sigma and 2.5 sigma for the 1990 and 1991 peak asymmetries respectively.

In order to make a second set of measurements of the peak asymmetry, and to check the results given in tables 5.10 and 5.11, method 2 was used. Figure 5.3 shows the distribution of the muon polar angles, again measured for the angles between the incoming e^- and the outgoing μ^-, for the 1991 data and reconstructed Monte Carlo data at the peak.

The real data distribution was corrected on a bin by bin basis for background and for efficiency as in method 1, and the reconstructed Monte Carlo distribution was corrected for efficiency. As in method 1, the background subtraction made very little difference to the real data distribution. Immediately, it can be seen that there is a very large and unexpected asymmetry in the real data distribution which is not seen in the Monte Carlo. By applying the χ^2-fit over a range in which the selection efficiency was reasonably flat, i.e. $|cos\theta_{e^-\mu^-}| \leq 0.744$, the forward-backward charge asymmetry was obtained, and this is expressed in units of percent in table 5.12 along with its associated errors, the Monte Carlo prediction and the $\frac{\chi^2}{DoF}$ of the fit to the real data. Table 5.12 also contains the result of the fit to the 1990 peak data. The errors quoted in table 5.12 are the statistical errors obtained from the fit and the systematic errors which are discussed in section 5.3.1. The Monte Carlo prediction was obtained by applying the same fit to the truth level data distribution and the error quoted was the statistical error from this fit. As in method 1, the asymmetry obtained from the fit to

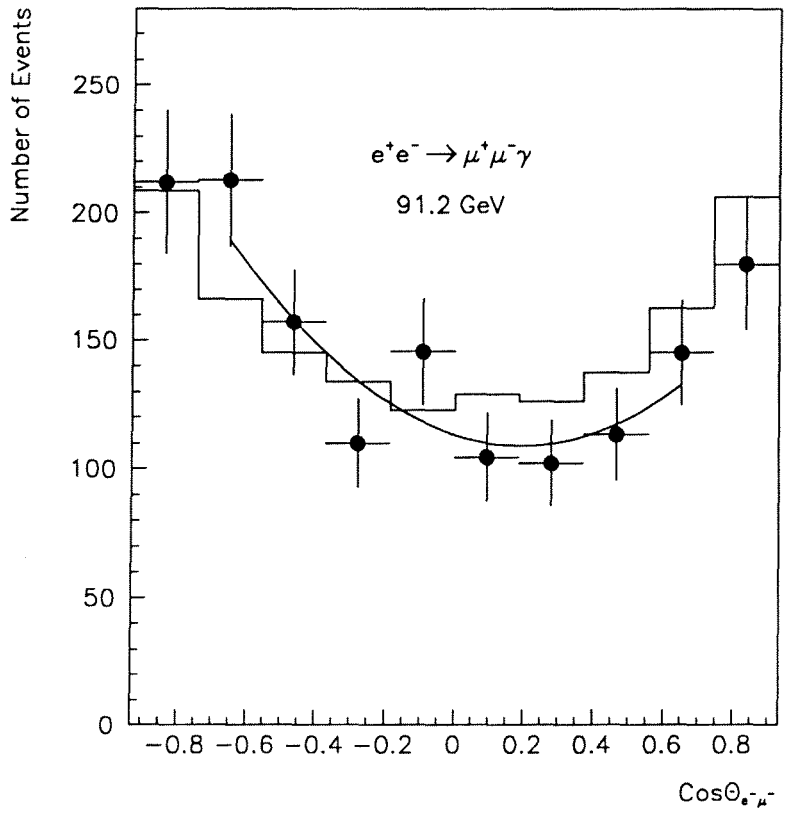

Figure 5.3: *The muon polar angle distribution. The histogram is the reconstructed and efficiency corrected MC prediction, and the dots with error bars (statistical) are the background subtracted and efficiency corrected real data. Superimposed onto this plot is a χ^2-fit to the corrected real data distribution.*

the efficiency corrected reconstructed Monte Carlo data, was found to be in agreement with the truth level predictions.

The results from method 2 agree with the results of method 1 since the measured asymmetries are found to deviate from the expected value by 2.2 sigma for 1990 and 1.9 sigma for 1991.

Year	$\sqrt{s}$/GeV	$A_{fb}{}^{exp}$	$A_{fb}{}^{pred}$	$\frac{\chi^2}{DoF}$
1990	91.214	-22 % ± 8 % ± 5 %	-1 % ± 3 %	$\frac{7.05}{6}$
1991	91.215	-15 % ± 6 % ± 4 %	-1 % ± 2 %	$\frac{5.19}{6}$

Table 5.12: *The asymmetry measurements obtained from method 2 (a χ^2-fit to the corrected real data at the peak). The quoted errors are statistical and systematic respectively. This table also contains the predicted asymmetry obtained from a fit to Monte Carlo truth level angular distributions, and its associated error is the statistical error from the fit.*

5.3.1 Asymmetry Systematic Errors

There were several sources of systematic error in the measurement of these asymmetries, and these fall under common headings for both methods.

- Background subtraction.
- Charge misassignment.
- Efficiency corrections.
- The angular range used for the measurements.
- Possible systematic differences between μ^- and μ^+ distributions.

Also, in the case of the fit, different fitting techniques can give rise to different asymmetry measurements. The contribution from the background subtraction procedure was estimated from Monte Carlo and found to be negligible in comparison to the other contributions. This was also the case for the error due to charge misassignment. This was estimated from real and Monte Carlo data by using the technique given in reference [73]. This is based on counting the number of selected events containing like signed charged tracks when the cut on the total charge has been removed. The systematic errors from the efficiency corrections, δA_{eff}, were obtained by using the

difference in the corrected and uncorrected asymmetries. These errors are generous overestimates, but are generally the smallest contribution to the systematic errors. The effect of the angular range, δA_{range}, was checked by varying the $cos\theta$ acceptance cut in the case of method 1, and by varying the range of the fit in the case of method 2. Also, the difference in the measured asymmetries obtained by using either $\theta_{e^-\mu^-}$, or $\theta_{e^+\mu^+}$ was used, δA_θ. Finally, in the case of the fit, both χ^2 and log likelihood methods were used and the difference observed here, δA_{fit}, was taken as a measure of the error. The contributions from each of these sources of error are tabulated in tables 5.13, 5.14 and 5.15 for each centre of mass energy. For the peak results, the total systematic

$\sqrt{s}$/GeV	N_{events}	$\frac{N_{events}}{N_{total}}$	$\delta A_{eff}/\%$	$\delta A_{range}/\%$	$\delta A_\theta/\%$
88.222	2	$\frac{2}{23}$	12	43	0
89.215	5	$\frac{5}{23}$	6	0	37
90.217	16	$\frac{16}{23}$	2	2	2
91.214	212	$\frac{212}{212}$	2	2	1
92.206	28	$\frac{28}{65}$	5	18	7
93.208	26	$\frac{26}{65}$	7	27	8
94.201	11	$\frac{11}{65}$	1	17	2

Table 5.13: *The contributions to the asymmetry systematic errors from method 1 for the 1990 data.*

errors shown in tables 5.10, 5.11 and 5.12 were obtained by adding in quadrature all contributions given in tables 5.13, 5.14 and 5.15 respectively. For the combined data sets, the systematic errors shown in tables 5.10 and 5.11 were determined by adding in quadrature the individual contributions at each centre of mass energy shown in tables 5.13 and 5.14, and then weighting the resulting numbers by the fraction of the events at that energy, before finally adding in quadrature all of the contributions in the

$\sqrt{s}$/GeV	N_{events}	$\frac{N_{events}}{N_{total}}$	δA_{eff}/%	δA_{range}/%	δA_{θ}/%
88.464	3	$\frac{3}{48}$	22	0	59
89.456	25	$\frac{25}{48}$	8	1	15
90.212	20	$\frac{20}{48}$	7	4	9
91.215	484	$\frac{484}{484}$	1	0	1
91.952	34	$\frac{34}{86}$	8	5	10
92.952	24	$\frac{24}{86}$	4	1	2
93.701	28	$\frac{28}{86}$	3	8	11

Table 5.14: *The contributions to the asymmetry systematic errors from method 1 for the 1991 data.*

Year	$\sqrt{s}$/GeV	N_{events}	δA_{eff}/%	δA_{range}/%	δA_{θ}/%	δA_{fit} /%
1990	91.2	212	1	4	1	3
1991	91.2	484	1	3	2	1

Table 5.15: *The contributions to the asymmetry systematic errors from method 2.*

data set.

Since the magnitudes of the measured peak asymmetries were found to be about 2 sigma larger than the predicted value, several tests were performed on the 1990 data in order to try to understand this occurrence. First of all, the data taking period was split into two parts, each containing a similar number of events. This was done in order to look for any period in which the detector was not operating efficiently. Also, the requirement that the high voltages be set on all subdetector components in an event was discarded. By studying the momentum, energy and angular distributions as a whole, and also for the forward and backward regions of the detector, no indication was found of any problems with the detector, and there was no observable change in

the shape of the muon angular distribution.

As another test of the generated radiative muon Monte Carlo sample used in this analysis, the predicted asymmetry was compared with that obtained from the standard ALEPH Monte Carlo. Again good agreement was found between the two predicted values. Also, the analysis code was checked once more by performing a χ^2-fit to the full muon angular distribution, which was obtained by the applying cuts given in section 5.2. From this fit the total muon asymmetry was determined to be $A_{\mu^+\mu^-} = -1\% \pm 2\% \pm 2\%$, which is in agreement with the published results of ALEPH. This was further proof that the analysis program was working correctly.

Another point which was considered was the effect of the initial-final state interference which is dependent upon the kinematic cuts applied to select the radiative muon pair events. Since this interference is not included within KORALZ, its effect was calculated by Z. Was [74]. By applying the same set of kinematic cuts as used in this analysis the size of the asymmetry due to the interference was found to be -3%. Adding this to the asymmetry obtained from KORALZ the total asymmetry was found to be -4%. Thus, the absence of the interference from KORALZ was not the main cause of the discrepency between the experimental and theoretical values.

In conclusion the results of the tests applied to the 1990 data indicate that the observed asymmetry is a real effect. Its significance, however, is not so high as to rule out a simple statistical fluctuation as the explanation. This is also the case for the 1991 asymmetry measurement.

5.4 Kinematic Distributions

Presented in this section are a set of kinematical distributions for the processes $e^+e^- \to \mu^+\mu^-\gamma$ and $e^+e^- \to \mu^+\mu^-\gamma\gamma$. All distributions shown here are for the data collected in 1991, unless otherwise stated, and these contain data from all centre of

mass energies. Also, the real data distributions are background subtracted, and all of the reconstructed Monte Carlo data distributions were normalized to the luminosity of the real data, before the histograms were added together. In the following figures, the points with error bars correspond to the observed events, and the histograms are the reconstructed Monte Carlo predictions. The errors shown are the statistical errors obtained from the number of entries in each bin. The Monte Carlo errors are not shown in these histograms since they are small in comparison to the other errors.

First of all a set of angular distributions are presented. Figures 5.4a and 5.4b show the photon polar angle and muon azimuthal angle distributions respectively. Figures 5.5a and 5.5b show the muon acollinearity angle and the muon-photon minimum angle distributions respectively. As well as these angular distributions, a set of energy and momentum distributions are presented here. Figures 5.6a and 5.6b show the photon energy spectrum, and the μ^- momentum distribution, as measured in the ECAL and TPC subdetectors respectively. Both of these distributions are normalized to the beam energy. The momentum distribution for the μ^+ is not shown here, but is very similar to that of the μ^- given in figure 5.6b. In chapter 4, it was explained that it is possible to calculate the momentum of particles in a three body decay entirely from the measured angular separations between the particle trajectories and the total centre of mass energy. The calculated photon energy spectrum and the calculated μ^- momentum distribution are shown in figures 5.7a and 5.7b. These are normalized to the beam energy for comparison with those plots given in figures 5.6a and 5.6b. Again the calculated momentum distribution for the μ^+ is very similar to that of the μ^-.

In order to quantify the level of agreement between the experimental and Monte Carlo distributions, the Kolmogorov test was used [75]. This test compares the shapes of two histograms, without taking into account their relative normalizations, and gives the probability that they came from the same parent distribution. The probabilities (KP), which were obtained from this method, are shown on each of the kinematic distributions.

In all cases good agreement was found between the observed and predicted distributions.

Next a set of invariant mass plots are presented. Figures 5.8a and 5.8b show the muon pair invariant mass and also the muon-photon invariant mass distributions. The latter of these distributions contains two entries per event. Both of these distributions were obtained by calculating the invariant masses using the calculated energy and momenta of the particles within the event. In both cases the real data distributions are in good agreement with the predictions from the Monte Carlo.

As explained in section 1.6 events from single $\mu^\star$ production would appear as a narrow peak in the $\mu\gamma$ invariant mass distribution. This is not seen at any particular invariant mass in the range covered here. Also, the energy of the photon radiated from a $\mu^\star$ decay could give rise to deviations in the observed energy spectrum. But since the measured photon energy spectrum is in good agreement with the electroweak predictions, there is no evidence for the single $\mu^\star$ production.

For the process $e^+e^- \rightarrow \mu^+\mu^-\gamma\gamma$ a scatter plot of $\mu\gamma$ invariant masses, containing two entries per event, is presented. This is given in figure 5.9 and contains both 1990 and 1991 data. On the y-axis are the $\mu^+\gamma$ masses and on the x-axis are the $\mu^-\gamma$ masses. Altogether, only 6 events were selected from the 1990 data and 12 events from the 1991 data sample. Here the invariant masses were calculated using the measured values of energy and momentum.

As explained earlier in section 1.6 if the $\mu^\star$'s were pair produced, the corresponding events would form a cluster around a point on the 45° line, within the mass resolutions indicated by the dashed lines. There is no indication of such clustering here, and the distribution of points is consistent with the Monte Carlo prediction, within the admittedly low statistics. This observation is consistent with the results of a similar study performed by ALEPH in which a lower limit was imposed on the mass of the $\mu^\star$ of $M_{\mu^\star} \geq 46.1$ GeV at 95% confidence level [42]. The mass resolutions which were indicated in figure 5.9 were determined in the following way. For different mass ranges,

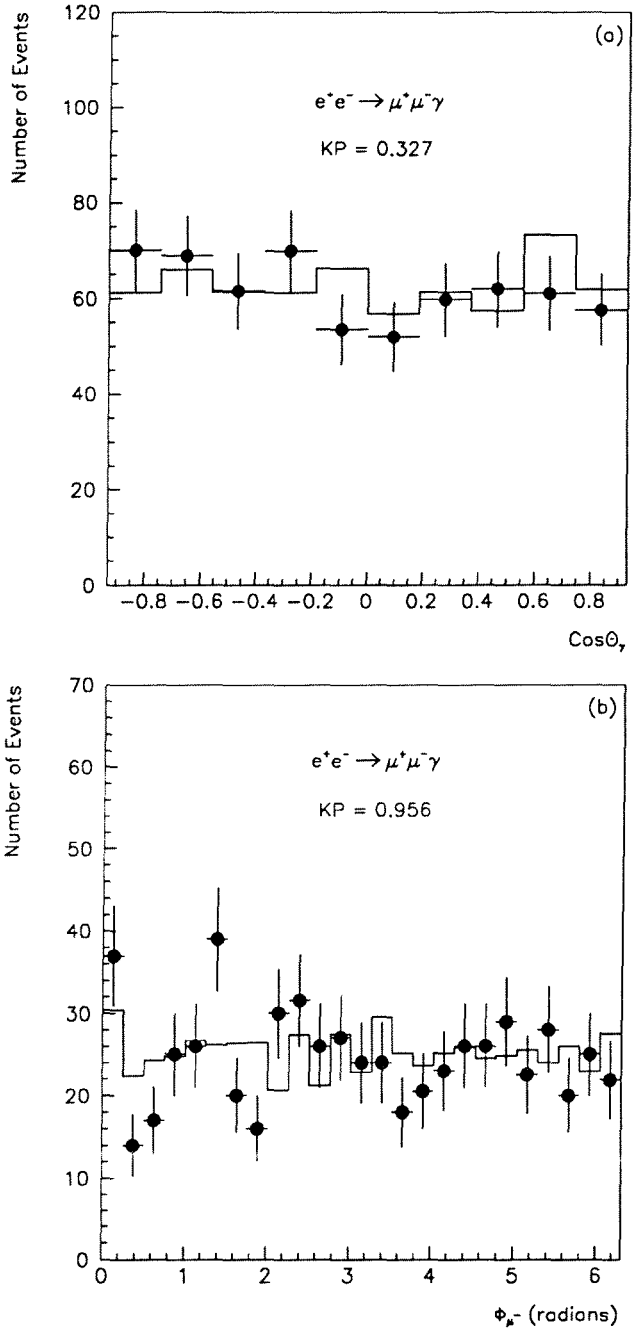

Figure 5.4: *a). The photon polar angle distribution. b). The muon azimuthal angle distribution. The dots with error bars (statistical) represent the 1991 data and the histograms represent the reconstructed MC predictions. Also shown in these figures are the Kolmogorov probabilities (KP).*

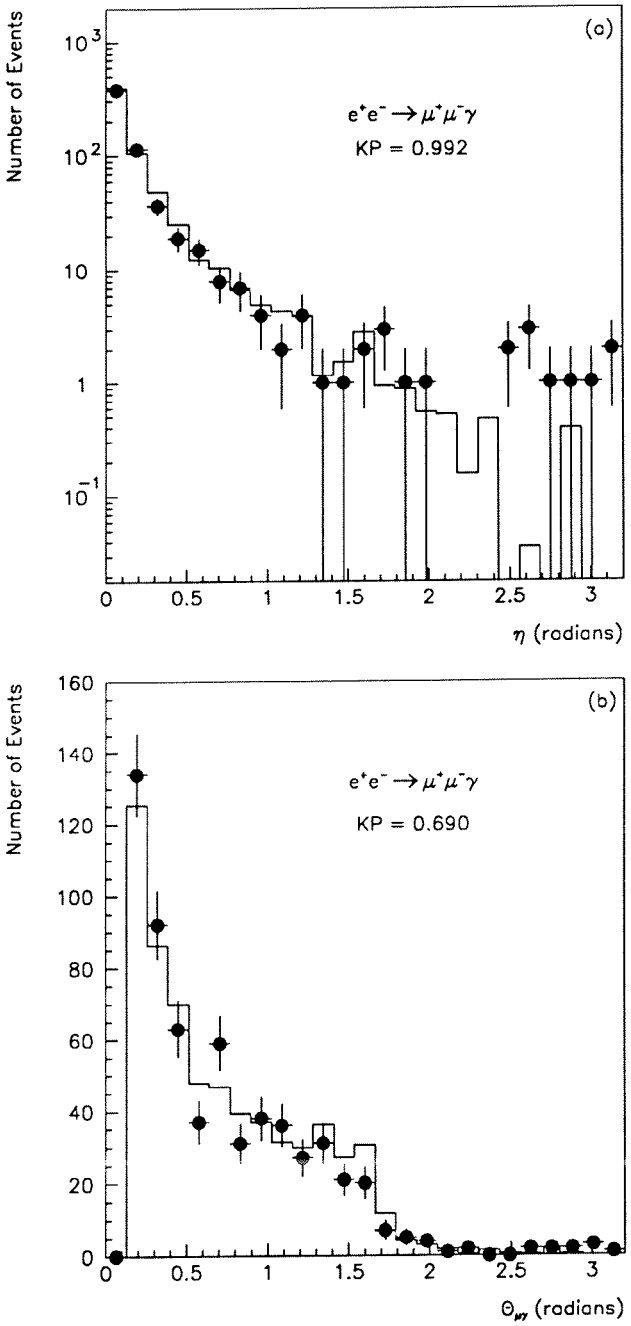

Figure 5.5: *a). The muon pair acollinearity angle distribution. b). The muon-photon minimum angle distribution. The dots with error bars (statistical) represent the 1991 data and the histograms are the reconstructed MC predictions. Also shown in these figures are the Kolmogorov probabilities (KP).*

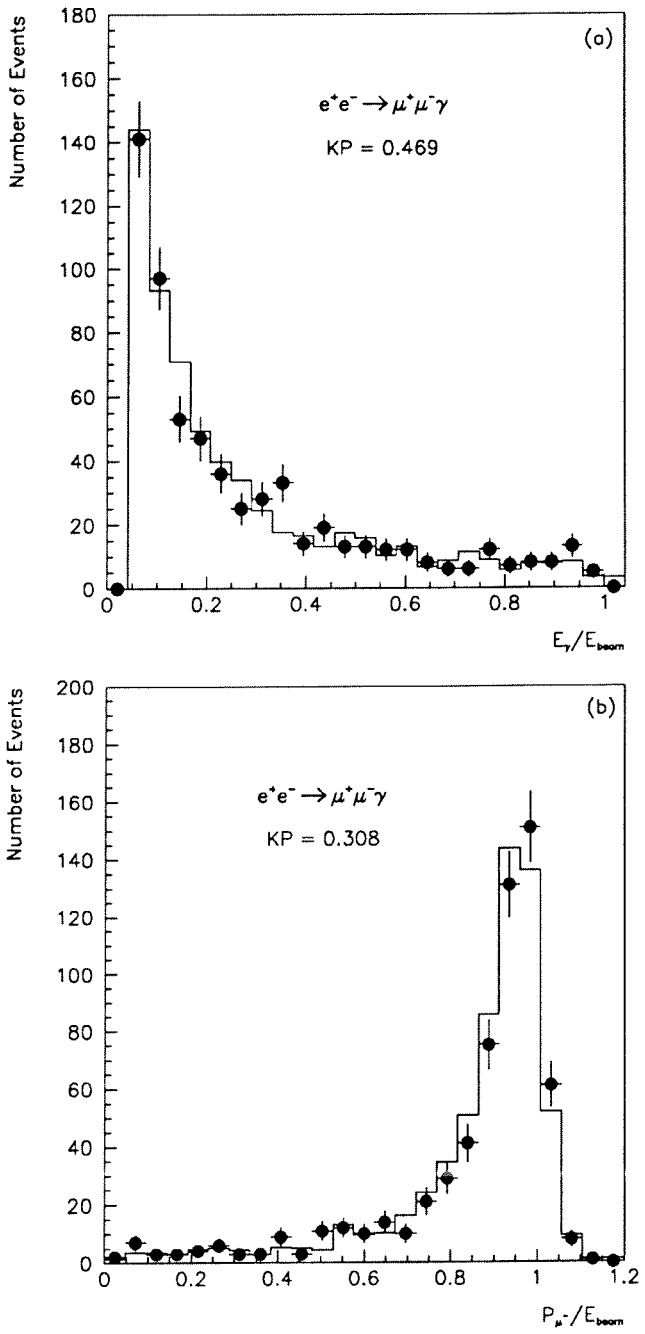

Figure 5.6: *a). The measured photon energy spectrum. b). The measured μ^- momentum distribution. The dots with error bars (statistical) represent the 1991 data and the histograms are the reconstructed MC predictions. Also shown in these figures are the Kolmogorov probabilities (KP).*

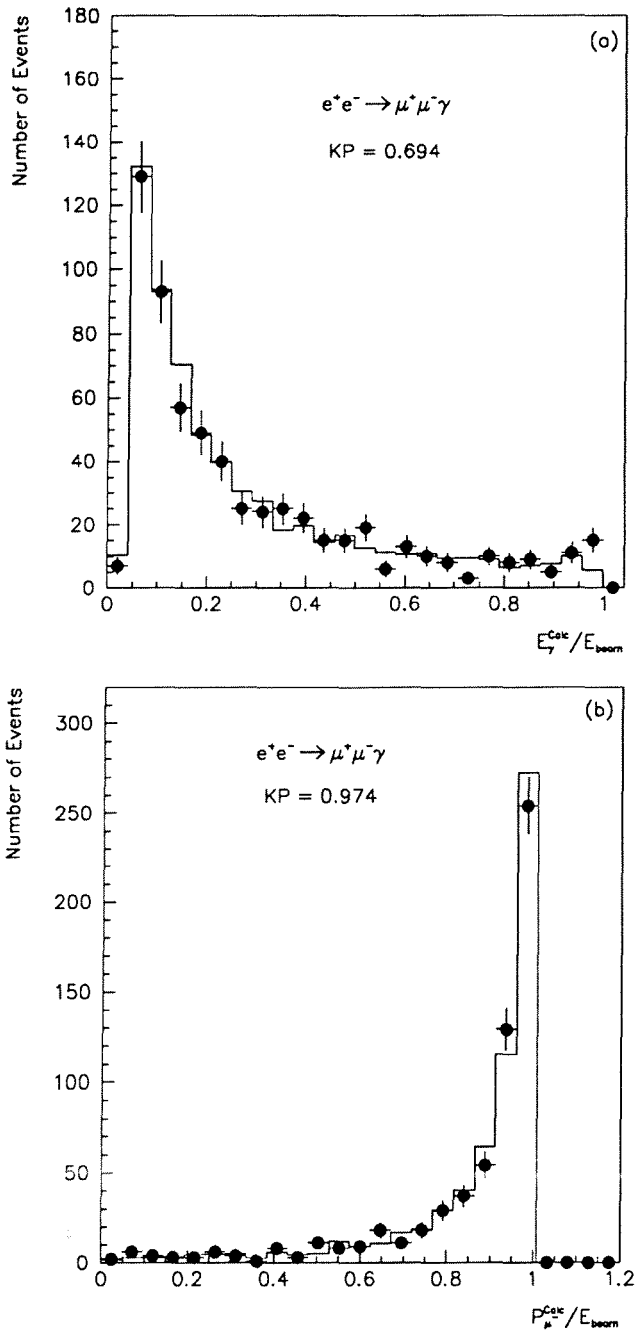

Figure 5.7: *a). The calculated photon energy spectrum. b). The calculated μ^- momentum distribution. The dots with error bars (statistical) represent the 1991 data and the histograms are the reconstructed MC predictions. Also shown in these figures are the Kolmogorov probabilities (KP).*

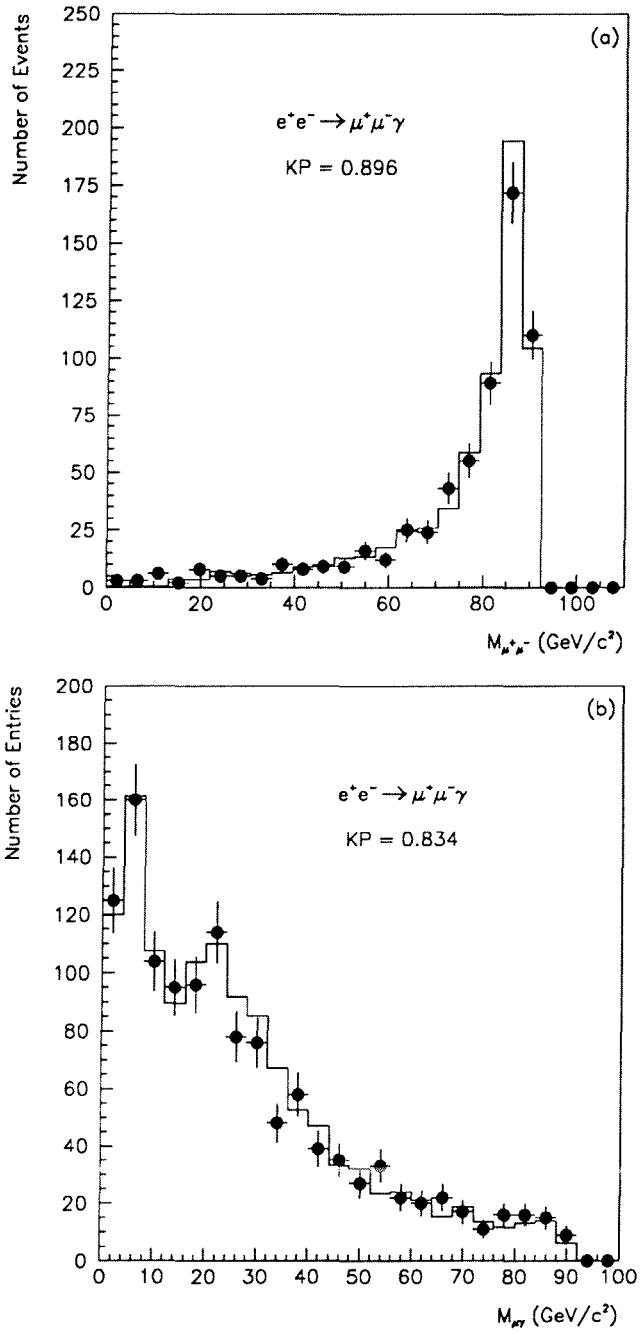

Figure 5.8: *a). The $\mu^+\mu^-$ invariant mass distribution. b). The $\mu\gamma$ invariant mass distribution (two entries per event). The dots with error bars (statistical) represent the 1991 data and the histograms are the reconstructed MC predictions. Also shown in these figures are the Kolmogorov probabilities (KP).*

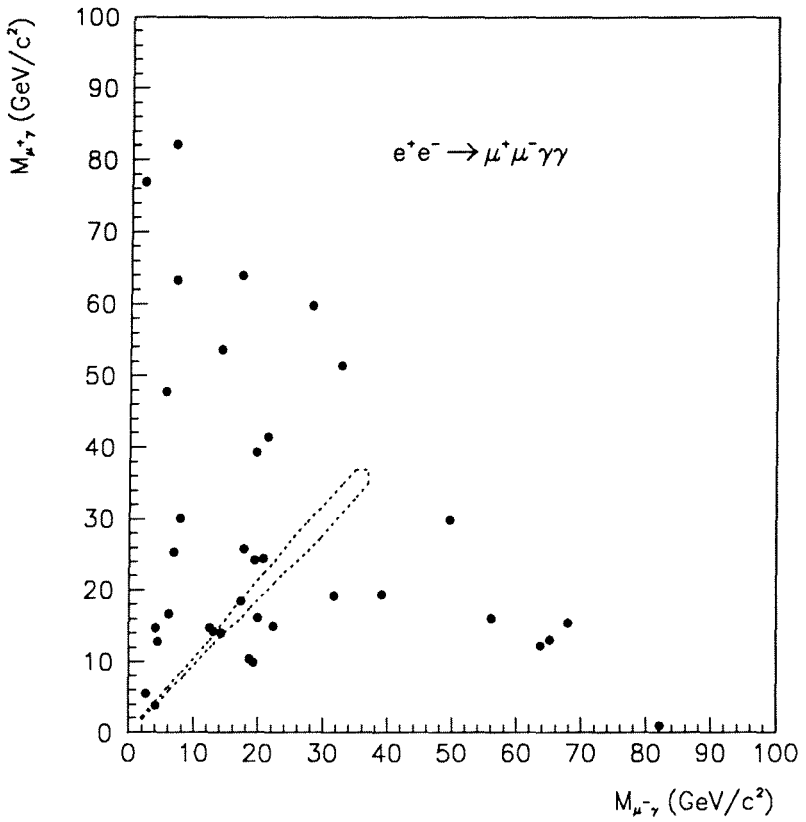

Figure 5.9: *A scatter plot of the invariant masses of $\mu^+\gamma$ and $\mu^-\gamma$ combinations for the $\mu\mu\gamma\gamma$ final state. This plot contains data from 1990 and 1991 and there are two entries per event. The dashed lines indicate a range of two sigma of the $\mu\gamma$ mass resolution about a* 45° *line.*

the ratio of reconstructed Monte Carlo invariant mass to generator truth level invariant mass was plotted. For each of these distributions the rms value was then measured. The invariant mass resolutions were then estimated by multiplying the mean mass in a given range by twice the rms value.

Chapter 6

Conclusions

A method was developed to perform a study of radiative muon pair production at the Z^0 resonance, by using the ECAL and TPC subdetectors of ALEPH. From this work several measurements were performed. The first of these was the measurement of the total cross-sections for the processes $e^+e^- \rightarrow \mu^+\mu^-\gamma$, and $e^+e^- \rightarrow \mu^+\mu^- N\gamma$, for a minimum photon energy of 2 GeV. These measurements were made at seven centre of mass energies in the region of the Z^0 resonance. It was found that the cross-sections measured for the 1990 data set were generally lower than the predictions. This was thought to be due to a statistical fluctuation. With the inclusion of the 1991 results the cross-section measurements were found to be in acceptable agreement with KORALZ.

The second measurement was of the forward-backward charge asymmetry. This was done for the combined data below the peak, at the peak, and above it. For the measurements either side of the peak, agreement was found between the real data and the Monte Carlo, although the statistical and systematic errors were very large. The asymmetry at the Z^0 peak was measured for both the 1990 and 1991 data. The magnitudes of the measured values were found to be larger than the KORALZ prediction by 2.2 sigma and 2.5 sigma respectively. These observations were confirmed by using a second method which involved applying a fit to the observed muon polar

angle distributions. In this case the observed asymmetries for 1990 and 1991 were larger than the prediction by 2.2 sigma and 1.9 sigma respectively. Although the measured peak asymmetries disagree with prediction from KORALZ the significance of these deviations is not so high as to rule out simple statistical fluctuations as the explanation. In this context it should be noted that the results from studies of other channels have shown no deviation from the standard model.

As well these measurements, a set of kinematic distributions for the process $e^+e^- \rightarrow \mu^+\mu^-\gamma$ were obtained, and these were all found to agree well with the electroweak predictions.

A search was conducted for $\mu^\star$ creation, in both the single and pair production channels. This was done by looking for structure within the invariant mass plots. In the single $\mu^\star$ search, good agreement was found between the real data and the Monte Carlo, and there was no indication of structure within the mass range covered in this work. In the pair production search, the predicted clustering around a point on the line of equal mass was not observed, and the distribution of points was found to be consistent with QED predictions of KORALZ, within the statistics. This result is consistent with the results of a study performed by ALEPH in which a lower limit was set on the mass of the $\mu^\star$ of $M_{\mu^\star} \geq 46.1$ GeV at 95% confidence level.

References

[1] A. Einstein, *The Meaning of Relativity*, Science Publications, Chapman and Hall, (1987) 6th Edition.

[2] M. Breidenbach et al., *Observed Behaviour of Highly Inelastic Electron-Proton Scattering*, Phys. Rev. Lett. **23** (1969) 935.
R.P. Feynman, *Very High-Energy Collisions of Hadrons*, Phys. Rev. Lett. **23** (1969) 1415.

[3] D.C. Cundy, *Proc. XVII Int. Conf. on High Energy Physics, London*, July (1974) (Didcot, Berks: Science Research Council) pp IV-131–148.

[4] G. Arnison et al., *Experimental Observation of Isolated Large Transverse Energy Electrons with Associated Missing Energy at* $\sqrt{s}$ = 540GeV, Phys. Lett. **B122** (1983) 103.

[5] M. Banner et al., *Observation of Single Isolated Electrons of High Transverse Momentum in Events with Missing Transverse Energy at the CERN* $\bar{p}p$ *Collider*, Phys. Lett. **B122** (1983) 476.

[6] P. Bagnaia et al., *Evidence for* $Z^0 \rightarrow e^+e^-$ *at the CERN* $\bar{p}p$ *Collider*, Phys. Lett. **B129** (1983) 130.

[7] P. Langacker, *Grand Unified Theories and Proton Decay*, Phys. Rep. **72** (1981) 185.

[8] F. Combley, *(g-2) factors for the muon and electron and consequences for QED*, Rep. Prog. Phys. **42** (1979) 1889.

[9] I.J.R Aitchison, Contemp. Phys. **26** (1985) 333.

[10] J.C. Maxwell, Phil. Trans. R. Soc. **155** (1864) 459.

[11] P.A.M. Dirac, Proc. R. Soc. **A133** (1931) 60.

[12] D.H. Perkins, *Introduction to High Energy Physics*, Addison-Wesley (1987), 3rd Edition.

[13] F. Halzen and A.D. Martin, *Quarks and Leptons: An Introductory Course in Modern Particle Physics*, Wiley (1984).

[14] I.J.R. Aitchison and A.J.G. Hey, *Gauge Theories in Particle Physics*, Adam Hilger (1982).

[15] C.N. Yang. and R.L. Mills, Phys. Rev. **96** (1954) 191.

[16] J. Chadwick, *Possible Existence of a Neutron*, Nature, **129** (1932) 312.

[17] E. Fermi, Nuovo Cimento **11** (1934) 1.
E. Fermi, Z. Phys. **88** (1934) 161.

[18] R.P. Feynman and M. Gell-Mann, Phys. Rev. **110** (1958) 1178.

[19] M. Goldhaber, L. Grodzins, and A.W. Sunyar, *Helicity of Neutrinos*, Phys. Rev. **109** (1958) 1015.

[20] H. Yukawa, Proc. Phys. Math. Soc. Japan. **17** (1935) 48.

[21] S. L. Glashow, *Partial Symmetries of Weak Interactions*, Nucl. Phys. **22** (1961) 579.

[22] P. W. Higgs, *Broken Symmetries and the Masses of Gauge Bosons*, Phys. Rev. Lett. **13** (1964) 508.

[23] E. Gross and P. Yepes, *Standard Model Higgs Boson Hunting at LEP*, International Journal of Modern Physics A, September 1992.

[24] S. Weinberg, *A Model of Leptons*, Phys. Rev. Lett. **19** (1967) 1264.

[25] A. Salam, *Elementary Particle Theory*, Proc. 8th Nobel Symposium, ed. N. Svartholm, Almquist and Wiksell, Stockholm (1968) 367.

[26] G. t'Hooft, *Renormalization of Massless Yang - Mills Fields*, Nucl. Phys. **B33** (1971) 173.

[27] J. Goldstone, A. Salam and S. Weinberg, Phys. Rev. **127** (1962) 965.
J.Goldstone, Nuovo Cimento **19** (1961) 154.

[28] VENUS Collaboration, Y. Yonezawa et al., Phys. Lett. **B264** (1991) 212.

[29] MAC Collaboration, W.T. Ford et al., Phys. Rev. Lett. **51** (1983) 257.

[30] CELLO Collaboration, H.J. Behrend et al., Phys. Lett. **B158** (1985) 537.

[31] JADE Collaboration, W. Bartel et al., Z. Phys. **C24** (1984) 223.

[32] Mark J Collaboration, B. Adeva et al., Phys. Rev. **D38** (1988) 2665.

[33] V.A. Koralchuk and I.V. Stoletnii, *The Differential and Total Cross-section of the $e^+e^- \to \mu^+\mu^-\gamma$ Process in Terms of the Theory of Electroweak Interactions*, Ukr. Fiz. Zh. USSR. Vol. **32** part 5 (1987) 645-650.

[34] G. Alterelli et al., *Z Physics at LEP 1 - Standard Physics*, CERN report **89-08** (1989) Vol.I.

[35] G. Alterelli et al., *Z Physics at LEP 1 - Event Generators and Software*, CERN report **89-08** (1989) Vol.III.

[36] MAC Collaboration, E. Fernandez et al., Phys. Rev. Lett. **54** (1985) 1620.

[37] Mark J Collaboration, B. Adeva et al., Phys. Rev. Lett. **55** (1985) 665.

[38] S. Jadach, B.F.L. Ward, Z. Was, *Complete Standard Model predictions for the muon forward-backward asymmetry at LEP*, Phys. Lett. **B257** (1991) 213.

[39] J.H. Kühn, S. Jadach, R.G. Stuart, Z. Was, Z. Phys. **C38** (1988) 609.
J.H. Kühn, R.G. Stuart, Phys. Lett. **B200** (1988) 360.
S. Jadach, Z. Was, Phys. Lett. **219** (1989) 103.

[40] The LEP Collaborations: ALEPH, DELPHI, L3 and OPAL, *Electroweak Parameters of the Z^0 Resonance and the Standard Model*, Phys. Lett. **B270** (1991) 97.

[41] G. Alterelli et al., *Z Physics at LEP 1 - Higgs Search and New Physics*, CERN report **89-08** (1989) Vol.II.

[42] The ALEPH Collaboration, D. Decamp et al., *Searches for New Particles in Z^0 Decays Using the ALEPH Detector*, Phys. Rep. **216** (1992) 253.

[43] LEP, *Large Electron-Positron Storage Ring. Technical Notebook*, CERN Publications (1989).

[44] ALEPH Collaboration, W. Blum (Editor), *The ALEPH Handbook 1989*, ALEPH Internal Note **89-77** (1989).

[45] ALEPH Collaboration, D. Decamp et al., *ALEPH: A Detector for Electron-Positron Annihilations at LEP*, Nucl. Instrum. Methods. **A294** (1990) 121.

[46] M. Bardadin-Otwinowska et al., *Electromagnetic calorimeter response to muons and non-interacting pions*, ALEPH Internal Note **89-2** (1989).

[47] G. Bagliesi et al., *The Combined Response of the ALEPH Electromagnetic and Hadronic Calorimeters to Pions*, Nucl. Instr. and Meth. **A286** (1990) 61.

[48] D.E. Plane, *The West Area Beam*, CERN-SPS **83-22**.

[49] J. Strong, *The ALEPH Second Level Trigger Processor*, ALEPH Internal Note **87-127** (1987).

[50] B. Jost, *Real-Time Data Reduction using a μVAX Processor Farm*, IEEE. Trans. Nucl. Sci. **36-5** 1452.

[51] I. Videau, *The Data Acquisition System for ALEPH*, IEEE. Trans. Nucl. Sci. **32-4** (1985) 1484.

[52] The Institute of Electrical and Electronics Engineers (IEEE), *IEEE Standard FASTBUS Modular High-Speed Data Acquisition and Control System*, ANSI/IEEE Std. 960-1986.

[53] J. Knobloch and P. Norton, *Status of Reconstruction Algorithms for ALEPH*, ALEPH Internal Note (1991).

[54] O. C. Allkofer et al., Phys Lett **B36** (1971) 425.

[55] S. Hayakawa, *Cosmic Ray Physics*, New York: Wiley, (1969).

[56] J. Ziegler, *The background in detectors caused by sea level cosmic rays*, Nucl. Instrum. Meth. **191** (1981) 419-24.

[57] S. Jadach, Z. Was, Comp. Phys. Commun. **36** (1985) 191.
S. Jadach, B.F.L. Ward, Z. Was, *The Monte Carlo program KORALZ, version 3.8, for the lepton or quark pair production at LEP/SLC energies.*, Comp. Phys. Commun. **66** (1991) 276.

[58] F.A. Berends and R. Kleiss, Nucl.Phys. **B228** (1983) 737.
M. Böhm, A. Denner and W. Hollik, Nucl.Phys. **B304** (1988) 687.
F.A. Berends, R. Kleiss, and W. Hollik, Nucl.Phys. **B304** (1988) 712.

[59] J.E. Campagne and R. Zitoun, *Electromagnetic Radiative Corrections at LEP-SLC Energies for Experimentalists*, Z. Phys. **C43** (1989) 469.

[60] T. Sjöstrand, Comp. Phys. Commun. **39** (1986) 347.

[61] J.A.M. Vermaseren, *Proceedings of the International Workshop on Gamma Gamma Collisions*, Amiens, April 1980, (Springer-Verlag Lecture Notes in Physics **134**).
R. Bhattacharya, J. Smith, and G. Grammer, Phys. Rev. **D15** (1977) 3267.
J.A.M. Vermaseren, program long writeup (unpublished).

[62] B. Bloch-Devaux, *KINLIB - ALEPH Event Generator Library Documentation*, ALEPH Internal Note **91-78** (1991).

[63] I.F. Ginzburg and V.G. Serbo, Phys. Lett. **B109** (1982) 231.

[64] F. Ranjard, *GALEPH - Monte Carlo Program for ALEPH*, ALEPH Internal Note **88-119** (1988).

[65] ALEPH Muon Group, J. Nash et al., *Measurement of the $e^+e^- \to \mu^+\mu^-$ cross-section in ALEPH*, ALEPH Internal Note **90-190** (1990).
ALEPH Collaboration, D. Decamp et al., *Measurement of Electroweak Parameters from Z^0 Decays into Fermion Pairs*, Z. Phys. **C48** (1990) 365.
ALEPH Collaboration, D. Decamp et al., *Improved Measurements of Electroweak Parameters from Z^0 Decays into Fermion Pairs*, Z. Phys. **C53** (1992) 1.

[66] ALEPH Collaboration, D. Buskulic et al., *Update of Electroweak Parameters from Z^0 Decays*, Submitted to Phys. Lett. B (1993).

[67] J. Badier et al., *The EBNEUT Analysis Package*, ALEPH Internal Note **90-52** (1990).

[68] C. Grab, *DALI - Event Display User's Guide*, ALEPH Internal Note **89-175** (1989).

[69] W.S. Babbage, *A Study of Final State Radiation in $Z^0 \to q\bar{q}\gamma$ Decays*, PhD. Thesis, Unpublished (1993).

[70] ALEPH Collaboration, D. Decamp et al., *Measurement of the Absolute Luminosity with the ALEPH Detector*, Z. Phys. **C53** (1992) 375.

[71] T. Fearnley et al., *Luminosity Errors - Again*, ALEPH Internal Note **93-06** (1993).

[72] R. Marshall, *The Statistics of Electroweak Induced Asymmetry Measurements*, RAL-84-003 (1984).

[73] F. Ould-Saada, PhD. Thesis, Saclay, CEA-N-2505, Unpublished (1986).

[74] Z. Was, Private communication.

[75] A.N. Kolmogorov, *Foundations of the Theory of Probability*, Chelsea Publishing Company (1950).